



---

Publicly Accessible Penn Dissertations


---

1993

## A Time-Resolved Spectroscopic Study of Photoinitiated Electron Transfer Reactions in Solution

Christopher J. Galli  
*University of Pennsylvania*

Follow this and additional works at: <https://repository.upenn.edu/edissertations>

 Part of the [Chemistry Commons](#)

---

### Recommended Citation

Galli, Christopher J., "A Time-Resolved Spectroscopic Study of Photoinitiated Electron Transfer Reactions in Solution" (1993). *Publicly Accessible Penn Dissertations*. 3682.  
<https://repository.upenn.edu/edissertations/3682>

This paper is posted at ScholarlyCommons. <https://repository.upenn.edu/edissertations/3682>  
For more information, please contact [repository@pobox.upenn.edu](mailto:repository@pobox.upenn.edu).

---

# A Time-Resolved Spectroscopic Study of Photoinitiated Electron Transfer Reactions in Solution

## Abstract

Photoinitiated electron transfer reactions may be considered within the context of two categories: (1) direct electron transfer, as observed in charge transfer molecular complexes. The photoexcitation couples the ground and charge transfer potential surfaces and (2) indirect electron transfer, as observed in covalently bonded donor (D) and acceptor (A) moieties. The optical preparation of an eigenstate of the donor or acceptor is followed by the evolution of the system to the charge transfer state. This thesis presents a study of pico- and subpicosecond polarization and vibrational relaxations accompanying these two classes of condensed phase electron transfer reactions.

The thesis presents optical ultrafast pump-probe measurements on the electron donor-acceptor complex tetracyanoethylene-hexamethylbenzene in polar and non-polar solvents. The experimental electron transfer rates are compared with nonadiabatic and adiabatic electron-transfer theories using a previously published analysis of all the vibrational modes active of the reaction. As the experimental electron transfer rates are competitive with and in some cases faster than the polarization relaxation time of the solvent, it is necessary to simulate the Smoluchowski diffusion of the reacting system over an equilibrating reaction coordinate.

Regarding the coupling of the reactant and product electronic surfaces, it is shown that the nuclear kinetic operator can give rise to the coupling responsible for the electron transfer reaction. This non-Born-Oppenheimer matrix element is estimated using information obtained from the absorption and Raman spectra. Using this coupling, good agreement is found between the experimentally observed and theoretically predicted rates.

This thesis also presents an optical time resolved spectroscopic study of the indirect electron transfer reaction in the model system magnesium triphenylporphyrinquinone in a range of solvent environments. These molecules have long served as model compounds for the ultrafast dynamics in photosynthetic complexes. In view of the recently observed coherent relaxation dynamics of Mg-tetraphenylporphyrin, these multicomponent electron transfer kinetic data are analyzed, focussing on the role of low frequency coherences in electron transfer processes.

## Degree Type

Dissertation

## Degree Name

Doctor of Philosophy (PhD)

## Graduate Group

Chemistry

## Subject Categories

Chemistry

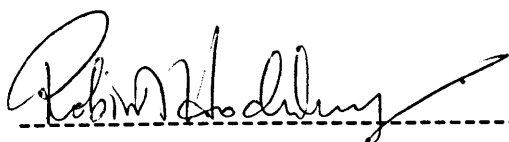
A TIME RESOLVED SPECTROSCOPIC STUDY OF PHOTOINITIATED  
ELECTRON TRANSFER REACTIONS IN SOLUTION

Christopher J. Galli

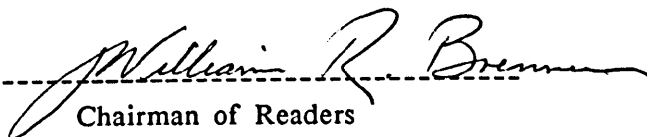
A Dissertation in Chemistry

Presented to the Faculties of the University of Pennsylvania in Partial  
Fulfillment of the Requirements for the Degree of Doctor of Philosophy

1993



Supervisor of Dissertation



Chairman of Readers



Graduate Group Chairman



Reader



Reader

CHEMISTRY / QD / 001 / 1993 / G168

**ABSTRACT**

**A TIME RESOLVED SPECTROSCOPIC STUDY OF  
PHOTOINITIATED ELECTRON TRANSFER REACTIONS IN SOLUTION**

**CHRISTOPHER J. GALLI**

**ROBIN M. HOCHSTRASSER**

Photoinitiated electron transfer reactions may be considered within the context of two categories: (1) direct electron transfer, as observed in charge transfer molecular complexes. The photoexcitation couples the ground and charge transfer potential surfaces and (2) indirect electron transfer, as observed in covalently bonded donor (D) and acceptor (A) moieties. The optical preparation of an eigenstate of the donor or acceptor is followed by the evolution of the system to the charge transfer state. This thesis presents a study of pico- and subpicosecond polarization and vibrational relaxations accompanying these two classes of condensed phase electron transfer reactions.

The thesis presents optical ultrafast pump-probe measurements on the electron donor-acceptor complex tetracyanoethylene-hexamethylbenzene in polar and non-polar solvents. The experimental electron transfer rates are compared with nonadiabatic and adiabatic electron-transfer theories using a previously published analysis of all the vibrational modes active of the reaction. As the experimental electron transfer rates are competitive with and in some cases faster than the polarization relaxation time of the

solvent, it is necessary to simulate the Smoluchowski diffusion of the reacting system over an equilibrating reaction coordinate.

Regarding the coupling of the reactant and product electronic surfaces, it is shown that the nuclear kinetic operator can give rise to the coupling responsible for the electron transfer reaction. This non-Born-Oppenheimer matrix element is estimated using information obtained from the absorption and Raman spectra. Using this coupling, good agreement is found between the experimentally observed and theoretically predicted rates.

This thesis also presents an optical time resolved spectroscopic study of the indirect electron transfer reaction in the model system magnesium triphenylporphyrinquinone in a range of solvent environments. These molecules have long served as model compounds for the ultrafast dynamics in photosynthetic complexes. In view of the recently observed coherent relaxation dynamics of Mg - tetraphenylporphyrin, these multicomponent electron transfer kinetic data are analyzed, focussing on the role of low frequency coherences in electron transfer processes.

## TABLE OF CONTENTS

CHAPTER	PAGE
I. Introduction.....	1
References.....	4
II. Electron Transfer Theory.....	14
A. Introduction.....	14
B. Nonequilibrium Polarization.....	17
C. Coupling Elements.....	24
D. Dimensionality of Reaction Coordinate.....	30
1. Exterior Modes.....	31
2. Interior Modes.....	32
E. Reaction Coordinate Parameters.....	37
F. Rate Expressions.....	39
References.....	49
III. Experimental Methods.....	62
A. Time Resolved Spectrometer.....	62

B.	Multipass Amplification.....	66
C.	Pulse Compression.....	70
D.	Continuum Generation.....	71
E.	Optical Fibers.....	74
F.	Experimental Configurations.....	77
	References.....	81

#### IV. Electron Transfer in the Molecular Complex

	Tetracyanoethylene-Hexamethylbenzene.....	96
A.	Introduction.....	96
B.	Donor-Acceptor System.....	99
C.	Charge Recombination Measurements.....	101
	1. Nonpolar Solvents.....	102
	2. Polar Solvents.....	103
D.	Theoretical Electron Transfer Rate.....	107
E.	Rate Parameters from Static Spectra.....	111
	1. Electronic Coupling.....	111
	2. Driving Force and Reorganization Energy.	112
F.	Non-Born-Oppenheimer Coupling.....	113
G.	Evaluation of Rate Expressions.....	118
H.	Discussion and Conclusion.....	122

References.....	125
V. Electron Transfer in Porphyrin - Quinones.....	174
A. Introduction.....	174
B. Coherences and Their Role in Reactions.....	175
C. Observed Coherences in Porphyrins and Porphyrin-Quinones.....	180
D. Description of System and Expectations.....	183
E. Results and Discussion.....	184
References.....	189
APPENDIX	PAGE
I. Nondissertation Research Summary.....	216
A. Coherence and Electronic Energy Transfer.....	216
B. Ultrafast Electron Transfer (ET) in Nile Blue- Dimethylaniline and related Complexes.....	218



C.	Low Frequency Coherence in Electron Transfer Reactions.....	219
D.	Intermolecular Vibrational Coherence in Liquid Pyrrole.....	220
E.	Electronic Coherence in Nearly Degenerate States of Magnesium Tetraphenylporphyrin in Solution.....	221

## LIST OF FIGURES

FIGURE	PAGE
--------	------

### Chapter I

I.1	Free energy diagram for direct photoinduced electron transfer....	6
I.2	Free energy diagram for indirect photoinduced electron transfer.	8
I.3	Molecular structure of tetracyanoethylene-hexamethylbenzene....	10
I.4	Molecular structure of porphyrinquinone.....	12

### Chapter II

II.1	Diagram illustrating reaction coordinate parameters.....	52
II.2	Classical solvent reaction coordinate.....	54
II.3	Multiple classical solvent reaction coordinates.....	56
II.4	Illustration of Marcus reaction regimes.....	58
II.5	Reaction coordinate along high frequency mode.....	60

### Chapter III

III.1	Colliding pulse mode locked laser.....	84
III.2	Real time autocorrelator.....	86
III.3	Multipass amplifier.....	88
III.4	Femtosecond spectrometer.....	90
III.5	Spectral output of optical fiber.....	92
III.6	Detection configuration for polarization spectroscopy.....	94

### Chapter IV

IV.1	Experimental absorption spectrum of TCNE-HMB.....	128
IV.2	Fit of TCNE-HMB absorption spectrum.....	130
IV.3	Morse potentials for the ground and first electronic states of TCNE-HMB.....	132
IV.4	Transient bleach of TCNE-HMB in cyclohexane.....	134
IV.5	Transient bleach of TCNE-HMB in carbon tetrachloride probed at 540 to 650 nm.....	136
IV.6	Transient bleach of TCNE-HMB in glycerol triacetate.....	138
IV.7	Transient bleach of TCNE-HMB in acetonitrile.....	140
IV.8	Transient bleach of TCNE-HMB in acetone.....	142
IV.9	Transient bleach of TCNE-HMB in ethyl acetate.....	144
IV.10	Transient bleach of TCNE-HMB in tetrahydrofuran.....	146

IV.11	Transient bleach of TCNE-HMB in nitrobenzene.....	148
IV.12	Transient bleach of TCNE-HMB in trichloroethene.....	150
IV.13	Transient bleaches of TCNE-HMB in butrynitrite.....	152
IV.14	Transient bleach of TCNE-HMB in acetonitrile probed at 580 to 650 nm.....	154
IV.15	Transient absorption of TCNE <sup>-</sup> probed at 450 nm.....	156
IV.16	Experimental electron transfer times versus solvent relaxation time.....	158
IV.17	Experimental electron transfer times with Marcus rates and simulation results versus solvent relaxation time.....	160
IV.18	Energy accepted by 165 cm <sup>-1</sup> donor - acceptor stretch.....	162
IV.19	Energy accepted by 1551 cm <sup>-1</sup> complex mode.....	164
IV.20	Energy accepted by modes coupled to electron transfer in TCNE-HMB.....	166

## Chapter V

V.1	Level diagram for magnesium tetraphenylporphyrin.....	192
V.2	Transient gain anisotropy of magnesium tetraphenylporphyrin in tetrahydrofuran.....	194

V.3	Transient absorption of freebase porphyrin-quinone in glycerol triacetate at 500 and 510 nm.....	196
V.4	Transient absorption of freebase porphyrin-quinone in glycerol triacetate at 520 nm.....	198
V.5	Transient absorption of magnesium triphenylporphyrin-quinone in pyridine at 650 nm over 2 ps .....	200
V.6	Transient absorption of magnesium triphenylporphyrin-quinone in pyridine at 650 nm over 4 ps .....	202
V.7	Transient absorption of magnesium triphenylporphyrin-quinone in pyridine at 620 nm over 30 ps .....	204
V.8	Transient absorption of magnesium triphenylporphyrin-quinone in tetrahydrofuran at 650 nm over 2 ps .....	206
V.9	Transient absorption of magnesium triphenylporphyrin-quinone in tetrahydrofuran at 650 nm over 2ps .....	208
V.10	Transient absorption of magnesium triphenylporphyrin-quinone in tetrahydrofuran at 620 nm over 30 ps .....	210
V.11	Transient absorption of magnesium triphenylporphyrin-quinone in toluene at 620 nm over 30 ps .....	212
V.12	Transient absorption of magnesium triphenylporphyrin-quinone in toluene at 620 nm over 2 ps .....	214

## Chapter I

### Introduction

Photosynthetic electron transfer reactions transduce electromagnetic radiation from the sun to the chemical energy required to perform cellular work. The transduction achieved by the photosynthetic molecular complex is the production of a charge separated electronic state of the system following the absorption of an optical photon. While much progress has been made toward understanding these critical reactions since the pioneering work of R. Marcus in the mid-1950's, the ultimate goal of emulating the efficiency and specificity of biological electron transfer will not be attained without a detailed understanding of the molecular properties of the photoactive system and the expression of these properties in theoretical treatments of the reaction dynamics.

Recent technological developments in subpicosecond spectroscopy permit the examination of these and other photoinduced reactions on a time scale faster than vibrational relaxation in polyatomic systems [1], faster than the dielectric solvent reorganization [2-6], and faster than the electronic dephasing of degenerate levels [7]. Such time resolution enables the investigation of the dynamics of nonequilibrated reacting systems and allows the observation of nuclear [8,9] and electronic [10,11]

coherences accompanying an electron transfer event.

Due to the ubiquity of electron transfer processes strong interplay has developed amongst physics, biology, and the diverse branches of chemistry in an effort to understand the mechanism of electron transfer reactions. As much of the motivation for the study of electron transfer processes stems from our interest in natural photosynthesis this photochemical system serves as a focal point for workers from these fields. Much of the effort from synthetic chemists in electron transfer studies has been directed toward developing model systems to examine the kinetics and energetics of the photosynthetic processes.

The variability of oxidation states in transition metal complexes has been exploited by the inorganic chemist in the development of model compounds including, for example, modified protein systems. One such technique allows the measurement of long range electron transfer kinetics through a protein matrix such as cytochrome *c* from Ru (NH<sub>3</sub>)<sub>4</sub><sup>+</sup> donor sites [12]. Asymmetric binuclear compounds such as binuclear Ru (II) coordination complexes have been used to examine the role of intervening ligands in photoinitiated intramolecular electron transfer [13].

In addition to the biochemical / biophysical studies conducted on intact or slightly modified photosynthetic systems extracted from biological sources protein pairs which are physiological partners are being used to gain insight into the mechanism of electron transport through biological molecules. An example of such a study is the substitution of various metallated porphyrins into the active site of the cytochrome *c* -

cytochrome *c* peroxidase protein-protein complex [14]. This experimental practice allows variation of the reaction free energy.

However, the interest in electron transfer reaction dynamics extends beyond the focus of natural photosynthesis. A better understanding of this fundamental reaction in natural and synthetic molecular assemblies will lead to more efficient photochemical devices, information storage devices, photoswitching assemblies, and conducting polymers. The need for a comprehensive reaction theory is critical.



## CHAPTER I

### References:

- 1     Mokteri, Chesnoy, and Labereau, *Chem. Phys. Lett*, **155**, (1989), 593
- 2     H.Sumii and R.Marcus, *J. Chem. Phys.*, **84**, (1986), 4894
- 3     G.C.Walker, E.Åkeson, A.E.Johnson, N.E.Levinger, P.F.Barbara,  
*J. Phys. Chem.*, **96**, (1992), 3728
- 4     K.Tominaga, D.A.V.Kliner, A.E.Johnson, N.E.Levinger, P.F.Barbara,  
*J. Chem. Phys.*, **98**, (1993), 1228
- 5     P.F.Barbara, G.C.Walker, T.P.Smith, *Science*, **256**, (1992), 975
- 6     E.Åkeson, G.C.Walker, P.F.Barbara, *J. Chem. Phys.*, **95**, (1991), 4188
- 7     C.Galli, K.Wynne, S.M.LeCours, M.J.Therien, and R.M.Hochstrasser,  
*Chem. Phys. Lett.*, **206**, (1993), 493
- 8     M.H.Vos, J.C.Lambry, S.J.Robles, D.C.Youvan, J.Breton, J.L.Martin,  
*Proc. Natl. Acad. Sci. USA*, **88**, (1991), 8885
- 9     K.Wynne, C.Galli, P.J.F.DeRege, M.J.Therien, and R.M.Hochstrasser,  
in *Ultrafast VIII*, editors J.L Martin, A.Migus, G.A.Mourou, A.H.Zewail,  
(Springer-Verlag, Berlin, New York, 1993)
- 10    J.N.Onuchic and P.G.Wolynes, *J. Phys. Chem.*, **92**, (1988), 6495

- 11 J.M.Jean, G.R.Fleming, and R.A.Friesner,  
*Ber. Bunsenges. Phys. Chem.*, **95**, (1991), 253
- 12 M.J.Therien, M.A.Selman, H.B.Gray, I.J.Chang, and J.R.Winkler,  
*J. Am. Chem. Soc.*, **112**, (1990), 2420-2422
- 13 T. Ohno, K.Nozaki, N.Ikeda, and M.Haga,  
in *Electron Transfer in Inorganic, Organic, and Biological Systems*,  
J.R.Bolton, N.Matagaga, and G.McLendon, editors  
American Chemical Society, Washington, D.C., (1991), 214-228
- 14 J.M.Nocek, N.Liang, S.A.Wallin, A.G.Mauk, B.M.Hoffman,  
*J. Am. Chem. Soc.*, **112**, (1990), 1623

**Figure I.1** Illustration of the potential energy surfaces involved in a direct electron transfer reaction. The bold, vertical arrow indicates a photoexcitation to an excited electronic surface. This state may, for example, be a charge transfer state as observed in molecular complexes. The dashed arrow indicates the electron transfer process.

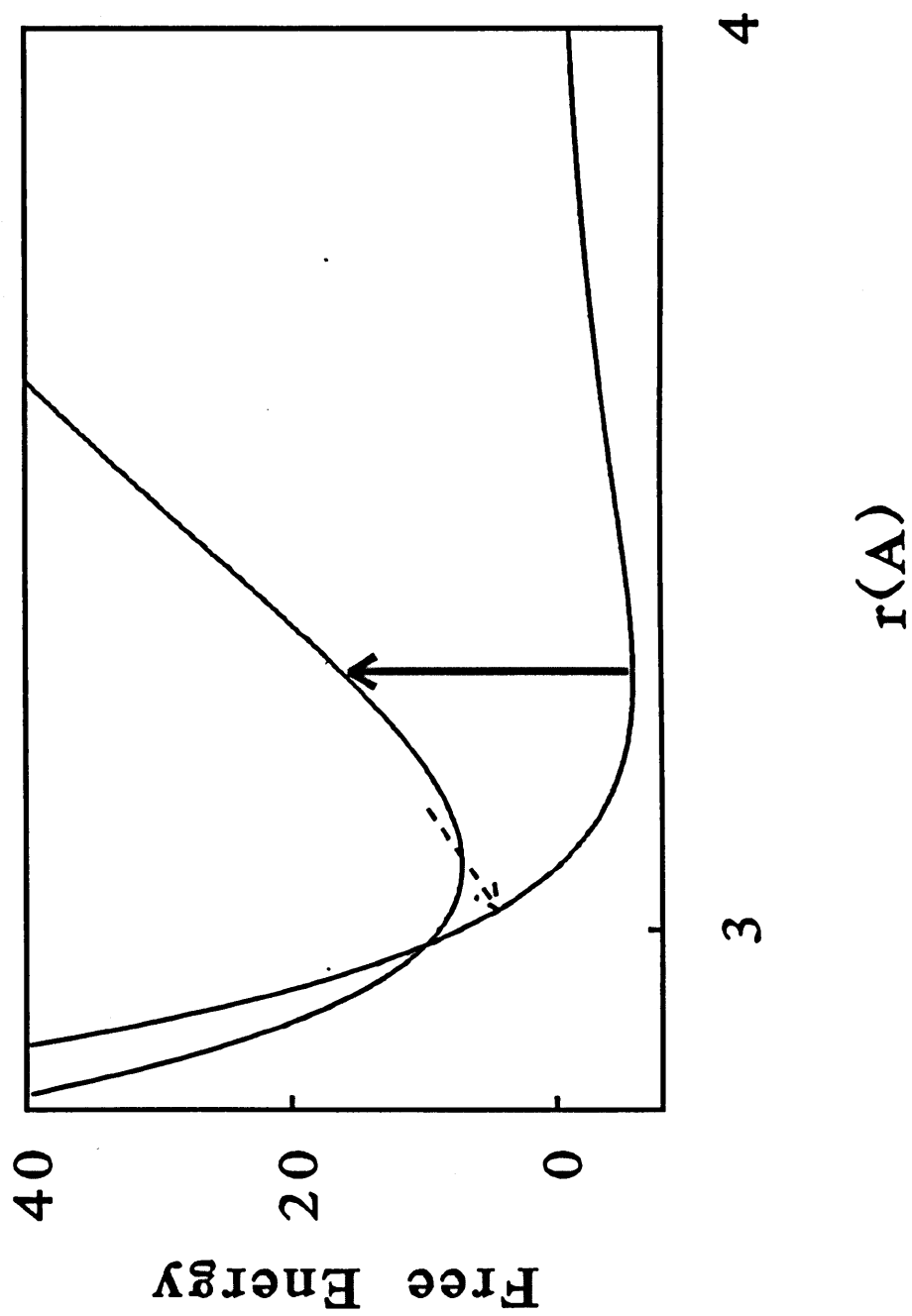
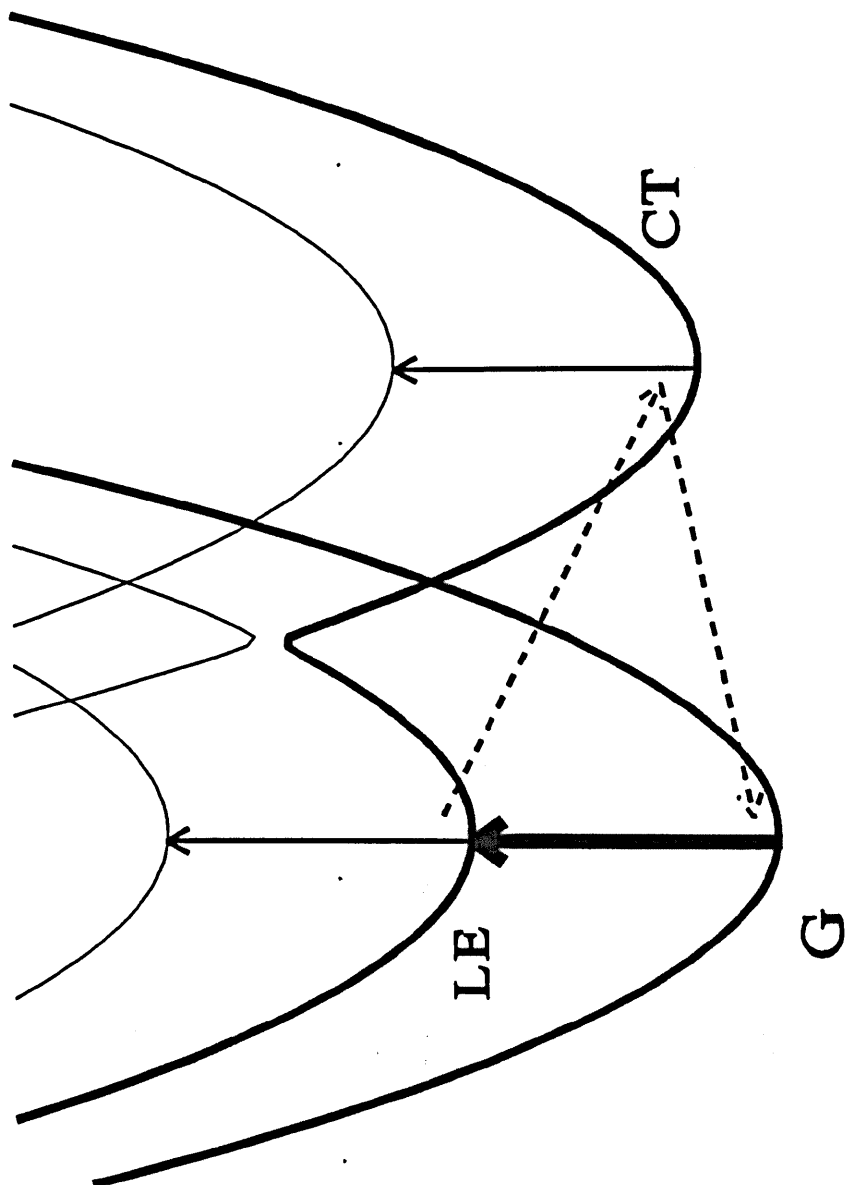


Figure I.2 Illustration of the potential energy surfaces involved in an indirect electron transfer reaction. The bold, vertical arrow indicates a photoexcitation to an eigenstate of the donor. This state is coupled to an ionic electronic state of the molecule pictured here on the right of the diagram. The thin, vertical arrows indicate the optical probes. The dashed arrows indicate the electron transfer processes. State labels: G, ground, LE, locally excited, CT, charge transfer.



**Figure I.3** Rough illustration of the molecular complex tetracyanoethylene-hexamethylbenzene (TCNE-HMB), an example of a species which undergoes direct photoinduced electron transfer. This process is discussed in Chapter I and Chapter IV.

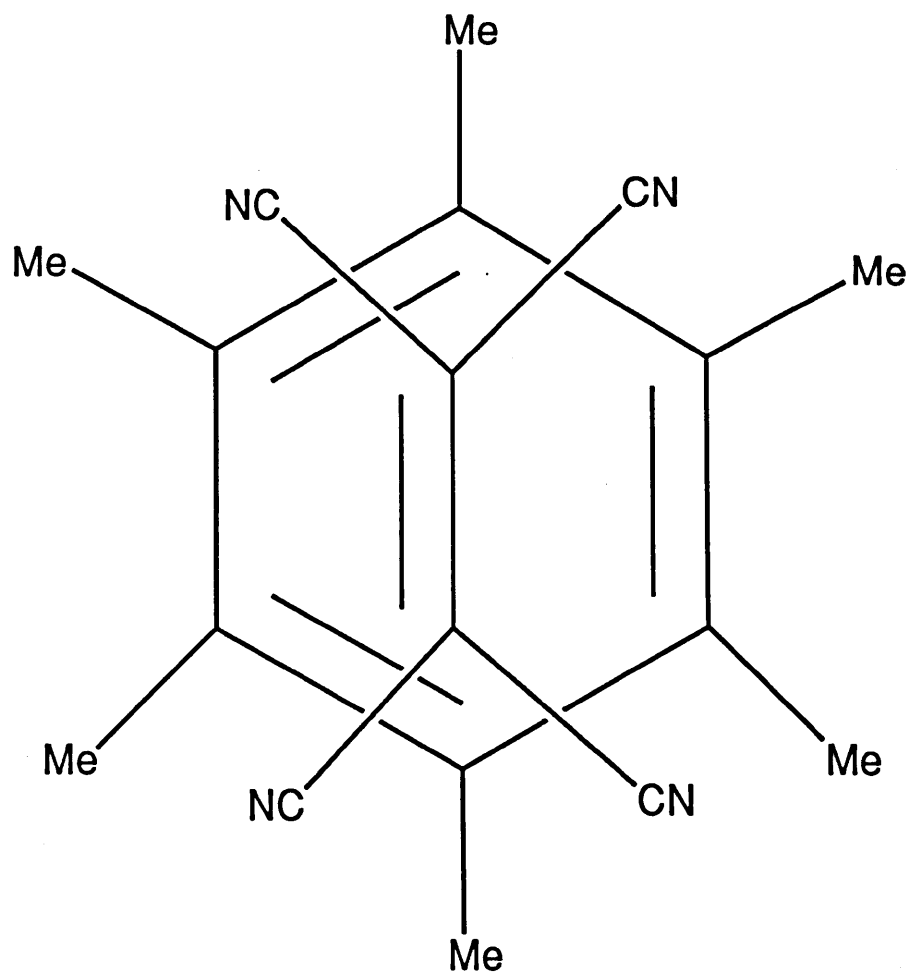
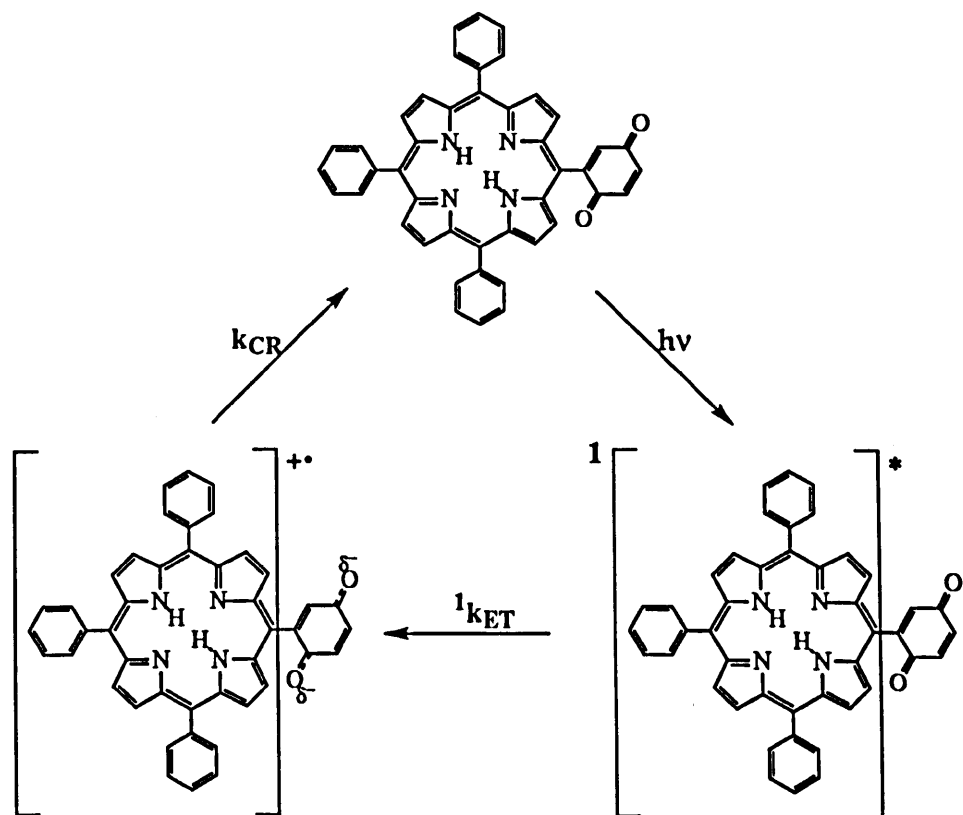




Figure I.4      Photoinduced reactions of the freebase porphyrinquinone. This species is an example of one exhibiting indirect photoinduced electron transfer as discussed in Chapter I and Chapter V. The optically prepared state is a local excitation of the porphyrin moiety,  $P^*Q$ . This state evolves to the charge transfer state  $P^+Q^-$ , indicated by the process  $^1 k_{ET}$  in the figure. The subsequent electronic relaxation is the charge recombination reaction, indicated by  $k_{CR}$  in the figure.



## Chapter II

### Electron Transfer Theory

#### Introduction:

The theory of electron transfer reactions, rooted in the absolute reaction rate theory developed by Eyring and coworkers in the 1930's [1], was pioneered and developed by R.A.Marcus in a series of papers published in the 1950's and 1960's [2-8]. This work was cited by the Nobel Committee upon awarding its prize in Chemistry to Marcus in 1992.

The post-WWII era was an active time in electron transfer kinetic investigations, owing in part to the application of electronic instrumentation generated by armament development to the measurement of fast electrochemical kinetics. Electron transfer reaction studies prior to this time were limited to slower time regimes such as observed in diffusion-controlled processes. This proliferation of electron transfer kinetic data resulted in a period of strong interplay between theory and experimentation which has continued to the present day.

Marcus not only identified the unique aspects of the electron transfer reaction with respect to the more intensely investigated bond rupture reaction, but developed expressions to quantify the contributions from these physical phenomena to the rate

expression. The electron transfer process generally involves a large charge separation which may be rapid with respect to the ability of the solvent modes to solvate this configuration of particles. The result is a nonequilibrium polarization condition in the reacting system, solvent barriers along angular and center of mass solvent coordinates, and free energy of solvation which is deposited in these modes. The role of the solvent polarization is central to Marcus' formulation of electron transfer dynamics.

In addition to the dominant role played by nonequilibrium polarization conditions in determining electron transfer kinetics, a related distinction between the bond rupture processes addressed by transition state theory and an electron transfer reaction is the higher dimensionality of the electron transfer reaction coordinate. The modes comprising the reaction coordinate include, in addition to the solvent modes described above and referred to as the exterior modes, a larger number of interior modes compared with a bond breaking reaction. As a simple example, consider the introduction of an electron into the lowest unoccupied molecular orbital ( LUMO) of a biologically important electron acceptor such as quinone. The delocalization of the LUMO results in the change of a number of equilibrium configurations of the interior modes. These shifts in equilibrium position of the many coupled interior and exterior modes result in a reaction coordinate of high dimensionality.

Bond rupture and subsequent mass transfer processes invariably proceed from reactant to product via an adiabatic transformation. Due to the large mass of the moiety transferred, the reacting pair in a bond rupture and atomic mass transfer reaction must

attain a separation on the order of a bond length. The resultant donor-acceptor electronic wavefunction overlap, reactant-product Coulombic repulsion, and exchange interaction is thus quite large with respect to the magnitude of these properties in electron transfer reactions. The exponential decay of the electronic wavefunction with respect to the molecular center allows the transfer of the electron over a longer range of reaction distances. The electronic wavefunction overlap and accompanying perturbation in this configuration can be quite small - small enough to describe the electronic wavefunction of the activated complex as a linear combination of the reactant and product electronic wavefunctions.

Each of the three distinctions of Marcus electron transfer theory versus absolute reaction rate theory: nonequilibrium polarization of the activated complex contribution to reaction dynamics, high dimensionality of the reaction coordinate, and nonadiabaticity of the electron transfer reaction will be discussed in more detail below.

## Nonequilibrium Polarization:

### Introduction:

Calculations of rate processes using absolute reaction rate theory had been executed with the assumption that the solvent configuration was in equilibrium with the charge distribution of the reactant transition state configuration [9-11]. Marcus was the first to calculate the contribution to electron transfer kinetics from the polarization coordinates [7]. As the unique property of the electron transfer reaction with respect to the bond rupture process is the nonequilibrium polarization of the transition state resulting in polarization barriers and energy to be transferred into polarization modes, the fundamental property to be determined is the electrical polarization function of reactants, activated complex, and products. This polarization of the activated complex may occur along all the component degrees of freedom and is, in general, comprised of electronic, atomic, and orientational contributions [2-5].

The polarization of the transition state may be considered to contain two components, the U-type, denoted by the vector function  $P_u(r)$ , and the E-type, denoted by the vector function  $P_e(r)$ .  $P_u(r)$  gives the magnitude and direction at point  $r$  of the polarization which is not in equilibrium with the charge distribution of the transition state.  $P_e(r)$  gives the magnitude and direction of the polarization which is in equilibrium with the transition state charge distribution. This equilibrium polarization at point  $r$  may be calculated from the electric field resulting from the transition state

charge distribution using equilibrium electrostatics. The total polarization is given by:

$$P(r) = P_u(r) + P_e(r) \quad (1)$$

The solvent degrees of freedom which store the activated complex polarization in general consist of electronic, translational, and orientational motions. The time scale for motion from a high potential energy configuration to an equilibrated state as the electron transfer reaction proceeds for these degrees of freedom ranges from something on the order of  $10^{-15}$  second for the electronic solvation to  $10^{-11}$  second for orientational solvation [3]. Each degree of freedom evolves from a contributor to  $P_u(r)$  to a contributor of  $P_e(r)$  on a different time scale.

If a reversible path is employed for reaching a nonequilibrium polarization state such as observed in the activated complex of an electron transfer reaction, the free energy associated with this state may be calculated [2]. Let the reversible work required to charge the system, in a vacuum, at infinite separation, be designated  $W_{iso}$ . The difference between this quantity,  $W_{iso}$ , and the electrostatic free energy,  $F$ , is the free energy arising from the interaction of the charges of the system with each other and with the polarized medium in the configuration of interest.

To calculate the free energy of the transition state, Marcus employs a two stage reversible charging process to create the activated complex nonequilibrium polarization state described by  $P(r)$ .

### Calculations:

The first step calculates the reversible work required to charge the system to a state which results in the final value of the nonequilibrium polarization, *i.e.* the U-type, which is denoted by  $P_u^0(r)$ . At the end of this first stage the equilibrium polarization, *i.e.* the E-type, attains a value denoted by  $P_e^0(r)$ . This is not the final value of the equilibrium polarization.

The second step holds the value of the nonequilibrium polarization function attained by the step one charging process fixed at  $P_u^0(r)$  while reversibly transforming the charge distribution to the final configuration of interest. Therefore during this transform the equilibrium polarization function evolves from its value at the end of stage one,  $P_e^0(r)$ , to its final value,  $P_e(r)$ . In order to derive an expression for the energy required to perform these charge transforms, an expression for the electrostatic potential is required.

The donor and acceptor molecules in a polarizable solvent comprise a system of charges and dipoles. The dipoles may exist for long times, for example the permanent dipoles of a polar solvent; for intermediate times such as the dipole between the donor cation and the acceptor anion, which persists for the time prior to the charge recombination; or for very short times, such as the dipole between the donor cation / acceptor anion and the electronic distribution of the polarizable medium, which equilibrates on the femtosecond time scale. The electrostatic potential for this system



of charges and polarized volumes, equilibrated along some degrees of freedom, but not others, can be written as a sum of contributions from the different components:

$$\psi(r') = \int \frac{\rho(r) dV}{|r-r'|} + \int \frac{\sigma(r) dS}{|r-r'|} + \int \frac{P(r) \cdot \nabla_r dV}{|r-r'|} \quad (2)$$

where  $\rho(r)$  expresses the charge density per unit volume at the point  $r$ , and  $\sigma(r)$  is the charge density per unit area at a surface element  $dS$  of an interface of a system. An example of such an interface is that existing in an electrode oxidation-reduction reaction.  $P(r)$  is the sum of the equilibrium and nonequilibrium polarization discussed above and expressed in equation II.1. The gradient operator subscript indicates the differentiation with respect to  $r$ .

Recall the work performed during stage one expresses the reversible charging of the system and results in the final value of the non-equilibrated polarization  $P_u^0(r)$ . This charging process is parameterized by  $\lambda$  which proceeds from its initial value of zero before the charging begins to its final value of one, indicating the completion of the stage one charging. The fractional value of any physical quantity during the stage one charging, such as the charge density  $\rho(r)$ , can be denoted

$$\rho^\lambda = \lambda \rho^0 \quad (3)$$

where  $\rho^0$  indicates the charge density per unit volume at the end of stage one.

In the absence of electrical saturation, the polarization of each mode is proportional to the local value of the electric field strength. This is true at all

increments of the stage one work:

$$P_e^\lambda = \alpha_e E^\lambda \quad (4)$$

$$P_u^\lambda = \alpha_u E^\lambda \quad (5)$$

In this regime of linear polarization, the work done in charging the system is calculated by expressing the change in charge density  $d\rho^\lambda$  in a volume element  $dV$ , plus the equivalent expressions for the surface charge and surface element  $d\sigma^\lambda$  and  $dS$ :

$$W = \int_\lambda \int_V \psi^\lambda \frac{d\rho^\lambda}{d\lambda} d\lambda dV + \int_\lambda \int_S \psi^\lambda \frac{d\sigma^\lambda}{d\lambda} d\lambda dS \quad (6)$$

If the value of the charge density per unit volume at the end of stage one is given by  $\rho^\circ$ , that of the surface charge per unit area  $\sigma^\circ$ , and the electrostatic potential  $\Psi^\circ$ , then the work done during this charging is given by integration over  $\lambda$  to yield:

$$W_I = \frac{1}{2} \int \Psi^\circ \rho^\circ dV + \frac{1}{2} \int \Psi^\circ \sigma^\circ dS \quad (7)$$

which is the final result for the stage one work.

The stage two charging process transforms the equilibrium polarization from its value at the end of stage one,  $P_e^\circ(r)$ , to its final value,  $P_e(r)$ . The work performed during this stage is the work required to change the charge distributions at the end of

stage one,  $\rho^0$  and  $\sigma^0$ , to their final values, denoted  $\rho(r)$  and  $\sigma(r)$ . As in the stage one charging, the stage two charging process will be parameterized by  $\lambda$  which will again serve as an integration variable. The charge density per unit volume and the charge density per unit area during this transformation can be respectively written:

$$\rho^\lambda = \rho^0 + \lambda (\rho - \rho^0) \quad (8)$$

and

$$\sigma^\lambda = \sigma^0 + \lambda (\sigma - \sigma^0) \quad (9)$$

Substituting equations II.8 and II.9 into the expression for the electrostatic potential given in equation II.2 yields the expression for the potential required to calculate the work performed during stage two:

$$\begin{aligned} \psi^\lambda(r) = & \int \frac{\rho^0 + \lambda(\rho - \rho^0) dV}{|r-r'|} + \int \frac{\sigma^0 + \lambda(\sigma - \sigma^0) dS}{|r-r'|} \\ & + \int \frac{(P_u^0 - \alpha_e \nabla \psi^\lambda) \cdot \nabla_r dV}{|r-r'|} \end{aligned} \quad (10)$$

where  $P_u^0(r)$  is the nonequilibrium polarization resulting from the stage one charging process and held constant during the stage two process, and  $\alpha_e \nabla \psi^\lambda$  is the equilibrium polarization at the stage  $\lambda$ .

The expressions for the charge density per unit volume and the charge density

per unit area given in equations II.8 and II.9, as well as the expression for the potential produced by  $(\rho(\mathbf{r}) - \rho^o)$  and  $(\sigma(\mathbf{r}) - \sigma^o)$  given by equation II.10, may introduced into the expression for the reversible work given in equation II.6. After the expression is integrated from  $\lambda = 0$  to  $\lambda = 1$ , Marcus attains the expression for the work done in transforming the equilibrium charges to their final value  $P_e(\mathbf{r})$ :

$$W_{II} = \frac{1}{2} \int (\psi + \psi^o) (\rho - \rho^o) dV + \frac{1}{2} \int (\psi + \psi^o) (\sigma + \sigma^o) dS \quad (11)$$

which is the final result for the stage two charging process.

The total work done in the two stages of charging is the electrostatic free energy,  $F = W_I + W_{II}$ , which can be written in terms of the final state of the system:

$$G = \frac{1}{2} \int \left[ \frac{\mathbf{E}_c \cdot \mathbf{E}_c}{4\pi} \mathbf{P} \cdot \mathbf{E}_c + \mathbf{P}_u \cdot \left( \frac{\mathbf{P}_u}{\alpha_u} - \mathbf{E} \right) \right] dV \quad (12)$$

where  $\mathbf{E}_c$  is the field exerted by the charges in vacuum,  $\mathbf{E}$  is the negative gradient of the electrostatic potential,  $\mathbf{P}$  is the total polarization given by equations II.4 and II.5, and  $\mathbf{P}_u$  is the nonequilibrated polarization in the system.

The quantity  $G$  in equation II.12 is the electrostatic free energy of a nonequilibrium state having U-type and E-type polarization. This nonequilibrium state in the dielectric degrees of freedom occurs when the charge transfer process occurs rapidly with respect to the dielectric solvation time. Such a nonequilibrium polarization condition is experimentally obtained by the rapid photoinduced electron transfer

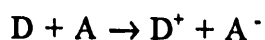
reactions detailed in this thesis.

This calculation is made in the dielectric unsaturation approximation. This means the dielectric polarization responds linearly to changes in the electric field as associated with any changes in charge distribution of the reacting complex. The electrostatic free energy thus is a quadratic function of the polarization coordinate [2,3,8,12].

### Coupling in the Electron Transfer Reaction

#### Introduction:

The electron transfer reaction may be expressed in general terms as:



which, in the absence of tunneling, occurs via an isoenergetic electronic transition as the system moves from the electronic state of the reactants to the electronic state of the products via the activated complex. The activated complex of the reaction is that configuration of nuclei including the solvent coordinates which occurs at the intersection of the reactant and product electronic energy surfaces. These surfaces and the coupling between them may be described using the Born-Oppenheimer description.

## Born-Oppenheimer Approximation:

### Diagonal Terms

In the Born-Oppenheimer approximation the full molecular Hamiltonian is decomposed into a sum of the Born-Oppenheimer electronic operator and the nuclear kinetic energy operator:

$$\mathfrak{H}(r_{el}; q_n) = H(r_{el}; q_n) + T(q_n) \quad (13)$$

This vibronic Hamiltonian is an operator of the vibronic wavefunction such that:

$$\mathfrak{H}(r_{el}; q_n) \Psi(r_{el}; q_n) = E \Psi(r_{el}; q_n) \quad (14)$$

where E is the total energy of the system and

$$\Psi(r_{el}; q_n) = \sum_i \phi_i(r_{el}; q_n) \chi_i(q_n) \quad (15)$$

Here,  $\{\phi_i(r_{el}; q_n)\}$  is an orthonormal set of electronic wavefunctions and  $\{\chi_i(q_n)\}$  are the nuclear wavefunctions functions. For example,  $\phi_i(r_{el}; q_n)$  may express the ground state electronic wavefunction of the reactant DA in an electron transfer reaction (see below).

The Born-Oppenheimer electronic potential energy surface for this state of the reactant  $\phi_i$  is given by the diagonal element:

$$H_{ii}(q_n) = \int \phi_i^*(r_{el}; q_n) H(r_{el}; q_n) \phi_i(r_{el}; q_n) d\tau_{el} \quad (16)$$

where the molecular energy operator  $H(r_{el}; q_n)$  includes the electron-electron repulsion, the electron-nuclear attraction, the nuclear-nuclear repulsion, and the electron kinetic energy.

This energy surface does not include the motion of the nuclei. The nuclear differential kinetic operator operating on the product wave function given in equation II.15 yields:

$$\langle \phi_i \chi_i | \nabla^2 | \phi_j \chi_j \rangle = \langle \phi_i \chi_i | \phi_j \chi_j'' + \phi_j'' \chi_j + 2 \phi_j' \chi_j' \rangle \quad (17)$$

where  $\nabla^2$  is the second differential operator, prime ' indicates single differentiation, and double prime '' indicates double differentiation. The first integral on the right hand side of equation II.17 does not involve differentiation of  $\phi$  with respect to  $q_n$ . This term, when  $i = j$ , gives the kinetic energy of the nuclei  $T_q$  in state  $\chi_i$  moving in a potential given by equation II.16. The adiabatic energy of this system is given by  $T_q + H_{ii}(q_n)$ .

The energy  $T_q + H_{ii}(q_n)$  is the result of an adiabatic approximation in the sense that the electronic energy  $H_{ii}(q_n)$  is calculated with fixed nuclei. The nuclei then move in this averaged electrostatic potential. Mathematically, this separation of motions is expressed by the parametric dependence of  $H_{ii}$  on  $q_n$ .

An addition to the diagonal energy is given by the second term of equation II.17 which expresses the nonadiabatic following of the electrons and nuclei:

$$T''_{ii}(q_n) = \int \phi_i^*(r_{el}; q_n) T(q_n) \phi_i(r_{el}; q_n) d\tau_{el} \quad (18)$$

### Off-diagonal Terms:

The electron transfer reaction is described in this representation by the off-diagonal matrix elements which couple the reactant and product vibronic wavefunctions. The electronic coupling matrix element is given by:

$$H_{ij}(q_n) = \int \phi_i^*(r_{el}; q_n) H(r_{el}; q_n) \phi_j(r_{el}; q_n) d\tau_{el} \quad (19)$$

which expresses the Coulombic repulsion between the reactant electronic wavefunction  $\phi_i^*$  and the product electronic wavefunction  $\phi_j$  as a parametric function of the nuclear coordinates. For weakly interacting species the reactant electronic wavefunction in an electron transfer reaction may be written as a product of the donor and acceptor electronic wave function at a given nuclear configuration:

$$\phi_i^*(r_{el}; q_n) \approx | D(r_{el}; q_n) A(r_{el}; q_n) > \quad (20)$$

The value of this product wavefunction increases as the donor-acceptor separation distance decreases. Similarly, the wavefunction of the result of the electron transfer reaction may be written as a product of the ionic species:

$$\phi_j(r_{el}; q_n) \approx | D^+(r_{el}; q_n) A^-(r_{el}; q_n) > \quad (21)$$



The electronic coupling matrix element  $H_{ij}(q_n)$  is at the center of one of the principle contributions to electron transfer reaction theory made by Marcus. Marcus realized that for a bond rupture and subsequent atomic mass transfer reaction, the donor-acceptor separation distance is small with respect to the donor-acceptor separation distances observed in electron transfer processes [2,7]. The subsequent large donor-acceptor electronic product wavefunction results in a large reactant-product electronic coupling matrix element for "... the usual bond rupture reaction which is almost invariably quantum mechanically adiabatic" [7]. In such a reaction the large  $H_{ij}(q_n)$  strongly couples the reactant and product electronic surfaces. The resulting splitting between the lower electronic surface and the upper electronic surface exceeds  $k_B T$ , the mean fluctuation energy per mode, making the upper surface thermally inaccessible. The probability of products proceeding to reactants upon attaining the activated complex configuration is near unity. This adiabaticity is expressed in the absolute reaction rate expression of transition state theory in which the pre-exponential frequency factor is the frequency of the dominant vibronic channel or a weighted average over the modes coupled to the electron transfer. The discussion of reaction rate expressions including comparisons of adiabatic and non-adiabatic rate expressions is continued below.

Continuing with the discussion of the off-diagonal terms of the Born-Oppenheimer approximation, the nuclear coupling matrix elements result from

differentiation of the electronic wavefunction  $\phi$  with respect to  $q_n$  and are expressed in the second and third terms of equation II.17. A complete expression for the nuclear coupling matrix element  $T''_{ij}$  follows from the second term of equation II.17:

$$T''_{ij}(q_n) = \int \phi_i^*(r_{el}; q_n) T(q_n) \phi_j(r_{el}; q_n) d\tau_{el} \quad (22)$$

The full expression for the nuclear coupling matrix element expressed in the third term of equation II.17 is :

$$T'_{ij}(q_n) = - \sum_q \frac{\hbar^2}{M_q} \left( \int \phi_i^*(r_{el}; q_n) \nabla q \phi_j(r_{el}; q_n) d\tau_{el} \right) \cdot \nabla q \quad (23)$$

where  $M_q$  is the effective mass associated with mode  $q$ . The sum extends over the modes of the system. The evaluation of this term is difficult as it requires an analytical expression for the electronic wavefunction of the reactants and products. In certain instances, however this term may be evaluated. An example of such an evaluation is the solution phase charge recombination study of the charge transfer species tetracyanoethylene (TCNE) - hexamethylbenzene (HMB) presented in this thesis.

The complete transition operator coupling the reactant state  $\phi_i$  and the product state  $\phi_j$  is given in this representation by the sum of the off-diagonal matrix elements:

$$\mathfrak{R}_{ij}(q_n) = H_{ij}(q_n) + T'_{ij}(q_n) + T''_{ij}(q_n) \quad (24)$$

### Dimensionality of Reaction Coordinate:

A rearrangement of charge within a nuclear framework such as the electron transfer reaction requires the reorientation of a large number of atomic masses compared to the bond ruptured - bond formed reaction [7]. While the reaction coordinate for the latter is described by a linear combination of the bond distances of those bonds broken and formed, a description of the electron transfer reaction requires inclusion of the change in bond lengths of the donor and acceptor modes experiencing a change in electric potential as a result of the new charge distribution as well as reorientations of the solvent degrees of freedom.

The electron transfer reaction is a radiationless transition between nondegenerate electronic states which occurs with highest probability at near isoenergetic phase regions. As this transition proceeds, the difference in electronic energy between the reactant and product,  $\sim \Delta G^0$ , is accepted by the nuclear modes comprising the reaction coordinate of the system. These components of the reaction coordinate may be conveniently partitioned into the **interior** modes of the system: those nuclear degrees of freedom involving motion of the atoms of the donor and/or acceptor, and the **exterior** modes of the system: those nuclear degrees of freedom involving motion of the atoms of the dielectric medium containing the reacting species.

### Exterior Modes:

As discussed above, the solvent degrees of freedom are comprised of electronic, atomic, and orientational modes. While the solvation of the electron transfer reaction product consists primarily of the energy required to reorient the permanent dipoles of the solvent, an expression for the reorganization energy of the solvent,  $\lambda_{OUT}$ , may be obtained within the confines of dielectric continuum theory. This model approximates the solvent as a dispersive continuum. The energy is given by:

$$\lambda_{out} = \frac{1}{2} \epsilon_0 \left[ \frac{1}{\epsilon_{\infty}} - \frac{1}{\epsilon_s} \right] \int (E^R - E^P)^2 dV \quad (25)$$

where  $\epsilon_0$  is the vacuum permittivity,  $\epsilon_{\infty}$  and  $\epsilon_s$  the optical and zero frequency dielectric constant, respectively,  $E^R$  the vacuum electric field resulting from the reactant charge distribution, and  $E^P$  the vacuum electric field resulting from the product charge distribution [1,13].

This expression may be evaluated using a spherical electron donor D and electron acceptor A. Integrating equation II.25 under these conditions then yields:

$$\lambda_s = \frac{(\Delta e)^2}{4\pi\epsilon_0} \left[ \frac{1}{2r_D} + \frac{1}{2r_A} - \frac{1}{r_{AD}} \right] \left[ \frac{1}{\epsilon_{\infty}} - \frac{1}{\epsilon_s} \right] \quad (26)$$

for two spheres of radius  $r_A$  and  $r_D$ , with center to center separation  $r_{AD}$  in a uniform dielectric medium where  $\Delta e$  is the charge transferred,  $\epsilon_{\infty}$  is the infinite frequency and  $\epsilon_s$  is the zero frequency dielectric constant of the solvent. Expressions for  $\lambda_{OUT}$  have

also been derived for geometries other than spherical reactants including elliptical species [13].

As an example of the solvent reorganization energies values obtained using equation II.26, this theoretical expression for  $\lambda_{\text{OUT}}$  has been evaluated with  $\Delta e = 1$  electron,  $r_D = 2.4 \text{ \AA}$ ,  $r_A = 1.9 \text{ \AA}$ , and  $r_{AD} = 3.35 \text{ \AA}$  for a wide range of solvents; these results are fully discussed in the chapter of this thesis concerning the charge recombination reaction of tetracyanoethylene (TCNE) and hexamethylbenzene (HMB) in solution. The stated molecular lengths are those measured by x-ray diffraction for crystalline TCNE - HMB. The solvent reorganization energies range from  $100 \text{ cm}^{-1}$  for the nonpolar  $\text{CCl}_4$  to  $2100 \text{ cm}^{-1}$  for propylene carbonate. There is good correspondence between these theoretical values found for  $\lambda_{\text{OUT}}$  and those from fitting the absorption spectra of TCNE-HMB in solution.

#### Interior Modes:

The interior modes of the system comprising the electron transfer reaction coordinate consist of donor and/or acceptor nuclear modes which must adjust to new equilibrium positions as a result of the product charge distribution. The bond lengths of the system may compress or lengthen, while torsional modes may undergo angular displacement.

The interior reorganization energy  $\lambda_{\text{IN}}$  is the energy required to give the system

the geometry of the product: that is, the work required to stretch, compress, or rotate a molecular bond to the product configuration. Using a harmonic approximation for the potential energy of the nuclear oscillators the total interior reorganization energy is given by summing the contributions from the normal modes comprising the reaction coordinate:

$$\lambda_{IN} = \frac{1}{2} \sum_i f_i (r_R^{eq} - r_P^{eq})^2 \quad (27)$$

where  $f_i$  is the reduced force constant for the  $i^{th}$  vibration, and  $(r_R^{eq} - r_P^{eq})$  is the difference in the bond equilibrium position for the reactant and product [13].

In cases where the charge separated state is accessed directly by a photon the reorganization energy of the interior modes,  $\lambda_{IN}$ , which are Raman active, may be experimentally estimated by measuring resonance Raman excitation profiles. Under the assumptions of harmonic vibrations, no inhomogeneous broadening, and no coordinate dependence of the transition dipole moment, the Raman cross section  $\sigma_R$  at the excitation frequency  $E_L$  is given by [14-16]:

$$\sigma_{R, i-f} (E_L) = \frac{E_L E_s^3 n^2 \Delta^2 (< n > + 1)}{h^2 c^2 \pi} |A_0(E_L) - A_0(E_L - \hbar\omega)|^2 \quad (28)$$

where  $E_s$  is the energy of the scattered photon,  $n$  is the solvent refractive index,  $< n >$

$\langle \dots \rangle$  is the average thermal occupation number at temperature  $T$  given by  $[e^{(\hbar\omega/kT)} - 1]^{-1}$ ,  $\omega$  is the vibrational frequency,  $A_0$  is the Kramers-Kronig transform of the absorption spectrum (see below) and  $\Delta$  is the dimensionless shift of the equilibrium position of the mode discussed below.

Consider a normal stretching coordinate  $Q$  such that:

$$Q = \mu^{\frac{1}{2}} r \quad (29)$$

where  $\mu$  is the reduced mass of the vibration and the bond length is given by  $r$ . The dimensionless coordinate is given by:

$$q = \left( \frac{\mu\omega}{\hbar} \right)^{\frac{1}{2}} r \quad (30)$$

The reorganization energy of this mode within the given model is:

$$\lambda = \frac{\hbar\omega\Delta^2}{2} \quad (31)$$

The Kramers-Kronig transform  $A_0(E_L)$  of the optical absorption spectrum is given by [15,17]:

$$A_0(E_L) = P \int_0^\infty \frac{\sigma_A(E)}{E(E-E_L)} dE + i\pi \frac{\sigma_A(E_L)}{E_L} \quad (32)$$

where  $\sigma_A(E)$  is the absorption cross section at energy  $E$ .  $P$  denotes the principle part of the integral. This can be evaluated analytically from a digitized absorption spectrum [18].

While the model above clearly demonstrates the dependence of the Raman cross section on the coordinate shift of the mode in question, the inapplicability of the above expressions to experimental situations where inhomogeneity and non-Condon effects ( i.e. dependence of electronic transition moment on nuclear coordinate) are contributory may require a time -dependent wavepacket approach [19-21, 22-26]. The absorptive cross section  $\sigma_A$  as a function of excitation frequency  $E_L$  is given by :

$$\sigma_A(E_L) = \frac{\pi^3 e^2 E_L M_0}{3 n h^2 c^2} \sum_i \int_{-\infty}^{\infty} d\delta G(\delta) * \text{Re} \int_0^{\infty} dt \langle \chi_i | \chi(t)_i \rangle e^{i(E_L + \epsilon_i + \delta)t} e^{-\gamma(t)} \quad (33)$$

where  $M_0$  is the transition length of the species at the equilibrium position,  $P_i$  is the initial Boltzmann distribution, and the sum extends over the vibrational modes of the molecule indexed by  $i$  with zeropoint energy  $\epsilon_i$ . The inhomogeneous distribution of electronic energies is given by the function  $G(\delta)$ . The function  $\langle \chi_i | \chi_i(t) \rangle$  expresses the correlation between  $|\chi_i\rangle = (M(q)/M_0)|i\rangle$  and  $|\chi_i(t)\rangle$  which is equal to  $e^{-iHt}|\chi_i\rangle$ . The exponential evolution operator propagates  $|\chi_i\rangle$  on the excited surface via the excited state vibrational Hamiltonian  $H$  for a time  $t$ .  $M(q)$  is the position dependent electronic transition length which may be expanded as a Taylor series about its value at the equilibrium nuclear configuration and  $|i\rangle$  is the ground



state vibrational wave function.

The function  $e^{-g(t)}$  expresses the damping of the correlation which in the condensed phase arises principally from the solute - solvent interactions which damps the electronic transition. In the frictionally damped oscillator model [27,28], where  $D$  represents the coupling strength between the solvation coordinate and the transition and the solvent time scale is  $\hbar / \Lambda$  :

$$g(t) = g_R(t) + i g_I(t) \quad (34)$$

$$g_R(t) = \left( \frac{D^2}{\Lambda^2} \right) \left[ e^{-\frac{\Lambda t}{\hbar}} - 1 + \frac{\Lambda t}{\hbar} \right] \quad (35)$$

$$g_I(t) = \frac{D^2}{2k_B T \Lambda} \left( 1 - e^{-\frac{\Lambda t}{\hbar}} \right) \quad (36)$$

The solvent reorganization and resultant Stokes shift arises from the response of the solvent molecules to the chromophore and is expressed in the imaginary component  $g_I(t)$  of the damping function  $g(t)$  [29,30]. The damping of the integrand from the real part of  $g(t)$  interpolates between an exponential damping resulting in a Lorentzian absorption line shape for fast solvents and / or weak coupling (  $\Lambda \gg D$  ) and a Gaussian damping resulting in a Gaussian absorption line shape in the slow solvent and / or strong coupling (  $\Lambda \ll D$  ) regime [31].

The expression for the resonance Raman cross section at this level of

approximation is:

$$\sigma_{R \rightarrow f}(E_L) = \frac{8\pi e^4 E_L E_S^3 M_0^4}{\hbar^6 c^4} \int_{-\infty}^{\infty} d\delta G(\delta) * \left| \int_0^{\infty} dt \langle \chi_i | \chi(t)_i \rangle e^{i(E_L + \epsilon_i + \delta)t} e^{-\gamma(t)} \right|^2 \quad (37)$$

The transform model, equations II.28 and II.32, and the wavepacket model, equations II.33 and II.37, were used in conjunction by Markel et al. [32] to measure the equilibrium shifts and reorganization energies of the interior modes coupled to the electron transfer reaction in the molecular complex tetracyanoethylene-hexamethylbenzene. These measurements were used in the analysis of the transient spectral data presented in chapter IV of this thesis.

#### Reaction Coordinate Parameters:

Figure II.1 (following this chapter) depicts an intersection of two free energy electronic surfaces: the reactant surface which in the case of an indirect electron transfer photoprocess is a local excitation of the donor or acceptor, and the product surface which is the polar electronic state. The multidimensional reaction surface has been cut along a single coordinate here labeled  $q$ . This coordinate may be an interior mode of the system thus representing a rearrangement of the nuclear framework of the donor-acceptor skeleton or an exterior mode representing a rearrangement or movement along a solvent degree of freedom. For a high frequency mode of greater than or equal

to  $\sim 1000 \text{ cm}^{-1}$  a more complete picture would be attained with the inclusion of quantized vibrational states. These are omitted here for generality.

This model [12] is in effect a Boltzmann weighted profile of the reacting system as the local potential energy minima corresponding to different solvent contributions have been summed over resulting in a smoothed surface which is approximated as a quadratic function of  $q$ .

The zero of the free energy is here defined by the minimum of the reactant surface drawn in the left of Figure II.1. This minimum also defines the zero of the mode  $q$ . Upon charge transfer the new equilibrium position of the mode is  $\Delta$ , while the work done to attain this configuration is the reorganization energy  $\lambda$ . The driving force for the reaction  $\Delta G$  is the difference between the free energy minima of the two surfaces.

In the presence of an electronic coupling element  $H_{RP}$  which may arise from Coulombic coupling as discussed above in the context of Born-Oppenheimer states or via exchange matrix elements, the diagonalization of the uncoupled reactant and product parabolic surfaces results in surfaces as those given in Figure II.1. The result of this coupling is two states: the lower surface, which for  $q$  less than or  $\sim$  equal to zero is essentially the reactant electronic configuration, and the upper surface. The probability of an electronic transition from the lower to the upper surface depends upon the magnitude of the element  $H_{RP}$ . For an equilibrated ensemble at the configuration of the activated complex indicated by  $q_x$  in Figure II.1, the population with free energy

sufficient to attain the electronic configuration of the upper surface relative to the population at  $q_x$  on the lower surface with the transition state energy is:

$$\frac{P(q_x; G^* + H_{RP})}{P(q_x; G^*)} = e^{-\frac{H_{RP}}{k_B T}} \quad (38)$$

For electronic splittings of greater than or on the order of  $\sim k_B T$  the motion of an equilibrated ensemble is essentially along the lower surface. This issue is addressed in the following section which examines reaction rate expressions.

#### Reaction Rates:

##### Adiabatic

A conceptual milestone in the quantitative study of reaction rate expressions was Arrhenius' late nineteenth century formulation of the proportionality of the reaction rate constant,  $k$  to the ensemble fraction possessing the transition state energy [33]:

$$k = A e^{-E^*/k_B T} \quad (39)$$

Subsequent development of expressions for rate constants required more detailed considerations of  $A$ , the preexponential or frequency factor, and  $E^*$ , the energy of activation.

The transition state theory, also known as the theory of absolute reaction rates or activated complex theory, has been associated with the work of Eyring since his

seminal publications in the 1930's [34-40]. Building upon the results of Tolman who clearly applied statistical mechanics to rate processes and thereby defined the activation energy [41], Eyring developed rate expressions for equilibrated ensembles which include an explicit expression of the pre-exponential factor A. As the fraction of species with energy between E and E + dE is calculable via Boltzmann statistics, transition state theory formulates a rate expression in terms of vibrational partition functions.

Consider a reaction in which two species A and B come together to form a activated complex which then dissociates into products:



The adiabatic rate expression can be written as a function of the thermodynamic equilibrium constant  $K_+$  which expresses the concentration of the transition state per concentration of the reactants:

$$K_+ = \frac{c^*}{c_A c_B} \quad (41)$$

The adiabatic rate expression represents the reaction as proceeding from the activated complex to products with unit probability. The system attains the activated configuration via a fluctuation in a suitable coordinate. In this treatment of reaction rates the coordinates describing the system are classical modes. If the dissociative mode of the complex is given as  $\nu$ , the adiabatic rate  $k_{Ad}$  is given by:

$$k_{Ad} = \nu K_s \quad (42)$$

The evaluation of the thermodynamic reaction equilibrium constant proceeds by expressing the concentration equilibrium constants as partition functions. The vibrational partition function per unit volume of a mode  $i$  is written with respect to the zero point energy of that mode:

$$\frac{q_i}{V} = f_i e^{-\frac{\epsilon_0^i}{k_B T}} \quad (43)$$

The thermodynamic constant is written in terms of the energy of activation of the reaction:

$$K_s = \frac{f_s}{f_A f_B} e^{-\frac{\Delta E^\ddagger}{k_B T}} \quad (44)$$

where the molecular partition function  $f$  is a product of the translational, rotational, and vibrational normal degrees of freedom.

The product partition function  $f$  may be factored to isolate the dissociative mode  $\nu$ :

$$f_s = f^* f_\nu \quad (45)$$

An explicit expression for  $f_\nu$  is obtained using the partition function of a harmonic oscillator:

$$f_v = \frac{e^{\frac{-h\nu}{2k_B T}}}{1 - e^{\frac{-h\nu}{k_B T}}} \quad (46)$$

In the regime  $h\nu \ll kT$  the numerator of the harmonic oscillator partition function is  $\sim 1$  and the denominator exponential may be expanded such that:

$$f_v = \frac{h\nu}{k_B T} \quad (47)$$

The transition complex partition function may now be written:

$$f^* = \frac{h\nu}{k_B T} f^* \quad (48)$$

Substituting these expressions for the equilibrium constant into the adiabatic rate expression yields the Eyring equation:

$$k_{Ad} = \frac{k_B T}{h} \frac{f^*}{f_A f_B} e^{\frac{-\Delta E^*}{k_B T}} \quad (49)$$

Nonadiabatic:

As discussed earlier in Chapter II, electron transfer reactions often occur nonadiabatically: the distance between the donor and acceptor moieties can be tens of Angstroms resulting in a small donor - acceptor overlap of electronic wavefunction and a concomitant small electronic coupling matrix element with respect to  $k_B T$ . The above rate expression for adiabatic reaction processes may be modified for application to nonadiabatic reactions *i.e* to express the reformation of the reactants by the activated complex by including a semiclassical electronic nonadiabaticity parameter  $\kappa$ .

An expression for  $\kappa$  was derived by Landau [42] and Zener [43] to express the probability of an electronic transition between weakly coupled states. These zero order Born-Oppenheimer states and the electronic coupling matrix elements responsible for transitions between them are detailed in the discussion of electronic wavefunctions earlier in this chapter. The probability for the system to remain on the lower electronic surfaces each time the system transverses the crossing region is given by:

$$P = 1 - e^{\frac{-4\pi^2 H_{RP}^2}{hV |s_R - s_P|}} \quad (50)$$

where  $H_{RP}$  is the electronic coupling matrix element discussed earlier in this chapter,  $h$  is Planck's constant,  $V$  is the velocity of the system at the transition region, and  $|s_R - s_P|$  is the absolute value difference between the forces exerted by the reactant and product potential energy functions experienced at the crossing region.

When  $H_{RP}$  is very small the exponential term in equation II.50 approaches 1 and



P approaches zero. The reactant and product surfaces are not electronically coupled therefore no transition is possible via this matrix element. When  $H_{RP}$  becomes large the exponential in equation II.50 tends toward zero and P approaches unity. The splitting in the crossing region between the upper and lower electronic surface has become larger than the available energy for fluctuations thereby making the upper electronic surface thermally inaccessible.

When the velocity of the system V through the transition configuration is large the probability P of remaining on the lower surface tends toward zero. There is little time spent in the transition configuration therefore the reaction temporal window is small. Also in the denominator of the exponential is an expression regarding the curvature of the potential energy functions of the reactant and product. When  $|s_R - s_P|$  is large the Landau-Zener  $Q_{LZ}$  region is small. The distribution in the conjugate variable  $p_Q$ , the momentum along this degree of freedom, is uncertainty broadened expressing a large fraction of systems with insufficient kinetic energy to attain the transition geometry and a large fraction of systems with large kinetic energy thereby attaining the upper electronic surface.

Using a cycle averaged velocity over a harmonic oscillation the Landau - Zener probability for remaining on the lower electronic surface may be rewritten for harmonic potentials:

where  $\langle v \rangle$  and  $\langle \lambda \rangle$  are suitable averages over the coupled reaction modes frequencies and reorganization energies respectively [44a,44b].

$$P = 1 - e^{\frac{-\pi^{\frac{3}{2}} H_{RP}^2}{\hbar \langle v \rangle \sqrt{\langle \lambda \rangle k_B T}}} \quad (51)$$

Marcus Reaction rate:

As the electronic coupling matrix element which perturbs the zero order reactant and product surfaces is small with respect to  $k_B T$ , first order quantum perturbation theory is applicable to the derivation of a nonadiabatic electron transfer rate. The result of this calculation is a Fermi Golden rule expression [12, 45-46]:

$$k_{NA}^{(1)} = \frac{2\pi}{\hbar} |H_{RP}|^2 (FC) \quad (52)$$

where  $H_{RP}$  is the electronic coupling element detailed above and (FC) is the thermally weighted sum of the Frank-Condon factors per unit energy given by:

$$FC = Q^{-1} \sum_{i,f} e^{-\frac{E_i}{k_B T}} |\langle i | f \rangle|^2 \delta(E_f - E_i + \Delta E) \quad (53)$$

The nuclear partition function for this degree of freedom in the initial state is  $Q$ , the overlap of the  $|i\rangle$  initial and  $|f\rangle$  final vibrational wavefunctions is given by  $\langle i | f \rangle$ ,  $\Delta E$  is the energy of reaction,  $E_f$  the energy of the final state, and  $E_i$  the energy of the

initial state.

For low frequency modes of the reactive complex such as those associated with orientational motion of polar solvents,  $h\nu / k_B T \rightarrow 0$  and FC is given by:

$$FC = (4\pi\lambda k_B T)^{-\frac{1}{2}} e^{-\frac{(\Delta E + \lambda)^2}{4\lambda k_B T}} \quad (54)$$

where  $\lambda$  is the reorganization energy of the low frequency mode.

There are large entropic changes associated with polar solvent reorientation accompanying the electron transfer process to accommodate the new charge distribution [47]. The expression above for FC in the classical limit can be adapted to allow for a significant  $\Delta S^0$  accompanying a new solvent configuration by summing over the solvent modes and writing:

$$FC = (4\pi\lambda_S k_B T)^{-\frac{1}{2}} e^{-\frac{(\Delta G^0 + \lambda_S + (E_f - E_i))^2}{4\lambda_S k_B T}} \quad (55)$$

where the subscript S has been added to explicitly denote the low frequency, classical mode, and the subscripts i and f denote the initial and final states of the high frequency, quantized modes. This expression assumes harmonic oscillations for the quantized modes of the system with no frequency change accompanying the electron transfer reaction. No harmonic approximation is employed for the classical modes.

The first order perturbation rate constant is then given by:

$$k^{(1)} = \sum_{n,m} P_n k_{nm}^{(1)} \quad (56)$$

where the sum is over all the initial (n) and final (m) quantized vibrational states involved in the process and  $P_n$  denotes the initial distribution of the quantized modes.

The rate constant for each pathway is given by:

$$k_{nm}^{(1)} = \frac{2\pi |H_{RP}|^2}{\hbar \sqrt{4\pi\lambda_s k_B T}} \prod_v |<n_v|m_v>|^2 \exp\left\{-\frac{(\Delta G^0 + \lambda_s + (m_v - n_v) \hbar\omega_v)^2}{4\lambda_s k_B T}\right\} \quad (57)$$

where the index  $v$  indicates the normal, quantized modes coupled to the electron transfer reaction.

The rate expressions above are not applicable to situations when the experimentally observed electron transfer times are comparable to the longitudinal dielectric relaxation time  $\tau_L$  [46] of the solvent indicating a charge transfer reaction occurring over nonequilibrated modes of the reaction coordinate. In continuum theory:

$$\tau_L = \frac{\epsilon_\infty}{\epsilon_s} \tau_D \quad (58)$$

where  $\epsilon_\infty$  is the high frequency dielectric constant,  $\epsilon_s$  is the zero frequency dielectric constant, and  $\tau_D$  is the Debye relaxation time which corresponds to the characteristic orientational correlation decay time of the solvent.

The explicit inclusion of the dielectric relaxation time  $\tau_L$  in the rate constant

for condensed phase electron transfer reactions was given by Jortner and Bixon :

$$k^{JB} = \sum_{n,m} P_n k_{nm}^{JB}, \quad k_{nm}^{JB} = \frac{k_{nm}^{(1)}}{1 + A_{nm}},$$

$$A_{nm} = \prod_v \frac{4\pi |H_{RP}|^2 |\langle n_v | m_v \rangle|^2 \tau_L}{\hbar \lambda_s}, \quad (59)$$

where  $k_{nm}^{(1)}$  is the result of the Golden rule calculation above and  $P_n$  is the initial distribution in the reactant vibrational manifold.  $A_{nm}$  is the solvent nonadiabaticity parameter which is directly proportional to the relaxation time of the dielectric continuum bath.

## Chapter II

### References:

- 1 H.Eyring, *J. Chem. Phys.*, **3**, (1935), 107
- 2 R.A.Marcus, *J. Chem. Phys.*, **24**, (5), (1956), 966
- 3 R.A.Marcus, *J. Chem. Phys.*, **24**, (5), (1956), 979
- 4 R.A.Marcus, *J. Chem. Phys.*, **26**, (1957), 867
- 5 R.A.Marcus, *J. Chem. Phys.*, **38**, (1963), 1858
- 6 R.A.Marcus, *J. Chem. Phys.*, **29**, (1963), 1734
- 7 R.A.Marcus, *Ann. Rev. Phys. Chem.*, **15**, (1964), 155
- 8 R.A.Marcus, *J. Chem. Phys.*, **43**, (2), (1965), 679
- 9 R.A.Marcus, *J. Chem. Phys.*, **44**, (1966), 1024
- 10 K.J.Laidler and M.King, *J. Chem. Phys.*, **87**, (1983), 2657
- 11 D.G.Trular, W.L.Hase, and J.T.Hynes, *J. Chem. Phys.*, **87**, (1983), 2664
- 12 R.A.Marcus and N.Sutin, *Biochim.et Biophys. Acta*, **811**, (1985), 265
- 13a R.D.Cannon, *Chem. Phys. Lett.*, **49**, (1977), 299
- 13b B.S.Brunschwig, S.Ehrensens, and N.Sutin,  
*J. Phys. Chem.*, **90**, (1986), 3657
- 14 J.B.Page and D.L.Tonks, *J. Chem. Phys.*, **75**, (1981), 5694

- 15 A.B.Myers and R.A.Mathies in, *Biological Applications of Raman Spectroscopy*, editor T.G.Spiro (Wiley, New York, 1987) Volume 2, p.1
- 16 E.J.Heller, *Acc. Chem. Res.*, **14**, (1981), 368
- 17 J.R.Cable and A.C.Albrecht, *J. Chem. Phys.*, **84**, (1986), 1969
- 18 C.K.Chan and J.B.Page, *J. Chem. Phys.*, **79**, (1983), 5234
- 19 S.Y.Lee and E.J.Heller, *J. Chem. Phys.*, **71**, (1979), 4777
- 20 D.J.Tannor and E.J.Heller, *J. Chem. Phys.*, **77**, (1982), 202
- 21 A.B.Myers, R.A.Mathies, D.J.Tannor and E.J.Heller, *J. Chem. Phys.*, **77**, (1982), 3857
- 22 A.B.Myers, R.A.Harris, and R.A.Mathies, *J. Chem. Phys.*, **79**, (1983), 603
- 23 A.B.Myers and R.A.Mathies, *J. Chem. Phys.*, **81**, (1984), 1552
- 24 A.B.Myers, M.O.Trulson, J.A.Pardoen, C.Heeremans, J.Lugtenburg, and R.A.Mathies, *J. Chem. Phys.*, **84**, (1986), 633
- 25 X.Ci and A.B.Myers, *Chem. Phys. Lett.*, **158**, (1989), 263
- 26 X.Ci, M.A.Periera, and A.B.Myers, *J. Chem. Phys.*, **92**, (1990), 4708
- 27 W.B.Bosma, Y.J.Yan, and S.Mukamel, *Phys. Rev. A*, **42**, (1990), 6920
- 28 S.Mukamel, *Ann. Rev. Phys. Chem.*, **41**, (1990), 647
- 29 R.F.Loring, Y.J.Yan, and S.Mukamel, *J. Chem. Phys.*, **87**, (1987), 5840
- 30 Y.J.Yan and S.Mukamel, *J. Chem. Phys.*, **89**, (1988), 5160
- 31 J.Sue, Y.J.Yan and S.Mukamel, *J. Chem. Phys.*, **85**, (1986), 462

- 32 F. Markel, N.S. Ferris, I.R. Gould, A.B. Myers,  
*J. Am. Chem. Soc.*, **114**, (1992), 6208
- 33 S. Arrhenius, *J. Phys. Chem.*, **4**, (1889), 226
- 34 H. Eyring, *J. Chem. Phys.*, **3**, (1935), 107
- 35 H. Eyring, *Chem. Rev.*, **17**, (1935), 65
- 36 H. Eyring and Polanyi, *Z. Phys. Chem. Abt. B.*, **12**, (1931), 279
- 37 H. Eyring and W.F.K. Wynne-Jones, *J. Chem. Phys.*, **3**, (1935), 492
- 38 H. Eyring, *J. Chem. Phys.*, **3**, (1935), 107
- 39 H. Eyring, H. Gershinowitz, and C.E. Sun, *J. Chem. Phys.*, **3**, (1935), 786
- 40 J.O. Hirschfelder, H. Eyring, and B. Topley, *J. Chem. Phys.*, **4**, (1936), 170
- 41 R.C. Tolman, *J. Am. Chem. Soc.*, **42**, (1920), 2506
- 42 L. Landau, *Physik Z. Sowjetunion*, **2**, (1932), 46
- 43 C. Zener, *Proc. Roy. Soc., London*, **A137**, p.696, **A140**, p.660, (1933)
- 44a N.S. Hush, *Coord. Chem. Rev.*, **64**, (1985), 135
- 44b N.S. Hush, *Electrochimica Acta*, **13**, (1968), 1005
- 45 J. Jortner, *J. Chem. Phys.*, **64**, (1976), 4860
- 46 J. Jortner and M. Bixon, *J. Chem. Phys.*, **88**, (1988), 167
- 47 R. Marcus and P. Siders, *J. Phys. Chem.*, **86**, (1982), 622



Figure II.1 Illustration of intersecting parabolic free energy surfaces along a mode  $q$ . The shift in equilibrium position is denoted  $\Delta$ . The difference in electronic energy between the reactant and product is  $\Delta G^0$ , the driving force of the reaction. The Born-Oppenheimer electronic coupling between the surfaces is denoted  $H_{RP}$  (see equation II.19). The reorganization energy for this mode  $q$  is  $\lambda$ . See text for further details.

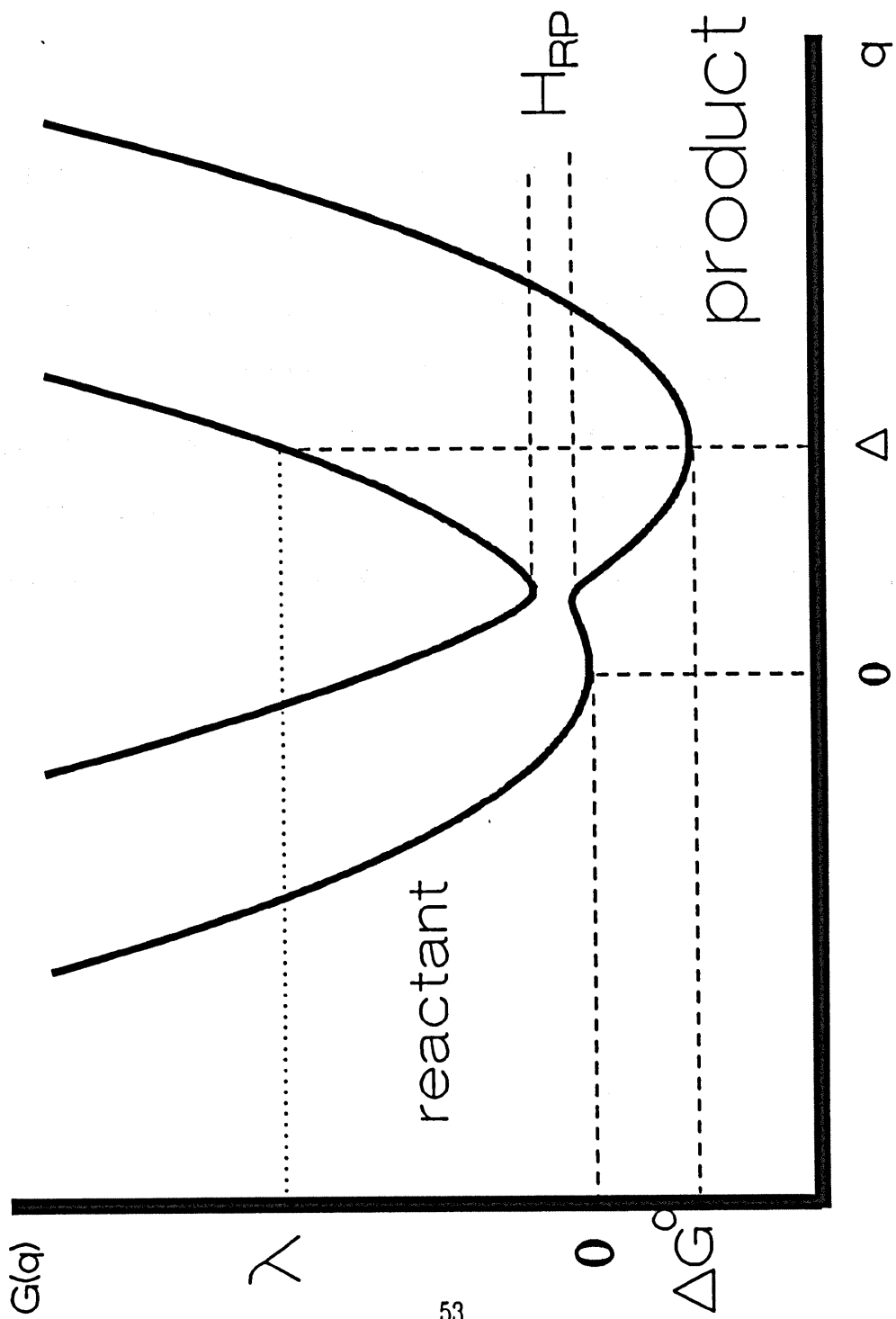


Figure II.2 Solvent (acetonitrile) reaction coordinate for the charge recombination reaction of tetracyanoethylene-hexamethylbenzene (TCNE-HMB). The bold, vertical arrow indicates a rapid excitation of the system to the excited electronic surface. At the arrow head, the solvent is not in equilibrium with the molecular charge distribution. The system undergoes dielectric polarization relaxation by proceeding from the Frank-Condon region, at the arrow head, to the minimum of the upper surface. The free energy difference between these two points is the solvent reorganization energy,  $\lambda_s$ .

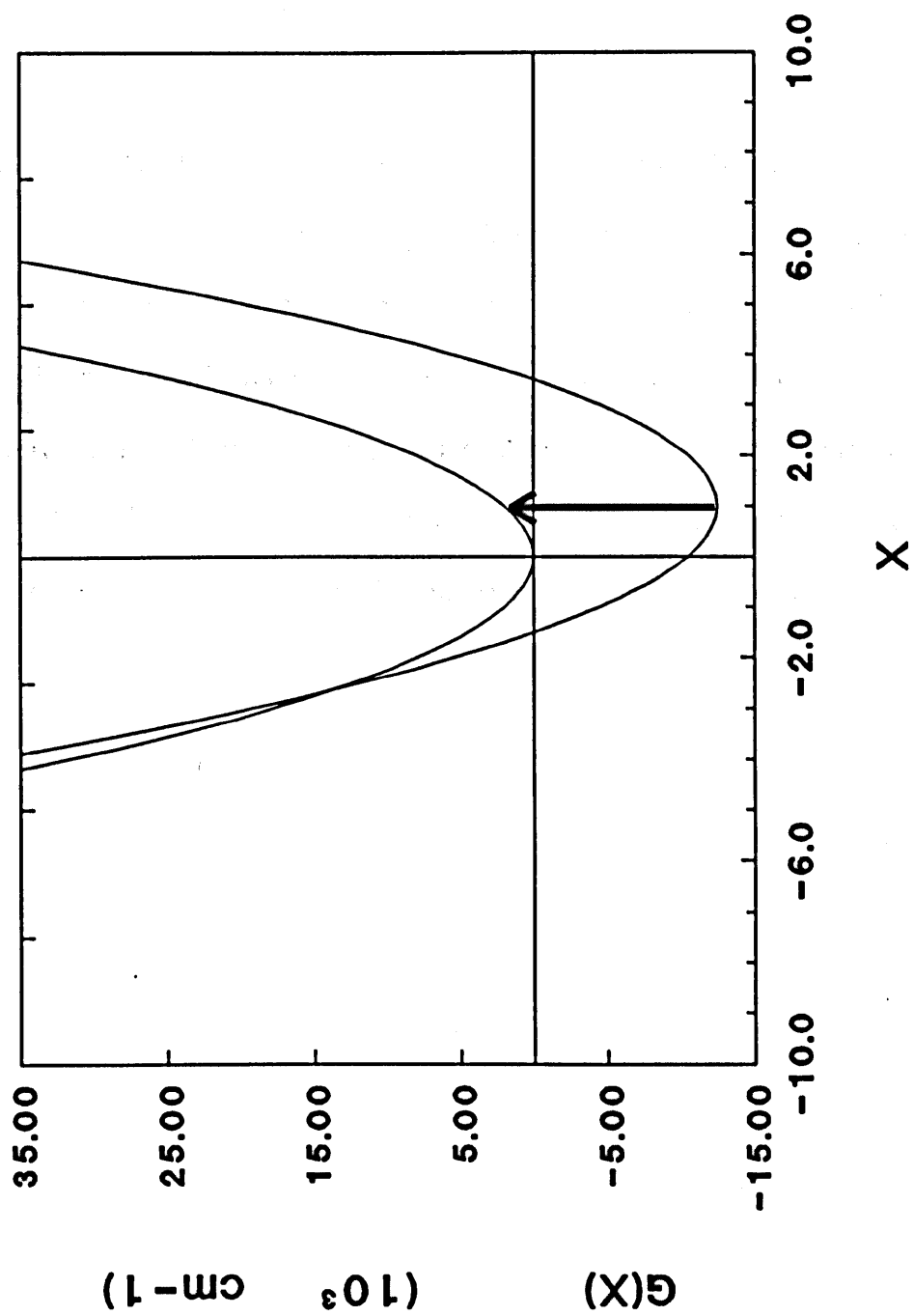


Figure II.3 Solvent (benzonitrile) reaction coordinate (X) for the charge recombination reaction of tetracyanoethylene-hexamethylbenzene (TCNE-HMB). The bold, vertical arrow indicates a rapid excitation of the system to the excited electronic surface. The multiple, lower surfaces depict the classical solvent coordinate with, respectively from the lowest surface, 0, 1 or 2 quanta in a high frequency reaction mode ( $1551\text{ cm}^{-1}$ ). Together with the reactant distribution, these product states comprise the vibronic transitions of the charge recombination reaction.

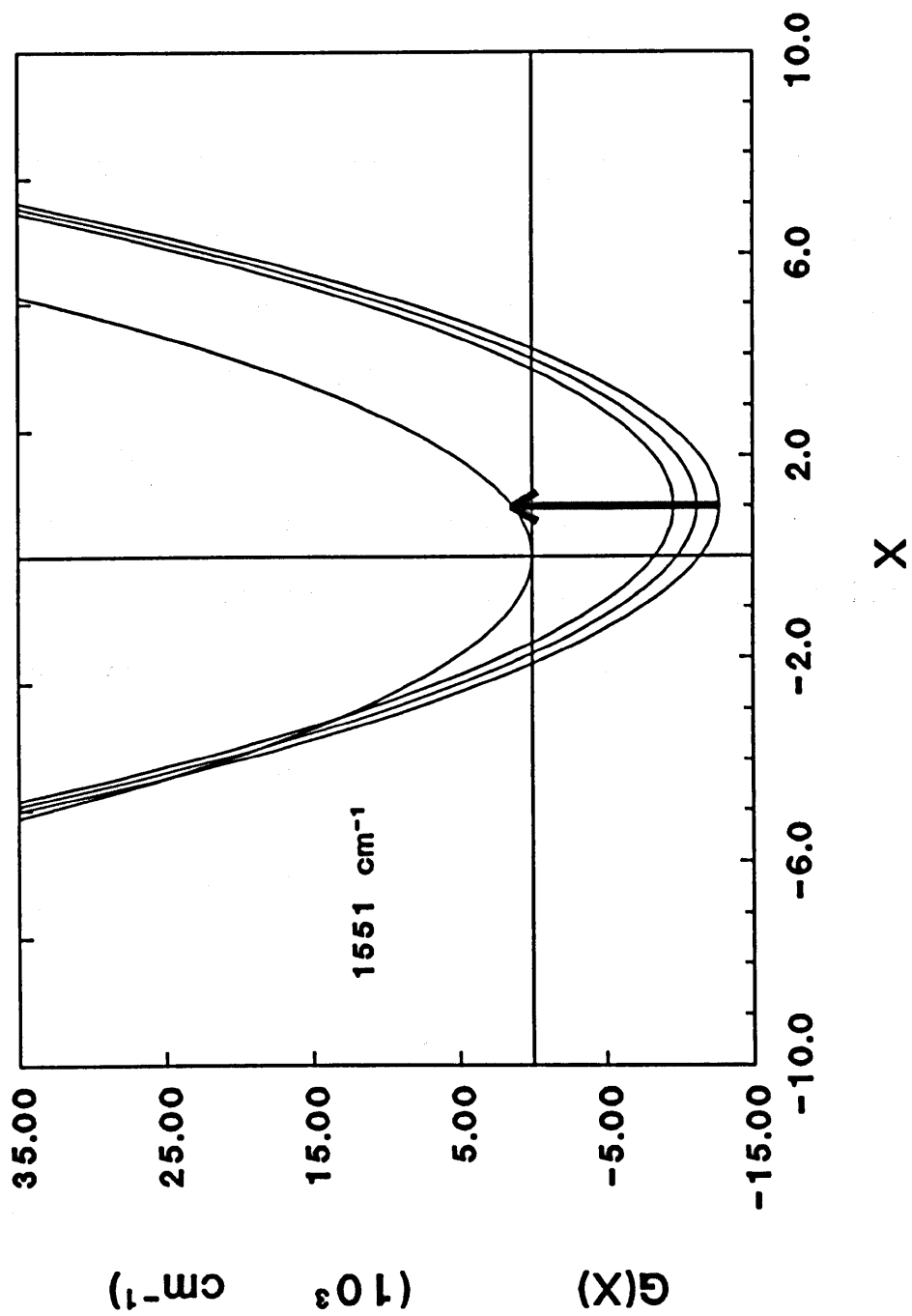
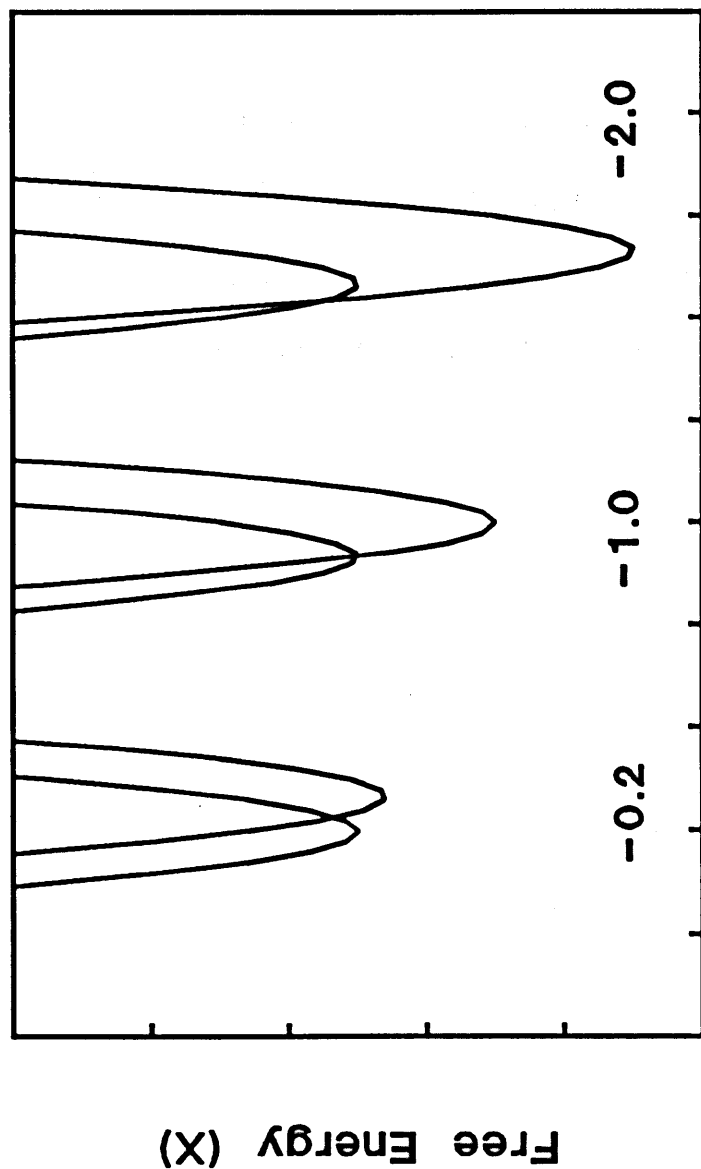
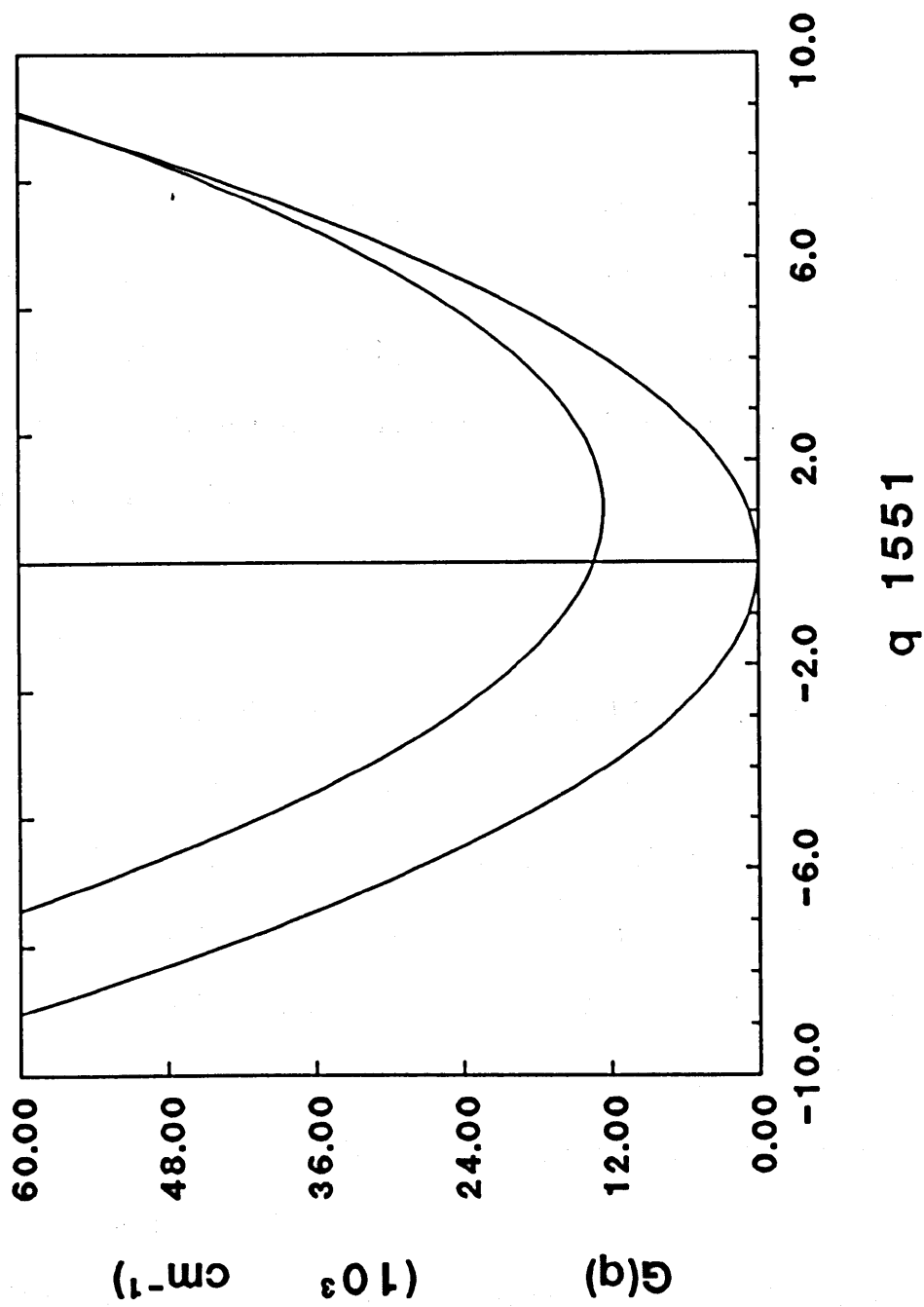


Figure II.4 Classical free energy surfaces depicting different Marcus reaction regimes. The curvature is the same for all depicted curves. The number indicated in the figure is the driving force / reorganization energy. In each set of surfaces, the reaction proceeds from the left well to the right; the reactions are exothermic. The small reaction barrier in the leftmost pair goes to zero as the driving force increases to the magnitude of the reorganization energy in the center pair. Further increase of the driving force, depicted in the right most pair of reaction surfaces, moves the reaction into the "inverted" regime with the increase of the barrier.





**Figure II.5** Reaction coordinate along the high frequency mode ( $1551\text{ cm}^{-1}$ ) for the charge recombination reaction of TCNE-HMB in acetonitrile. Depicted is a plot of harmonic ground and excited state surfaces using reaction parameters from resonance Raman investigations as described in Chapter II. Quantized vibrational states are not shown.



## CHAPTER III

### Experimental Methods

An electron transfer in the porphyrin based reaction centers of the blue-green alga *Rhodobacter Sphaeroides* occurs in 3 ps, while the longitudinal solvation time of a typical polar solvent such as tetrahydrofuran is  $\sim 1.4$  ps. The investigation of the initial processes of electron transfer in native and model systems in solution requires subpicosecond temporal resolution.

#### Time Resolved Spectrometer:

The femtosecond time resolved data presented here were collected using a colliding pulse mode locked laser (CPM) fabricated and developed in this laboratory following the design of Fork, Greene, and Shank (Figure III.1)[1-3]. This ring dye laser uses a flowing jet of Rhodamine 6G (aka Rhodamine 590) in ethylene glycol as the oscillator's lasing medium. At a concentration of 1-2 mM, the 300  $\mu\text{m}$  thick stream attenuates approximately 95% of the 514 nm pump light from the Coherent CR15 argon ion laser. Satisfactory stability and average power in the CPM is observed at Ar+ transmissions of 5 - 12%.

The Coherent CR15 is operated in the single line lasing mode of 514 nm at an

average power of 2 - 5 W. This pumping power must be adjusted to the gain of the resonator cavity which is strongly dependant upon the optical thickness of both the gain and saturable absorber media. The preferred transverse mode of the ion laser is  $TEM_{00}$  though this mode is not crucial. Satisfactory CPM performance may occur even though the argon ion emission displays some  $TEM_{01}$  or "doughnut" character.

The gain jet is situated near the focus of a  $<10^\circ$  z fold of the argon pump light; two 10 cm focal length mirrors are at the apices of the fold. Proper alignment of the gain jet in this beam waist, is critical for reliable performance of the dye laser. When the gain jet is placed at the focus of the waist thermal lensing is apparent in the far field image. The waist distortion is also observable on the downstream focussing mirror. Substantial improvement is attained by translating the jet out of the focus, into the diverging region of the argon beam. The far field image is used here to acquire a sharp, round image.

The gain jet's transverse and rotational degrees of freedom are also critical. As the laminar flow variation over the jet may be considerable, it is important to find a suitable, quiet spot in the gain jet. The pump beam to jet angle of incidence should be near Brewster's angle. This is attained by rotating the jet while observing the laser reflection spots off the front and rear jet face. These reflection spots are round and of equal intensity at the proper jet orientation angle.

The gain medium's fluorescence is focussed in the cavity by two 10 cm focal length mirrors coated for maximum reflectance at 619 nm. This is the nominal lasing

wavelength of the CPM. The resonator's three flat reflectors define the ring of the oscillator. Two of these mirrors are optimized for  $45^\circ$  incidence and 619 nm, while the third, optimized for 634 nm and  $0^\circ$  reflectance, contains the 1.3% transmitting output coupler.

Configured as detailed here the dye laser operates in the continuous wave (cw) mode. When the cavity is tuned as described, the output is  $\sim 150$  mW (cw) at the fluorescence maximum of the gain dye modified by the oscillator's mirror spectra.

Mode locked operation of the CPM is attained with the addition of a saturable loss medium. The saturable absorber 3,3' - Diethyloxadicarbocyanine (DODCI) in ethylene glycol in a stainless steel Coherent jet nozzle modified to about a  $15\text{ }\mu\text{m}$  opening provides the (passive) modelocking mechanism in this CPM. A concentration of  $\sim 1.0$  gram per liter yields a small signal loss of  $\sim 20\%$ . The backing pressure of both the saturable absorber and the gain dye was  $20 \pm 3$  psi.

The saturable absorber jet is situated at or near the focus of a  $\sim 5^\circ$  z fold , between two 5 cm focal length mirrors. Since the saturable absorber jet is the principal loss medium in the oscillator, the laser's performance is strongly dependent upon the placement of this jet within the beam waist. While the angular orientation of the jet is adjusted toward Brewster's angle as described for the gain jet above, the degree of saturation of the DODCI may be varied by the proximity to the focussed waist. Combined with the physical thickness of the jet in the cavity, which is adjusted by translation, these degrees of freedom chiefly determine the oscillator bandwidth.

As the temporal width of an optical pulse is inversely proportional to the spectral bandwidth it is desirable to tune the cavity to lase on the broadest bandwidth. The frequency components of the pulse must then be brought to the transform limit by varying the sign and magnitude of the group velocity dispersion (GVD) within the dye laser cavity [4-9]. This is accomplished in the CPM by adjustments to the intracavity four prism sequence. The amount of fused silica in the resonator is varied by translating the prism orthogonally to the laser beam, while the GVD is adjusted by altering the distance between the prisms (see below). Proper cavity tuning resulted in pulses as short as 40 fs with typical experimental values of 55 - 70 fs.

As described, the CPM output consists of a stable train of sub-100 fs pulses. The lasing wavelength may be varied over a limited range from about 610 to 630 nm. The repetition rate is  $\sim 100$  MHz, depending on the cavity length, with an average power of  $\sim 10$  mW. The power figures for the laser strongly depend not only on the resonator alignment but also on the chemical degradation of the gain and saturable media.

The principal noise sources of the CPM are the dye jets and the argon ion pump laser. The effects of variation in jet pressure, fluctuations in gain and/or saturable absorber thickness, and low frequency jet oscillations are observable with a optical photodiode and oscilloscope. These diagnostics are then used to adjust pump pressure and jet orientation to diminish noise. The limit of the pulse envelope fluctuations of the colliding pulse modelocked laser is determined by the noise of the argon ion laser

(ref 1). The pulse energy fluctuation was  $\sim 5\%$ , more than adequate to perform the desired spectroscopic experiments.

The CPM, however, has two rather critical shortcomings. The pulse energy is quite small - about 100 pJ per pulse or  $3 \times 10^8$  photons per pulse at 620 nm. Thus to attain a 5% excitation in a fairly concentrated biological sample of 1 mM, with an optical path of 1 mm to retain the desired temporal resolution, the beam would have to be focussed to a waist of  $\sim 2 \mu\text{m}$ .

The other weakness of this laser is the lack of tunability. Both the  $S_0 \rightarrow S_1$  and  $S_1 \rightarrow S_0$  transitions in polyatomic molecules are quite broad - consider, for example, the  $\sim 3800 \text{ cm}^{-1}$  spectral width of the  $S_0 \rightarrow S_1$  transition of a typical porphyrin. A tunable probe source is required for an extended spectroscopic investigation of polyatomic species.

Both CPM shortcomings are overcome by pulse amplification. Amplification provides not only more excitation photons, but the high peak power pulses may also be used to generate new probe frequencies.

### Multipass Amplification

Continuum generation to generate new probe frequencies requires peak powers on the order of  $10^{12} \text{ W/cm}^2$ . Thus for a waist of  $10 \mu\text{m}$ , the CPM seed pulse must be

amplified with a gain of  $\sim 10^3$ . This figure was surpassed in this laboratory by the fabrication and development of a copper vapor laser (CVL) pumped multipass amplifier in which gains of  $1 - 5 \times 10^5$  were routinely attained.

The amplifier was constructed using the design considerations of Knox, Downer, Fork, and Shank (Figure III.3) [10,11]. The gain medium of the amplifier is Rhodamine 640 perchloride. The amplification and beam quality of the amplifier depends strongly on the solvent of the gain medium - the gain dependence as a result of the solvent dependent fluorescence and the beam quality chiefly due to the solvent's heat capacity. After much experimentation with alcohols and Ammonyx detergents the optimized results were observed in a 40:60 V:V mixture of methanol : water. The amplifier operated at concentrations of  $\sim .4$  g of Rhodamine 640 / L of solvent which yielded an attenuation of the CVL light of  $\sim .9$ .

The amplifier is pumped by the copper vapor laser (Metalaser 251) operating at 8 kHz. This oscillator nominally produced 20 watts of average power distributed over two lines: one at 510 nm and the other at 578 nm which are absorbed in the wings of the amplifier gain medium. The specified 20 watts, however, was rarely attained - more typical was an average power of 12 watts which decayed to an output of approximately eight watts over a ten hour period. This laser, which had a down fraction of greater than .5 over a five year period, was the uncontested weak link of the spectrometer.

A 30 cm focal length lens is used to focus the output of the CVL to a spot size



of about 1 mm. The gain dye flows rapidly through a 2 mm quartz cell - the velocity of the dye solution was such so as to refresh the CVL pumped volume between shots. Since there is a considerable amount of energy deposited in the gain medium with each CVL pulse, *i.e.*  $\sim 1\text{-}2$  mW, the rapid flow rate is required to diminish thermal lensing and other beam distorting processes. The dye was cooled using a coil immersed into the 2 L reservoir of the gain medium. The coil contained a flowing solution of ethylene glycol and water at  $0^{\circ}\text{C}$ .

The amplifier was initially configured with a gain dye jet. The jet nozzle was coated with polished sapphire; the jet opening was 1.25 mm thick. Substitution by a closed quartz cell, however, resulted in a substantial reduction in gain fluctuation particularly in the sub-100 Hz region.

Since the CVL pulses are on the order of 10 - 20 ns, the six passes of the seed pulse from the CPM through the gain cell must occur with a propagation length of not more than  $\sim 4$  meters. This is accomplished by using a "bow-tie" arrangement of the seed beam with respect to the gain cell (Figure III.3). The CVL pumps the gain cell at near normal incidence, thus the seed beam incidence must also be at a small angle with respect to the cell normal to maximize the overlap of the CPM beam with the excitation volume. The seed beam incidence was between 10 and 20 degrees. The CVL pulse and CPM pulse are manually synchronized by an adjustable delay pulse generator used to fire the copper vapor laser. A 60 Mhz oscilloscope used to observe the amplified pulse energy is sufficient to optimize the CVL trigger delay with respect

to the amplified beam's power and noise characteristics.

Lensing within the amplifier is employed to vary the spot size with respect to pass. Thus each pass has a slightly different waist within the amplifier gain cell and samples different regions of the excitation volume. The initial amplifier lens focal length is 200 mm which corrects the 2 mrad divergence of the CPM and gently focusses to a spot of  $\sim 250 \mu\text{m}$  for passes one and two. After the second pass, a 100 mm lens is employed to increase the spot size to  $\sim 500 \mu\text{m}$  for passes three and four.

Following pass four the amplified CPM beam (ACPM) is strongly focussed by a 2 cm lens into a  $300 \mu\text{m}$  jet of malachite green / ethylene glycol solution to attenuate the amplified spontaneous emission (ASE). The ASE spectrum is roughly the fluorescence spectrum of the Rhodamine 640 in a water : methanol mixture which is slightly to the blue of the ACPM. The malachite green solution more strongly attenuates the ASE than the ACPM resulting in a  $< 1\%$  component of ASE in the output of the amplifier.

After the malachite green saturable absorber is a collimating lens of focal length 2 cm. Fine positioning of this lens resulted in a spot size of  $\sim 1 \text{ mm}$  for passes five and six. A weak telescope following the amplifier reduces the divergence to  $< 2 \text{ mrad}$ .

As mentioned above, the net gain of the amplifier was on the order  $1 - 5 \times 10^5$ , corresponding to a pulse energy of  $1 - 5 \mu\text{J}$ . The gain varied not only as a result of the CVL average power but also according to the spectrum of the CPM. As the CPM spectrum is shifted to the blue, around 610 nm, the highest gains are observed as a

result of the proximity of the Rhodamine 640 fluorescence. There is a trade - off between high gains around 610 nm and short pulses around 625 nm.

As a result of the dispersive materials used in the amplifier, particularly the solvents of the gain and saturable absorber, the temporal width of the laser pulse increases by a factor of two : from the CPM value of 50 - 70 fs to the amplified 100 - 140 fs. It is necessary, therefore, to compress the pulse temporally.

### Pulse Compression

A frequency dependent delay line comprised of prism quartets or grating pairs provides the pulse compression required to maintain transform-limited pulses in spectrometers containing dispersive materials [1-4]. A prism quartet, such as found in the cavity of the CPM and discussed above, is an optical component whose GVD may be set at negative or positive values as required.

The first prism spatially disperses the optical pulse into the frequency components. The red and blue edge of the pulse's spectrum thus have a different path length to the second prism of the sequence. The output of the second prism is a collimated spectrum. The remaining prisms then reverse the transverse dispersion to yield a collimated beam. The ray propagation of the beam through the pulse compressor is given by [12-16]:

where  $P$  is the optical path length,  $L$  is the distance between the first two prisms,  $n$  is

$$\frac{d^2P}{d\lambda^2} = 4L \left( \left[ \frac{d^2n}{d\lambda^2} + \left( 2n - \frac{1}{n^3} \right) \left( \frac{dn}{d\lambda} \right)^2 \right] \sin\beta - \right. \\ \left. 2 \left( \frac{dn}{d\lambda} \right)^2 \cos\beta \right) \quad (1)$$

the refractive index of the prism material, and  $\beta$  is the angular dispersion of the laser beam.

For quartz prisms such as found in the CPM a distance  $L$  of  $\sim 28$  cm is required to transform the pulse. Following the amplification of the CPM a compressor is used to return the temporal width of the pulse to 50 - 70 fs. A pair of SF10 prisms at a separation  $L \sim 48$  cm is used in a double pass arrangement. This optical element provides satisfactory compression. The restoration of the temporal width to  $\sim 60$  fs, combined with the average pulse energy of 2.5  $\mu$ J, results in a peak power of  $\sim 40$  MW. Focussed to a waist of 10  $\mu$ m this pulse yields a peak energy density of  $4 \times 10^{13}$  W / cm<sup>2</sup> - more than sufficient to generate additional probe frequencies through continuum generation.

### Continuum Generation

When an optical pulse of sufficient intensity propagates through a transparent, nonlinear medium, the initial properties of the pulse are modulated. This modulation results from the interaction of the pulse with the polarization induced in the material.

The induced polarization may be expressed in a general way as a series expansion in the applied field:

$$P = \epsilon_0 \chi^{(1)} E + \chi^{(2)} E E^* + \chi^{(3)} E E^* E + \dots \quad (2)$$

where  $P$  is the macroscopic polarization,  $E$  is the electromagnetic field,  $\epsilon_0$  the vacuum dielectric permeability,  $\chi^{(1)}$  is the linear susceptibility, and  $\chi^{(2)}$  and  $\chi^{(3)}$  represent the weaker, higher order interactions. As the susceptibilities are frequency dependent,  $\chi^{(1)}$  describes the variation of phase velocity with respect to frequency in the material. The intensity of the second harmonic polarization depends on  $\chi^{(2)}$ , while  $\chi^{(3)}$  is the parameter of interest for self - focusing, induced birefringence, and the phenomena responsible for increasing the bandwidth of the pulse, self-phase modulation (SPM).

For a material with inversion symmetry,  $\chi^{(2)}$  vanishes, leaving a dielectric displacement  $D$  through third order given by:

$$D = \epsilon_0 [ 1 + \chi^{(1)} + \epsilon_0^{-1} \chi^{(3)} E E^* ] E \quad (3)$$

Thus the total dielectric constant  $\epsilon$  ( $= D / E$ ) can also be written as a function of field strengths. Using its relationship with the optical frequency dielectric constant, the optical frequency refractive index  $n$  experienced by the optical wave is given by:

$$n = n_0 + n_2 \langle E E^* \rangle \quad (4)$$

where the brackets indicate the time average.

The phase of the electric field associated with the optical pulse at a time  $t$  and point  $z$  is written:

$$\theta(t) = \omega t - kz = \omega \left( t - \frac{nz}{c} \right) \quad (5)$$

where  $\omega$  is the optical frequency,  $k$  is the wave vector, and  $c$  the vacuum speed of light. The instantaneous phase is given by the time derivative of  $\theta$ :

$$\frac{d\theta}{dt} = \omega \left( 1 - \frac{n_2 z}{c\epsilon_0} \frac{dI}{dt} \right) \quad (6)$$

Thus sharply rising or falling pulse edges experience large frequency sweeps proportional to the nonlinear refractive index  $n_2$ .

The self-phase modulation in a number of materials was experimentally examined for efficiency in generating probe frequencies from the ACPM fundamental. Solid state materials such as SF6 and SF10 quartz generated a spectral broadening of over a factor of ten which decayed in tens of minutes due to thermal effects. The best results were observed in a 2 mm flow cell of ethylene glycol. At energy densities of  $\sim 2 \times 10^{12}$  W/cm<sup>2</sup> the self-phase modulation in ethylene glycol generated probes for

time resolved experiments over an  $\sim 8000 \text{ cm}^{-1}$  range around the ACPM fundamental at 620 nm. The visual output from the flow cell is white.

Due to dispersion, the ACPM pulse is temporally broadened by a factor  $>10$  in the ethylene glycol cell. The probe wavelength is selected using a bandpass interference filter of 10 nm spectral width. A double pass prism pair, as described above, compresses the probe over this 10 nm width to 40 - 70 fs, depending on the center frequency. The shorter pulses were observed in the far wings of the continuum spectrum. The complete spectrometer is shown in Figure III.4.

The self-phase modulation of the optical pulse in the ethylene glycol cell is accompanied by other nonlinear effects, including self-focussing, which prohibit compression over the full bandwidth of the modulated pulse. Full compression may be achieved, however, if the spectral broadening is performed in an optical fiber.

#### Optical Fibers:

In the far field, a pulse spectrally broadened via self-phase modulation in a bulk material generally displays a strongly inhomogeneous image across the beam. This inhomogeneity may include a speckle pattern indicating a localized, small scale self-focussing referred to in the optical literature as filaments. This irreversible beam decomposition prohibits transform limited compression.

The self focussing of optical pulses is a result of the radial distribution of high

peak intensities from mode-locked lasers. As shown in equation III.4, the index of refraction experienced by the wavefront of a pulse is a function of the intensity. In materials where  $n_2 > 0$  the higher intensity central portion of the beam will experience a larger index of refraction than will the spatial wings. The material is converted into a lens as a result of this interaction. This beam distortion may occur on a number of different length scales, *i.e.* over the whole beam resulting in whole beam self focussing effects, or, on a much smaller scale resulting in small scale self-focussing effects depending on the scale of the variation in radial intensity. What is required is an optical device for bandwidth generation via self-phase modulation in the absence of unwanted nonlinear effects such as self-focussing.

The single mode optical fiber is a cylinder of doped silica of linear refractive index  $n_{in}$  surrounded by a quartz cladding of linear refractive index  $n_{out}$ . By total internal reflection, the inner core of the fiber acts as a waveguide with no radial variation in optical intensity. An intense modelocked pulse launched into the fiber core is spectrally broadened by self-phase modulation without self focussing or spatial distortion. As the single mode fiber cores are quite small, typically 3 - 10  $\mu m$ , small peak input powers result in the large power densities required for effective pulse broadening. The emerging pulse may then be compressed to the transform limit using the pulse compression techniques described above [12-18].

To generate a probe pulse shorter than the 55-70 fs emerging from the multipass amplifier described above, an optical fiber based pulse compressor was



fabricated in this laboratory. The length of fiber must be sufficient to provide the optical path required to generate the desired bandwidth, yet no so long as to impress unwanted group velocity dispersion. This optimum length is dependent upon the input peak power, the fiber core diameter, the nonlinear refractive index  $n_2$  of the fiber core, and the dispersion properties of the fiber core material [24-26]. The calculated optimum length of 1.6 cm of optical fiber Newport SVP10 was in good agreement with the experimentally obtained value of 1 cm.

As the maximum peak power density of the fiber is  $\sim 5 \text{ GW} / \text{cm}^2$ , only a small fraction of the ACPM intensity may be focussed into the core. Two achromatic 10X microscope objectives (Melles Griot) were employed to launch and subsequently collimate the beam. Careful numerical aperture matching between the beam focussing and optical fiber (  $\text{NA} = .1$  ) resulted in a power throughput of  $> .5$ . This performance figure meets or exceeds contemporary literature values [25,27]. Throughput losses resulted largely from reflective losses at the fiber faces and non-diffraction limited ACPM focussing. Both polarization preserving and non-polarization preserving fibers were examined. As the weak birefringence of the silica core was not sufficient to rotate the input polarization during the 1 cm propagation length, the larger core non-polarization preserving fibers were used.

Operating near the damage threshold of  $\sim 5 \text{ GW} / \text{cm}^2$ , spectral broadenings of a factor of  $> 10$  were attained from the ACPM input spectral width of 10 nm to  $\sim 100$  nm centered around 620 nm (Figure III.5). The pulse emerging from the fiber

typically had a temporal width of 2 - 3 ps. Although full compression of this bandwidth would result in pulses  $\sim 5 - 7$  fs., the shortest autocorrelations were that of an optical pulse  $\sim 11$  fs. corresponding to a compression factor of  $> 20$ . However, pulses widths on the order of  $\sim 13$  fs were the more common experimental result.

The inability to compress the spectrally broadened pulse with one optical compressor indicates a nonlinear frequency chirp, or higher order dispersion occurring during the bandwidth generating process [24-28]. Multiple order dispersion requires multiple compressors to restore the pulse to the transform limit. As the reflective losses of these compressors can be  $> .5$ , making the pulses troublesome for spectroscopy, further compression was not pursued.

#### Experimental Configurations for Time Resolved Polarization Spectroscopy

The time resolved spectroscopic data presented here were obtained by measuring the change in optical density of a sample induced by the pump laser pulse as a function of delay time between the pump and the probe light pulses. The pumping and probing beams comprise the two optical arms of the experiment. One arm is reflected by a mirror fixed to a programmable stepper motor (Klinger UT100 150pp) providing the variable delay between the pulses. Immediately prior to the sample lens the pump beam passes through a horizontal polarizer while the probe beam passes through a polarizer oriented  $45^\circ$  to the horizontal (Figure III.6). The probe polarization

thus has projections both parallel and perpendicular to the pump polarization. These polarizers ensure strong polarization of the optical arms at the sample. The sample focussing lens is mounted with putty to eliminate the stress induced birefringence observed in many optical components.

The pump and probe beams, crossing at an angle of  $\sim 3^\circ$ , are typically focussed to a 50 - 100  $\mu\text{m}$  spot with a 10 cm lens. The use of separate focussing lenses for pump and probe beams of different wavelength to match spot sizes showed no improvement in signal to noise ratio. The confocal length of the beam waist under these conditions was a few millimeters. The sample was contained in a static or flowing cell depending on the quantity of material available. Cell optical paths were 1 mm to minimize loss of time resolution resulting from dispersion within the sample.

Care must be taken when performing optical experiments with short pulses, for the high peak powers may give rise to spurious signals. Thermal blooming, continuum generation, multiphoton absorption, thermal lensing and a variety of other nonlinear optical interactions may obscure the signal of interest, particularly when the pump and probe are temporally coincidental in the sample. To eliminate such contributions to the data, the pump and probe beams were attenuated to diminish the signal to the limit of detectability. The optical intensities may then be increased to reduce data acquisition time only if the signal retains its low intensity form.

Following the sample, a diaphragm blocks the pump beam while the probe beam is gently focused by a lens. A polarizing beamsplitter separates the parallel and

perpendicular probe components. The transmitted parallel and perpendicular beams are then directed to separate detectors. The photocurrents are sent to matched lock-in amplifiers (Ithaco 3985A) operating at the pump modulation frequency of *ca* 300 Hz. The two signal channels are then digitized and stored in a computer.

The experimental design outlined above allows simultaneous measurement of the two quantities required for the calculation of the anisotropy, here denoted  $S_{\parallel}(t)$  and  $S_{\perp}(t)$ . The anisotropy  $r(t)$  is given by:

$$r_{obs}(t) = \frac{S_{\parallel}(t) - S_{\perp}(t)}{S_{\parallel}(t) + 2S_{\perp}(t)} \quad (7)$$

The simultaneous acquisition of  $S_{\parallel}(t)$  and  $S_{\perp}(t)$  removes the systematic error which can arise from different degrees of excitation during consecutive measurements. The required balancing of the parallel and perpendicular probe intensities is achieved by neutral density filters. A solution standard with a known anisotropic response, for example the anisotropy of 0.4 over the first ten picoseconds for the nondegenerate transition of Nile blue in ethanol at 620 nm, serves as calibration. This practice allows an estimate of the error in recorded anisotropies of  $< 15\%$ .

The measurement of anisotropy offers a substantial improvement in signal to noise over conventional pump-probe experiments with little additional effort. Fluctuations in pump and/or probe powers impress significant noise components on time resolved experiments. However, the two-channel detection used for the anisotropy

experiment allows cancellation of these correlated fluctuations.

### CHAPTER III

#### References:

- 1 R.L.Fork, B.I.Green, and C.V.Shank,  
*Applied Physics Letters*, **38**, (9), (1981), 671
- 2 J.A.Valdmanis and R.L.Fork,  
*IEEE Journal of Quantum Electronics*, Vol. **QE-22** No.1, (1986), 112
- 3 J.A.Valdmanis, R.L.Fork, J.P.Gordon, *Optics Letters*, **10**, (3), (1985), 131
- 4 O.E.Martinez, R.L.Fork, and J.P.Gordon, *Optics Letters*, **9**, (5), (1984), 156
- 5 R.L.Fork, *Optics Letters*, **11** (10), (1986), 629
- 6 S.DeSilvestri, P.Laporta, and O.Svelto,  
*Ultrafast IV*, (Springer-Verlag, Berlin, Heidelberg, New York, 1984), p.23
- 7 J.C.Diels, I.C.McMichael, F.Simoni, R.Torti, and H.Vanherzeele,  
*Ultrafast IV*, (Springer-Verlag, Berlin, Heidelberg, New York, 1984), p.31
- 8 J.J.Fontaine, W.Dietal, and J.C.Diels,  
*IEEE Journal of Quantum Electronics*, Vol. **QE-19** No.10, (1983), 1467
- 9 R.S.Miranda, G.R.Jacobovitz, C.H.Brito Cruz, and M.A.F.Scarparo,  
*Optics Letters*, **11**, (4), (1986), 224
- 10 W.H.Knox, M.C.Downer, R.L.Fork, and C.V.Shank,  
*Optics Letters*, **9**, (1994), 552

- 11 W.H.Knox, *IEEE Journal of Quantum Electronics*, **24**, (1988), 388
- 12 R.L.Fork, O.E.Martinez, and J.P.Gordon, *Optics Letters*, **9**, (5), 91984), 150
- 13 R.L.Fork, C.H.Brito Cruz, P.C.Becker, and C.V.Shank,  
*Optics Letters*, **12**, (7), (1987), 483
- 14 O.E.Martinez, J.P.Gordon, and R.L.Fork,  
*J. Opt. Soc. A*, **1**, (10), (1984), 1003
- 15 J.D.Kafka and T.Baer, *Optics Letters*, **12**, (6), (1987), 410
- 16 E.B.Treacy, *Phys. Lett.*, **28A**, (1968), 43
- 17 D.Nickel, D.Kuhkle, and D. von der Linde,  
*Optics Letters*, **14**, (1), (1989), 36
- 18 A.A.Hnilo and O.E.Martinez,  
*IEEE Journal of Quantum Electronics*, Vol. **QE-23**, (5), (1987), 593
- 19 A.A.Hnilo and O.E.Martinez, and E.J.Quel,  
*IEEE Journal of Quantum Electronics*, Vol. **QE-22**, (1), (1986), 20
- 20 A.Migus, C.V.Shank, and E.P.Ippen,  
*IEEE Journal of Quantum Electronics*, Vol. **QE-18**, (1), (1982), 101
- 21 U.Ganiel, A.Hardy, G.Neumann, and D.Treves,  
*IEEE Journal of Quantum Electronics*, Vol. **QE-11**, (11), (1975), 881
- 22 A.A.Hnilo and O.E.Martinez, *Optics Communications*, **60**, (1,2), (1986), 87
- 23 G.Haag, M.Munz, and G.Marowsky,  
*IEEE Journal of Quantum Electronics*, Vol. **QE-19**, (6), (1983), 1149

- 24 M.A.Duauay and J.W.Hansen, *Appl. Phys. Lett.*, **14**, (1969), 14
- 25 B.Nikolaus and D.Grischowsky, *Appl. Phys. Lett.*, **42**, (1983), 1
- 26 A.M.Johnson, R.H.Stolen, and W.M.Simpson,  
*Appl. Phys. Lett.*, **44**, (1984), 729
- 27 J.D.Kafka, B.H.Kolner, T.Baer, and D.M.Bloom, *Optics Letters*, **9**, (1984), 505
- 28 J.D.Kafka and T.Baer, *Proc. SPIE*, **533**, (1985), 38



**Figure III.1** Diagram of colliding pulse mode locked (CPM) oscillator. Triangles are SF10 prisms used in pulse compression. Solid rectangles are reflectors. Solid line traces CPM beam. See text for details.

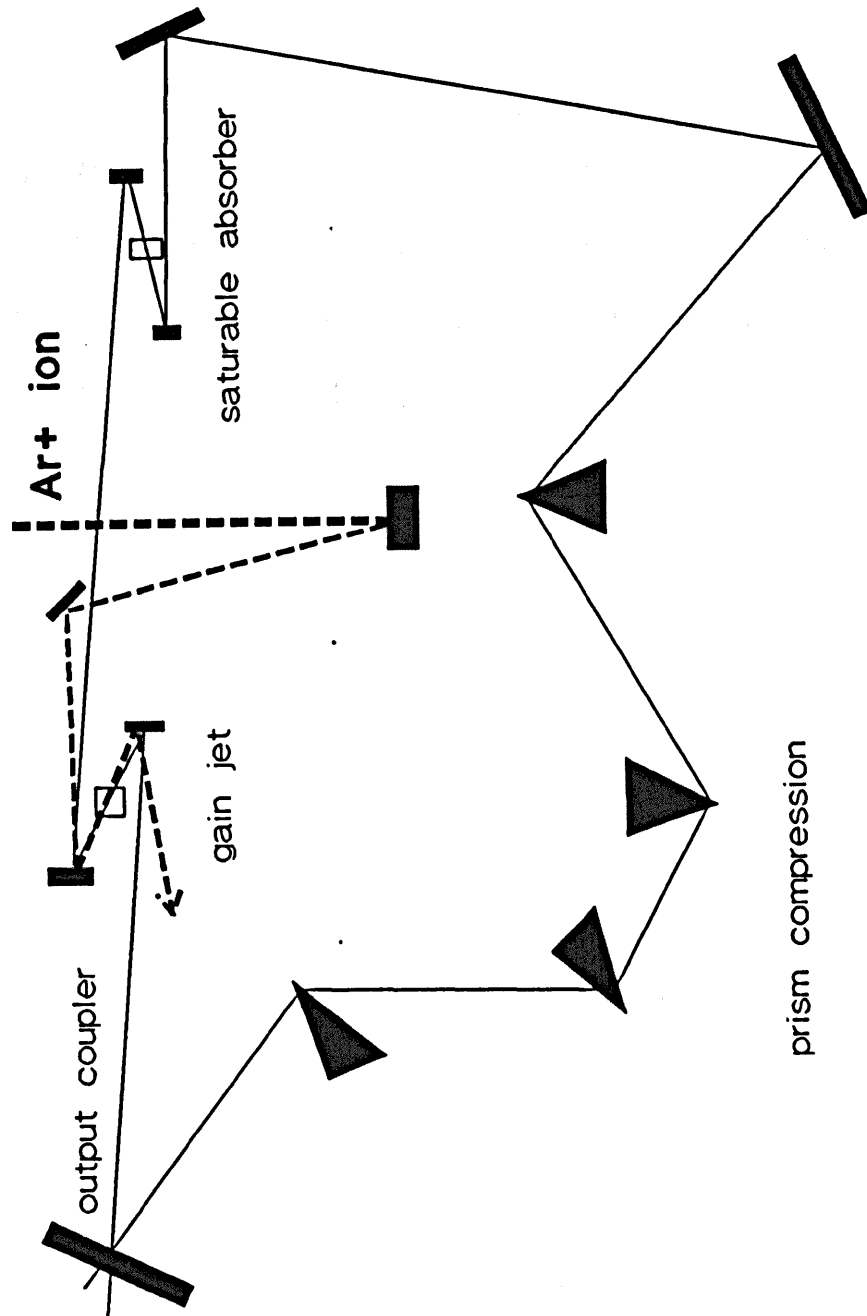
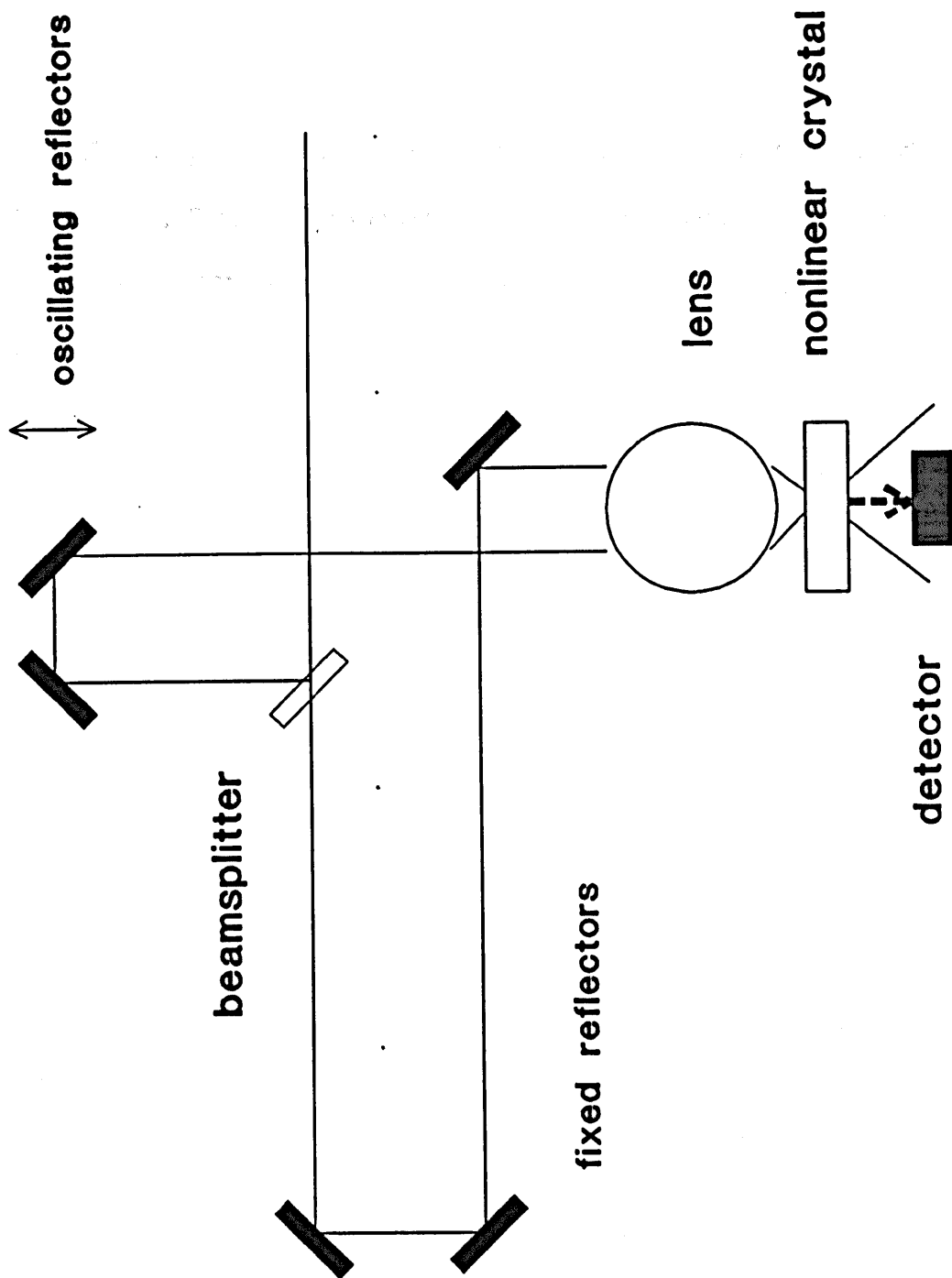
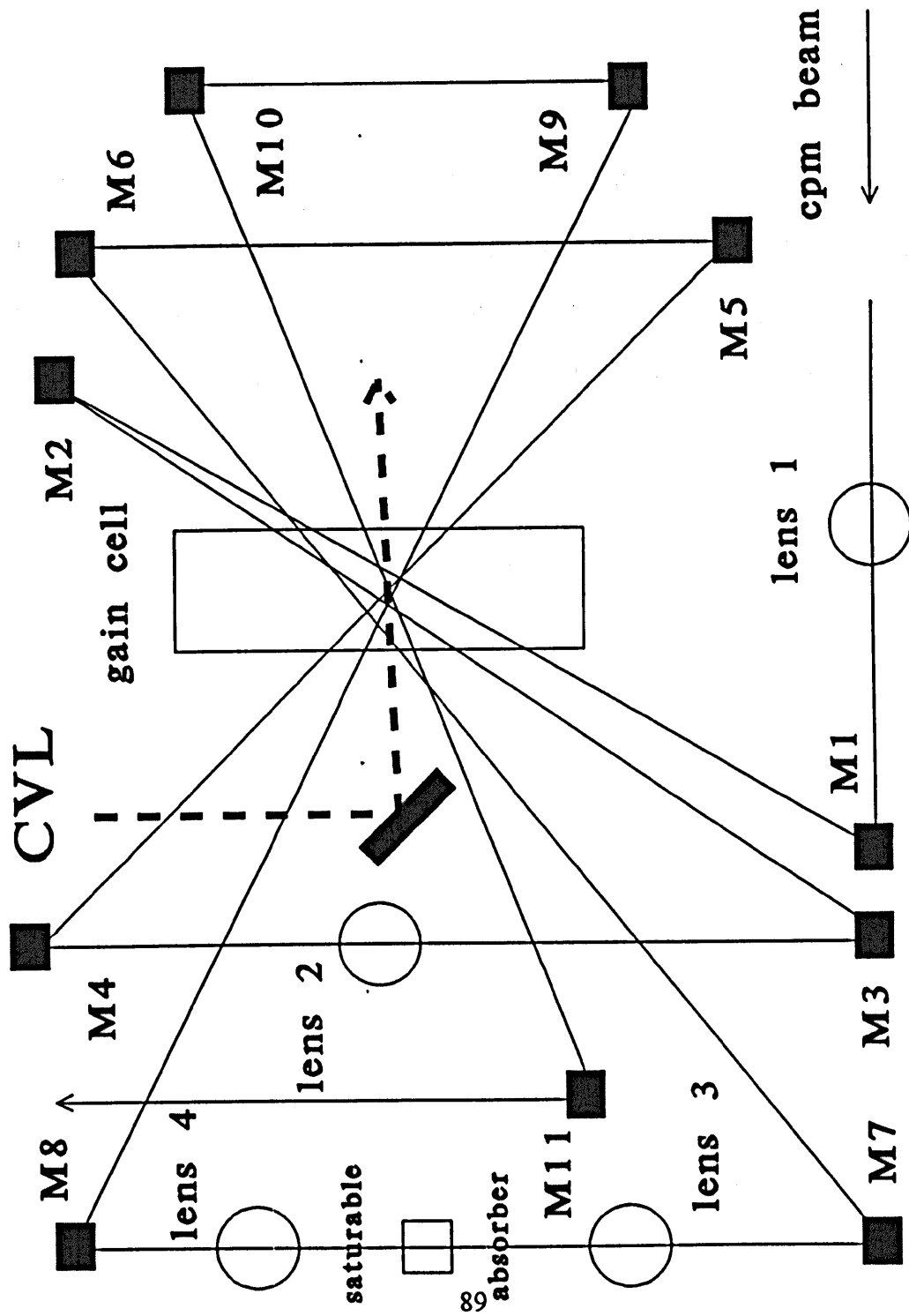


Figure III.2 Diagram of real time optical pulse autocorrelator constructed for pulse analysis. Solid black rectangles are reflectors. The sine wave oscillation of the reflectors indicated in the figure provides the time base, while the detector provides the signal amplitude for an xyz oscilloscope.



**Figure III.3** Diagram of the multipass amplifier described in text. Solid rectangles labeled  $M^*$  are reflectors. Open circles are lenses. Heavy dotted line traces path of copper vapor laser (CVL) beam. Thin solid line traces amplified CPM beam. See text for further details.



**Figure III.4** Diagram of the femtosecond spectrometer described in text. Open circles are lenses. Solid rectangles labeled M\* are reflectors. Solid triangles are prisms employed in pulse compression. Ethylene glycol cell used in continuum generation. Interference filter used to select probe wavelength. See text for further details.

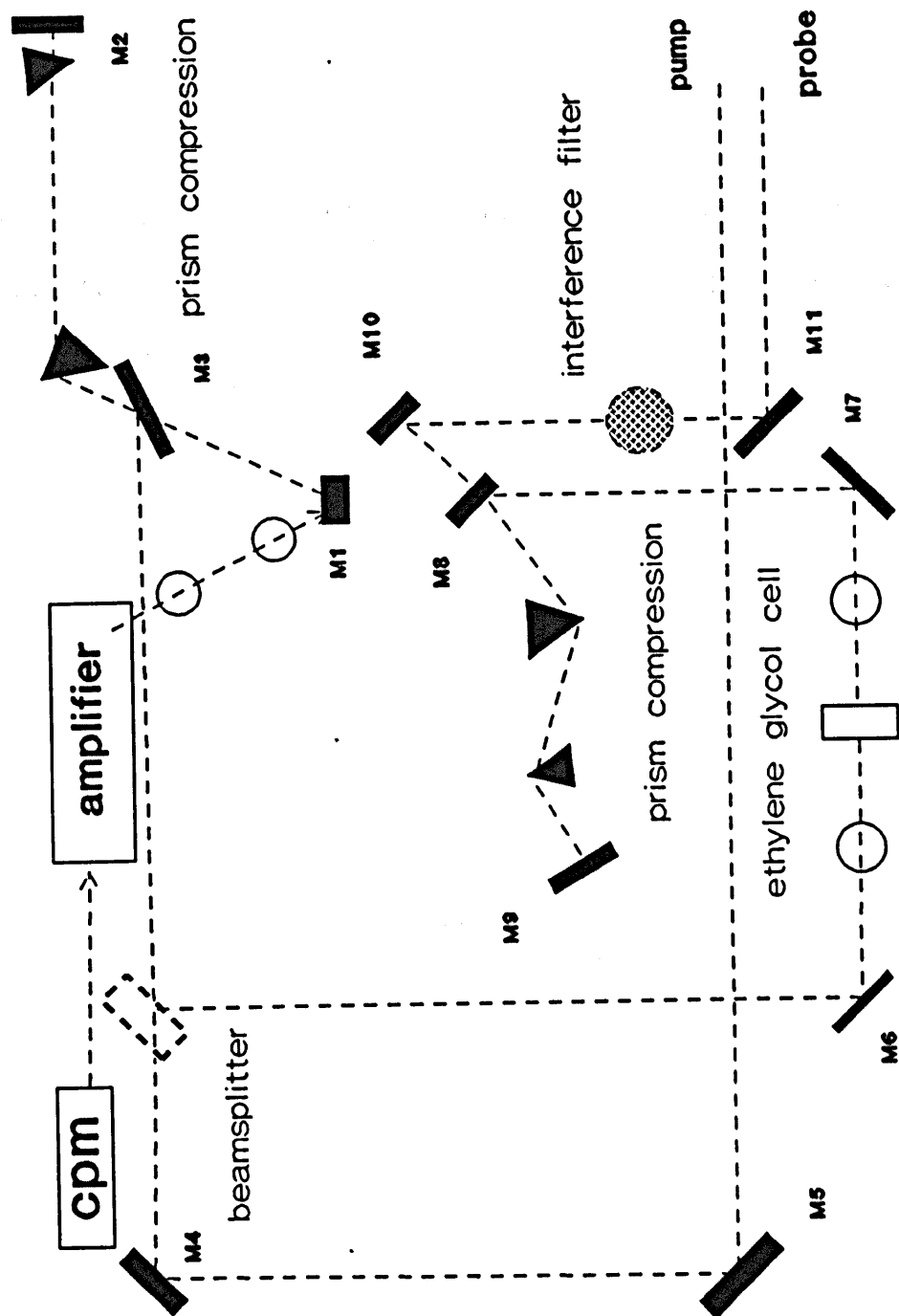




**Figure III.5** Typical experimental spectrum of continuum generated in optical fiber. This spectral data collected using Princeton Research OMA-II. Spectral width of input pulse  $\sim 10$  nm. See text for details.

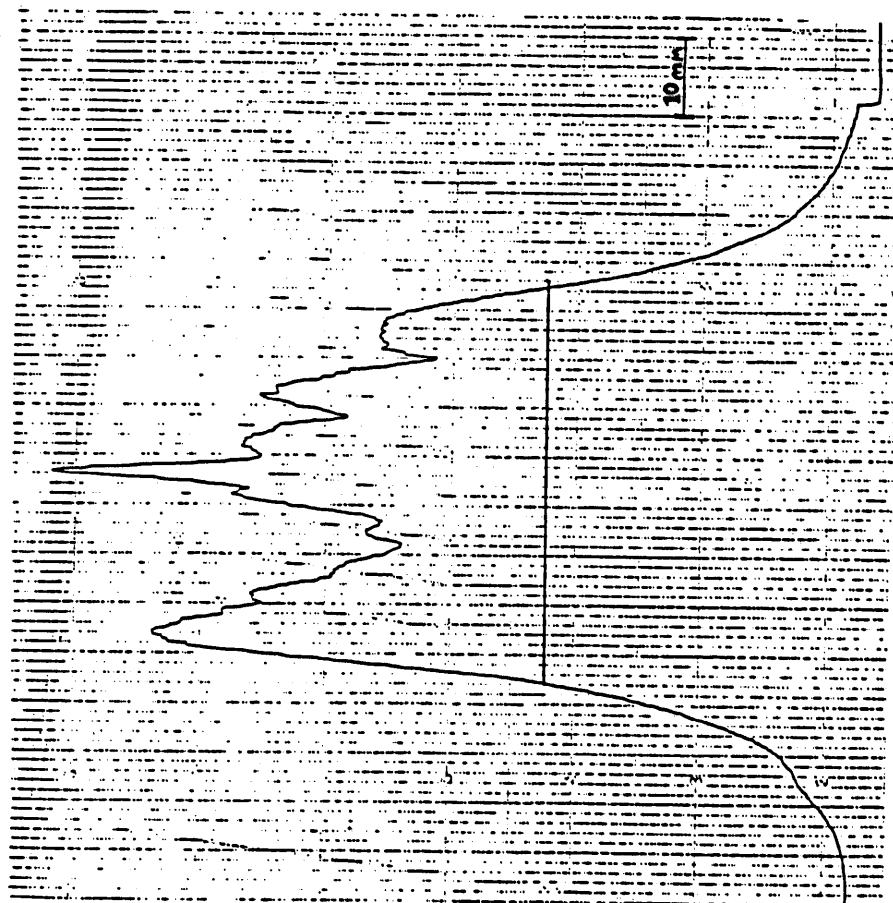
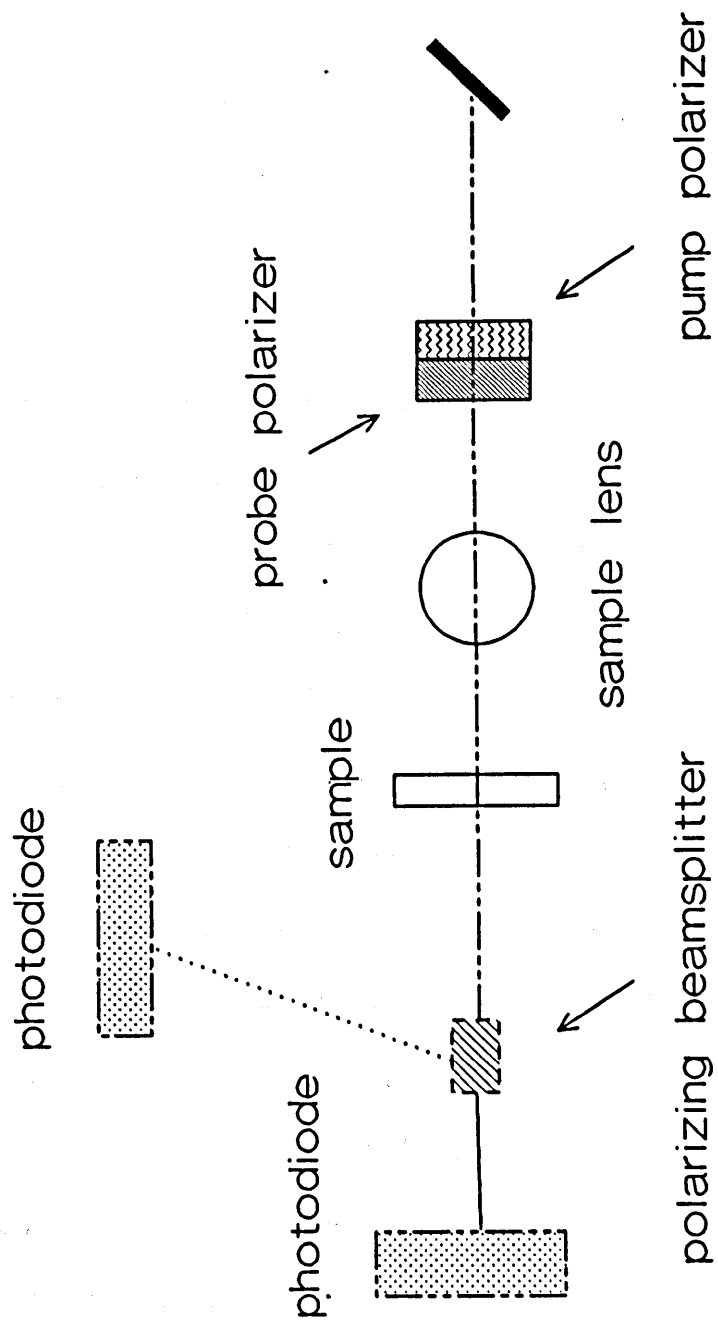


Figure III.6 Diagram of detection elements for simultaneous measurement of probe polarization component parallel and probe polarization component perpendicular to pump polarization. Probe polarizer and pump polarizer are displaced orthogonal to figure with optical axes at  $45^\circ$ . Polarizing beamsplitter separates parallel (solid line) and perpendicular (dotted line) probe polarization components. See text for details.



## Chapter IV

### Electron Transfer in the Molecular Complex

#### Tetracyanoethylene - Hexamethylbenzene

##### Introduction:

A key feature of all reactions that requires investigation is the nature of the energy distribution of product states. In descriptions of electron transfer reactions it is customary to subdivide this distribution into solvent related and internal mode excitations, with the former being treated as a classical polarization coordinate [1] and the latter by relaxation theories involving quantum modes of vibration [2]. Thus the so called reorganization energy associated with electron transfer is seen to have two dominant components, the solvent and internal mode contributions. In cases where the charge separated state is created directly by a light pulse and the electron transfer involves a return to the initial, neutral state, the modes that are involved in coupling the two states are those that constitute the spectra connecting them, such as absorption, fluorescence or Raman scattering. Therefore, in these cases, studies of electron transfer kinetics can be supplemented by knowledge of the reaction coordinate obtained through independent experiments.

In addition to the identification and quantification of the modes which

constitute the reaction coordinate by accepting the free energy of reaction, it is also of interest to identify the nature of the transfer coupling element which serves to couple the reactant and product electronic surfaces. In the electron transfer reaction discussed above, the charge separated state is created directly by a light pulse and the electron transfer involves a return to the initial, covalent state. This charge recombination reaction (CR) thus proceeds from the reactant, charge separated state to the product, neutral state. For molecular systems with high quantum yields this charge recombination reaction proceeds primarily by fluorescence which is driven by the radiative electronic transition dipole [3]. The positions and shapes of these luminescence bands accompanying the charge recombination reflects the evolution of the system along the reaction coordinate. Consider a luminescent charge recombination reaction occurring in the absence of appreciable internal mode reorganization. The difference between the peak of the absorption spectrum and the steady-state emission spectrum then indicates the amount of energy accepted by the solvent modes. The kinetics of this Stokes shift may be measured by collecting the emission as a function of time following excitation. The time scale associated with this shift is indicative of the solvent reorientation time in response to the creation of the charge separated state.

The emission from the charge separated state may be quenched in the presence of dominating relaxation pathways. Such radiationless transitions between the reactant and product surface will occur if the optically prepared charge separated state evolves

to a "critical" particle configuration of electronic degeneracy on a time scale that is rapid with respect to the radiative relaxation processes. These "crossing points" where the zero - order Born-Oppenheimer reactant and product electronic surfaces intersect are the phase regions in which radiationless jumps are most likely to occur, since the reacting complex in this region has a probability of being controlled by either surface. These regions are the funnels or holes of the reaction surface [4].

The coupling matrix elements which split the zero-order reactant - product electronic degeneracy were discussed in Chapter II of this thesis. These off-diagonal terms, the electronic coupling matrix element which expresses the Coulombic repulsion at the avoided crossing, exchange interactions, and the nuclear coupling matrix elements which express the non-adiabaticity of the reaction, couple the reactant and product vibronic wavefunctions. The examination of these radiationless electronic transitions mechanisms governing electron transfer reaction dynamics is central to the study of these reactions.

Another aspect of the electron transfer reaction in the condensed phase which has recently come to the forefront of contemporary chemical physics research is the examination of the picosecond and subpicosecond dynamics of the solvent degrees of freedom. The advent of ultrafast lasers has enabled the study of these rapid solvations as the solvent responds to the nonequilibrium polarization state created by a photoinitiated electron transfer. The time resolution of these spectrometers has made it possible to study the reaction dynamics of electron transfer reactions which occur

on a time scale which is comparable to the solvent relaxation times. The reaction is occurring along nonequilibrated modes of the reaction coordinate. Since the efficiency of a photoinduced electron transfer process, that is, the number of charge separated states created per photon absorbed, depends upon the rapidity of the system's evolution to the ionic state, the elucidation of the early time dynamics is central to the goal of emulating the efficiency and specificity of the charge transfer events observed in natural photosynthetic systems.

These reaction features, the nature of the energy distribution in the product states, the matrix elements coupling the reactant and product electronic surfaces, and the reaction of molecular systems in nonequilibrated configurations, provide the basis for the spectroscopic examination of the ultrafast electron transfer reactions detailed below.

#### Donor-Acceptor System:

Tetracyanoethylene (TCNE) is a white crystal at room temperature and atmospheric pressures which dissolves to yield a colorless, clear solution, as does the crystalline hexamethylbenzene (HMB). Mixing these solutions produces a red to violet solution the shade and intensity of which depends upon the concentration of the solutes. This absorption in the visible region is a result of the TCNE-HMB molecular complex formation.



The TCNE-HMB complex is a member of a group of complexes whose theoretical description is owed to the pioneering work on electron-transfer (ET) by Mulliken and others [3]. It is well established that the ground state of such a complex is weakly bound and only slightly polar whereas the electronically excited state that absorbs in the visible region involves the transfer of an electron from HMB to TCNE. Mulliken described the ground state bond as arising from the admixture of the pure ionic state  $| I >$  character into the neutral, Van der Waals state  $| N >$ . The ground state  $| G >$  and the excited state  $| E >$  are written:

$$\begin{aligned} | E > &= \alpha(\vec{x}) | N > - \beta(\vec{x}) | I > , \\ | G > &= \beta(\vec{x}) | N > + \alpha(\vec{x}) | I > , \end{aligned} \tag{1}$$

Here the mixing coefficients  $\alpha(x)$  and  $\beta(x)$  are written as explicit functions of the nuclear coordinates ( $x$ ). The ground state dipole moment  $\mu_0$  in the molecular complex TCNE-HMB is 2 Debye [5]. This quantity may be compared to  $\mu_{\text{ION}} = 16$  Debye which is calculated by placing an electron on TCNE at the experimentally observed separation of 3.35 Angstroms measured by X-ray diffraction studies of the crystalline compound [6,7]. The ground state is but weakly polar with respect to the ionic state. This comparison indicates the magnitude of the  $| N >$  and  $| I >$  components of the states  $| G >$  and  $| E >$ .

Approximate potential energy surfaces are shown in Figure IV.3 along the

HMB donor (D) and TCNE acceptor (A) stretch. The figure is generated using Morse potentials with the ground state minimum  $r_0 = 3.35$  Angstrom, measured using X-ray diffraction [6,7], the excited state minima  $r_A = 3.14$  Angstrom measured by resonance Raman [8], ground state well depth of  $3000 \text{ cm}^{-1}$  [9,10], and excited state well depth of  $41 \cdot 10^3 \text{ cm}^{-1}$  calculated using the ionization potential ( $\text{IP} = 64.1 \cdot 10^3 \text{ cm}^{-1}$ ) of the donor [3a], the electron affinity ( $\text{EA} = 12.9 \cdot 10^3 \text{ cm}^{-1}$ ) of the acceptor [3a], and the driving force of  $\Delta G^0 = -13 \cdot 10^3 \text{ cm}^{-1}$  [8]. The curvature of the ground state well is fixed by the DA stretch of  $165 \text{ cm}^{-1}$ . The curvature of the excited state well is set to ensure Frank-Condon absorption at 550 nm.

#### Charge Recombination Measurements:

The dynamics of the condensed phase charge recombination reaction of the molecular complex TCNE-HMB were examined using the femtosecond laser described in Chapter II of this thesis. The excitation pulse centered at 620 nm and of 50 - 70 femtosecond temporal width placed the molecular complex on the excited electronic surface  $|E\rangle$  which is largely ionic in character. This photoexcitation transfers an electron from the donor HMB to the acceptor TCNE creating the charge separated state  $\text{TCNE}^- \text{HMB}^+$ . This charge separated state undergoes radiationless relaxation via charge recombination to return to the initial  $|G\rangle$  electronic state. The charge recombination kinetics are measured using pump - probe spectroscopy: the system

prepared with the 620 nm pump pulse may be interrogated with a 40-70 femtosecond probe pulse of  $\sim 15$  nm width centered between 450 and 700 nm.

#### Nonpolar Solvents:

The 620 nm excitation pulse results in a bleaching of the ground state absorption of TCNE-HMB in the nonpolar solvents examined, which may be observed at probe wavelengths between 500 and 680 nm. Figure IV.4 presents a typical experimental result. The transient bleach rises with the pump pulse and recovers with a single exponential decay. When probed at 620 nm, this recovery time constant is  $16.6 \pm 0.2$  ps in cyclohexane,  $11.2 \pm 0.1$  ps in  $\text{CCL}_4$ , and  $9 \pm 0.4$  ps in  $\text{CS}_2$ . The variation in recombination kinetics with respect to solvent is probably due to differences in the free energy of reaction,  $\Delta G^0$ , and polarizabilities of the different solvents.

Superimposed on the decay kinetics in cyclohexane is an oscillation of frequency  $\hbar\omega = 161.7 \pm 0.5 \text{ cm}^{-1}$  which oscillates in the bleach signal like  $\cos(\omega t + \phi)$  with phase shift  $\phi = -0.20 \pm 0.11$  rad and decays with a time constant of  $\tau = 1.4 \pm 0.2$  ps. The same oscillation is seen when the bleach recovery is observed at 650 nm ( $\hbar\omega = 158 \pm 1.3 \text{ cm}^{-1}$ ,  $\phi = 0 \pm 0.2$  rad,  $\tau = 1.2 \pm 0.3$  ps). This oscillatory component of the transient bleach signal is due to preparation of a nuclear coherence in the donor-

acceptor stretch of the ground electronic state by impulsive stimulated Raman scattering [11,12].

As stated above, the bleaching and recovery of the ground state absorption of TCNE-HMB is observed at probe wavelengths outside the excitation spectral width. For example in  $\text{CCl}_4$ , the bleach recovery times are 11.2 ps at 620 nm,  $18.0 \pm 0.3$  ps at 540 nm and  $7.0 \pm 0.3$  ps at 650 nm. When the prepared state is probed below 500 nm, however, the signal is dominated by the transient absorption of the  $\text{TCNE}^-$  ion. This absorption feature peaks at  $\sim 450$  nm [13]. When probed at 450 nm in  $\text{CCl}_4$ , the transient absorption signal from the  $\text{TCNE}^-$  ion was measured to rise exponentially with a time constant of  $470 \pm 30$  fs. The observation of the  $\text{TCNE}^-$  ion proves the ionic nature of the  $|E\rangle$  state.

#### Polar Solvents:

In order to examine the role of polar solvent dynamics in the TCNE-HMB charge recombination reaction, the photoinduced charge transfer kinetics were examined in eleven polar solvents. In order to ensure breadth in the experimental solvation times, solvents with dielectric relaxation times  $\tau_L$  (see Chapter II of this thesis) ranging from .56 ps for acetonitrile [14] to 125 ps for glyceroltriacetate [15] were employed. For these solvents the theoretical solvent reorganization energies calculated with the assumption of spherical molecules ranges from  $460 \text{ cm}^{-1}$  for

trichloroethene to  $1470\text{ cm}^{-1}$  for acetonitrile (see Table IV.2).

The transient bleach induced in the TCNE-HMB complex by the 620 nm excitation recovers on a time scale of .3 - 2 ps which is quite rapid with respect to the  $\sim 10 - 16$  ps recovery observed in the nonpolar solvents. Oscillations due to nuclear coherence in the  $165\text{ cm}^{-1}$  donor-acceptor stretch are again observed.

Most importantly, this bleach recovery for the molecular complex in the polar solvents decays into a transient absorption which recovers on approximately the same time scale as the bleach component. Figure IV.7 shows a typical experimental result for the transient spectra in a polar solvent. This transient absorption is attributed to the formation of vibrationally hot molecules in the ground electronic state  $|G\rangle$  [15-18]. That is, the driving force of the reaction has been accepted by the nuclear degrees of freedom comprising the reaction coordinate resulting in vibrationally excited species on the ground electronic surface which undergo subsequent relaxation.

Since the excitation pulse is much shorter than the polarization relaxation, the rapid charge redistribution initiated by the photoexcitation takes place over a "frozen" solvent configuration, which undergoes subsequent relaxation as the system evolves to the charge recombination configuration. The charge of the system is again redistributed as the complex returns to the electronic ground state, which is essentially covalent. Immediately following the charge recombination, the solvent is in a nonequilibrium configuration. Since the transient absorption component is observed in the polar media and not the nonpolar media, it seems reasonable that the excited modes responsible for

the absorption and subsequent recovery are those associated with the solvent.

The data are fit to a three level model:  $|a\rangle$ , the initial, Boltzmann ground state ensemble,  $|b\rangle$ , the electronically excited complex created by the excitation pulse, and  $|c\rangle$ , the vibrationally hot species in the ground electronic state. The decay parameter  $k_{bc}$  describes the relaxation from state  $|b\rangle$  to state  $|c\rangle$ , while the decay parameter  $k_{ca}$  describes the relaxation from state  $|c\rangle$  to state  $|a\rangle$ . The absorption component of the experimental data results from the molecules  $|c\rangle$  and is proportional to this population:

$$I_{C, Abs.} = I(t) \otimes \frac{k_{bc}}{k_{ca} - k_{bc}} (e^{-k_{bc} t} - e^{-k_{ca} t}), \quad (2)$$

The bleach component of the signal is proportional to the dynamics of the population in state  $|a\rangle$  and is given by:

$$I_{A, Bleach} = I(t) \otimes \frac{k_{bc} k_{ca}}{k_{ca} - k_{bc}} \left( \frac{e^{-k_{bc} t}}{k_{bc}} - \frac{e^{-k_{ca} t}}{k_{ca}} \right), \quad (3)$$

where  $I(t) \otimes \dots$  stands for convolution with the system response function. Neither transient absorption nor stimulated emission signal components were observed at probe wavelengths in the vicinity of the excitation wavelength. As noted above, absorption from state  $|b\rangle$  is observed at probe wavelengths in the region  $\sim 450$  nm.

The transient data were fit with the absorption and bleach functions expressed in equations IV.2 and IV.3. During the fitting procedure, for all solvents, the model time constants,  $k_{bc}$  and  $k_{ca}$ , tended to nearly identical fit values. Therefore the final fitting was performed by constraining the parameters  $k_{bc}$  and  $k_{ca}$  to be equal. Physically, this corresponds to solvation of the photoprepared state leading to charge recombination, followed by solvation of the ground electronic state. As seen in Figure IV.6 and subsequent figures, this model results in excellent fits to the experimental data. This time constant is identified as the charge recombination time and plotted in Figure IV.16 versus the solvent dielectric relaxation time  $\tau_L$  as measured by dynamic Stokes shift experiments [15]. It is apparent from this figure that the electron transfer rate for the complex TCNE-HMB in solvents of  $\tau_L \geq 1.7$  ps exceeds the Stokes solvation time. Roughly, in fast solvents, the charge recombination occurs with the dielectric relaxation. In the slower solvents, ( $\tau_L \geq 1.7$  ps) the charge recombination occurs over a "frozen" solvent configuration.

The electron transfer reaction has also been interrogated with probe wavelengths other than the excitation wavelength. Figure IV.14 shows a typical result; the solvent for this data is acetonitrile. The relative magnitude of the absorptive component with respect to the bleaching component increases when probed to the red of the excitation wavelength. There is quite good agreement amongst the time constants resulting from the model detailed above for probe wavelengths equal to, or to the red of, the excitation wavelength.

### Electron Transfer Rates:

The theory of electron transfer reaction rates developed by Marcus [1,19], Jortner [2,20], and others [21-25], discussed in Chapter II of this thesis, expresses the charge transfer reaction as an internal conversion process. The driving force of the reaction, *i.e.* the electronic free energy  $\Delta G^0$ , is converted into the energy of the accepting modes of the reaction. As discussed in Chapter II of this thesis these modes may be high frequency vibrations of the donor-acceptor complex, best described as quantized degrees of freedom, or low frequency motions which behave classically. Typically, the latter are comprised primarily of solvent motions, though low frequency modes of the donor- acceptor complex such as torsional motions may contribute. The general form of this electron transfer rate expression is given as [20,21]:

$$k = A \sum_{i,f} P_i F_{i,f} \exp\left\{-\frac{(\Delta G^0 + \lambda_s + E_{f,i})^2}{4 \lambda_s k_B T}\right\}, \quad (4)$$

where A is a frequency factor,  $\Delta G^0$  is the driving force of the reaction discussed above,  $E_{f,i}$  is the energy difference and  $F_{i,f}$  is the Franck-Condon factor between the initial and final vibrational state of a quantized accepting mode.  $P_i$  is the probability of finding this mode in the initial state  $|i\rangle$ . In this equation  $\lambda_s$  is the reorganization energy of bath modes that are considered to behave in a classical fashion. The Boltzmann constant is  $k_B$  and the temperature is T.



Experimental data of electron transfer rate versus driving force are often compared to the rate expression above using a single quantized accepting mode with a frequency of  $\sim 1500 \text{ cm}^{-1}$  corresponding to the frequency of a typical aromatic stretch mode [see e.g. 26]. As discussed in Chapter II of this thesis, the relocalization of charge affects a large number of interior modes of the system with respect to a bond rupture- mass transfer reaction. The use of one  $1500 \text{ cm}^{-1}$  mode is an attempt, in the absence of other data, to express the high frequency components of the reaction coordinate in an average way.

As the charge transfer process is typically coupled to a number of interior modes the nonadiabatic rate constant incorporating the transmission through each vibronic pathway as detailed in Chapter II of this thesis may be employed. Recall the first order perturbation rate constant is given by:

$$k^{(1)} = \sum_{n,m} P_n k_{nm}^{(1)} \quad (5)$$

where the sum is over all the initial (n) and final (m) quantized vibrational states involved in the process and  $P_n$  denotes the initial distribution of the quantized modes.

The rate constant for each pathway is given by:

$$k_{nm}^{(1)} = \frac{2\pi |H_{RP}|^2}{\hbar \sqrt{4\pi\lambda_s k_B T}} \prod_v |\langle n_v | m_v \rangle|^2 \exp\left\{ \frac{-(\Delta G^0 + \lambda_s + (m_v - n_v) \hbar\omega_v)^2}{4 \lambda_s k_B T} \right\} \quad (6)$$

where the index  $\nu$  indicates the normal, quantized modes coupled to the electron transfer reaction, and  $\lambda_s$  is the reorganization energy of the classically treated modes.

It is in principle possible to numerically calculate the electron transfer rate by summing the rate expression above over the coupled interior modes. This calculation is facilitated, however, by employing a wave-packet formulation of the perturbation rate expression:

$$k^{(1)} = \frac{|V|^2}{\hbar^2} \int_{-\infty}^{\infty} \prod_i \langle 0_i | 0_i(t) \rangle \exp \left\{ -\lambda_s k_B T t^2 / \hbar^2 - i (\lambda_s + \Delta G^0) t / \hbar \right\} dt, \quad (7)$$

where  $|0(t)\rangle$  is the ground vibrational state of the reactant electronic state propagated over the product electronic state's potential. In this equation the factor  $\lambda_s k_B T / \hbar^2$  denotes the variance of the energy gap fluctuations due to solvent motions leading to electronic dephasing of the electron transfer transition and  $\lambda_s + \Delta G^0$  is the average energy gap. The vibrational correlation function of a harmonic oscillator for mode  $i$  is given by [27,28]:

$$\langle 0_i | 0_i(t) \rangle = \exp \{ s_i (\bar{n}_i + 1) [\exp(-i\omega_i t) - 1] + s_i \bar{n}_i [\exp(i\omega_i t) - 1] \}, \quad (8)$$

$$\bar{n}_i = [\exp(\hbar\omega_i / kT) - 1]^{-1}$$

where  $s \equiv \Delta^2/2$  where  $\Delta$  is the normal dimensionless shift defined in Chapter II.

The equilibrium shifts of the eleven interior modes comprising the

reaction coordinate of the electron transfer in the TCNE-HMB complex have been measured by Myers *et al.* [8] using resonance Raman excitation profiles and static absorption spectra as detailed in Chapter II of this thesis. The solute - solvent interaction responsible for the broadening of the charge transfer absorption and shape of the resonance Raman excitation profile was modeled in this analysis as a Brownian oscillator. The result of this analysis of TCNE-HMB in  $\text{CCl}_4$  is a driving force,  $\Delta G^0$ , of  $-11600 \text{ cm}^{-1}$  and solvent reorganization energy,  $\lambda_s$ , of  $3930 \text{ cm}^{-1}$ . The authors note, however, that this calculation for the solvent reorganization energy is too high for the nonpolar  $\text{CCl}_4$  while the value of the driving force must be correspondingly smaller. These values, the equilibrium shifts of the interior modes, as well as the reorganization energies calculated from these data are given in Table IV.1. The relative magnitude of the eleven interior modes shown to be coupled to the electron transfer process are used in the following section to fit the static absorption spectra in order to obtain more realistic estimates of the driving force,  $\Delta G^0$ , and the  $\text{CCl}_4$  solvent reorganization energy,  $\lambda_s$ .

#### Rate Parameters from Static Spectra:

##### Electronic Coupling

The evaluation of the electron transfer rate expression above requires the

matrix element  $H_{RP}$  which couples the reactant and product electronic surfaces of the TCNE-HMB complex. Hush has proposed the estimation of this quantity using the radiative coupling element  $\mu_{EG}$  responsible for the charge transfer absorption [24]. As expressed in equation IV.1, first order perturbation theory is used to write the ground state wave function  $|G\rangle$  and the electronically excited state  $|E\rangle$  as linear combinations of the neutral  $|N\rangle$  and ionic  $|I\rangle$  uncoupled states with the undressed expansion coefficient:

$$\frac{\langle G | H | E \rangle}{E_N^0 - E_I^0} \quad (9)$$

The denominator of the expansion coefficient is given by the peak of the absorption spectrum  $h\nu_{\max}$ , while the numerator is the electronic coupling matrix element. In the charge recovery dynamics examined in this thesis chapter, the reactant state is equated with  $|E\rangle$  and the product state with  $|G\rangle$ ;  $H_{GE} = H_{RP}$ . The states  $|G\rangle$  and  $|E\rangle$  given by the above approximation can be used to write an expression for  $\mu_{EG}$  as a function of the expansion coefficient and:

$$H_{RP} = \frac{\mu_{EG} h\nu_{\max}}{\mu_{ion}} \quad (10)$$

where  $\mu_{ion} \approx 16$  Debye as earlier detailed and  $\mu_{EG}$  is estimated from the absorption spectrum at 3.5 Debye resulting in  $H_{RP} = 4100 \text{ cm}^{-1}$ . The Hush coupling assumes  $H_{RP}$

is not a function of nuclear coordinates. Perturbation theory is applicable when  $H_{RP} \ll h\nu_{\max}$ .

### Driving force and Reorganization energy

As discussed above, the charge transfer absorption may be modelled to obtain the driving force of the electron transfer reaction. This calculation was performed to estimate the driving force and reorganization energies of the solvent accompanying the electron transfer in TCNE-HMB.

As detailed in Chapter II in the discussion regarding exterior modes of reactions in solution, the solvent reorganization energy may be conveniently calculated within the confines of the dielectric continuum model (see equation II.26). The result of this calculation for the nonpolar solvent  $\text{CCl}_4$  is  $100 \text{ cm}^{-1}$ . This dielectric continuum calculation was performed for the 12 solvents examined in this study; the results of the calculation are listed in Table IV.2.

Using this value for the reorganization energy, an excellent fit to the charge transfer absorption of TCNE-HMB in  $\text{CCl}_4$  which yielded a driving force  $\Delta G^0 = -13860 \text{ cm}^{-1}$  was obtained by increasing the equilibrium shifts reported by Myers *et al.* by 0.23. The spectra in the remaining solvents were then fit with  $\Delta G^0$  and  $\lambda_s$  as free parameters. The results of these fits as well as the theoretical values are given in Table IV.2. The good agreement between the fit values and theoretical values for  $\lambda_s$

indicate that there is little spectral contribution from undetected low frequency modes coupled to the charge transfer.

#### Non-Born-Oppenheimer Coupling:

A cursory evaluation of the Marcus rate expression using the Hush coupling equal to  $4100 \text{ cm}^{-1}$  calculated above, employing the 11 interior modes and the corresponding equilibrium shifts, and incorporating the reorganization energies and driving forces calculated from the absorption spectra yields a theoretical electron transfer rate in a given solvent which is orders of magnitude too rapid with respect to the experimentally observed value. Since there is close agreement between the dielectric continuum theoretical reorganization energies and those obtained via absorption spectra fitting (see Table IV.2), and good agreement amongst the solvent specific estimates of driving force from Myers *et al.* [8] and this work, attention naturally turns to the electronic coupling matrix element  $H_{RP}$ .

Recall here the expression of the charge transfer Mulliken states expressed as nuclear coordinate dependent functions:

$$\begin{aligned} | E \rangle &= \alpha(\vec{x}) | N \rangle - \beta(\vec{x}) | I \rangle , \\ | G \rangle &= \beta(\vec{x}) | N \rangle + \alpha(\vec{x}) | I \rangle , \end{aligned} \tag{1}$$

where  $\vec{x}$  is the set of vibrational coordinates coupled to the electron transfer. Assuming separable harmonic surfaces, the potential energy of these states may be written:

$$E_N(\vec{x}) = \sum_i \frac{\lambda_i x_i^2}{x_{i0}^2} \quad E_I(\vec{x}) = \sum_i \frac{\lambda_i (x_i - x_{i0})^2}{x_{i0}^2} + \Delta E \quad (12)$$

where  $\lambda_i$  is the reorganization energy given by  $(\mu_i \omega_i^2 x_{i0}^2) / 2$  where  $\mu_i$  is the reduced mass associated with the  $i^{\text{th}}$  vibration,  $\omega_i$  is the frequency of the mode, and  $x_{i0}$  is the equilibrium shift of the mode. The driving force is here given by  $\Delta E$  and the sum runs over the  $i$  interior modes coupled to the electron transfer reaction. Using the experimental values for the equilibrium shifts  $x_{i0}$  and a driving force of  $13000 \text{ cm}^{-1}$ , the lowest observed intersection of the  $|N\rangle$  and  $|I\rangle$  states is on the order of  $6 \cdot 10^4 \text{ cm}^{-1}$  above the  $|N\rangle$  minimum. The vibronic states which are Frank-Condon accessed by a  $16100 \text{ cm}^{-1}$  (620 nm) photon are essentially diabatic states of ionic character  $|I\rangle$ . As the Franck-Condon coupling between the photon accessed vibronic states and the nearly degenerate vibronic states which are high lying in the  $|N\rangle$  manifold is  $\sim 10^{-5}$ , the resultant dressed coupling is  $4000 \cdot \sqrt{10^{-5}} = 13 \text{ cm}^{-1}$ .

This dressed coupling may be used as the perturbation expansion parameter (cf. equation IV.9) to express the ground  $|G\rangle$  and excited  $|E\rangle$  vibronic states as admixtures of the neutral  $|N\rangle$  and ionic  $|I\rangle$  states:

where, for example, the product wavefunction  $|E\rangle = |v_E\rangle$  is essentially a vibronic

$$|E\rangle|v_E\rangle \approx |I\rangle|v_I\rangle - \frac{\langle 0_N|v_I\rangle V}{\Delta E_{v_I}}|N\rangle|0_N\rangle + \sum_{v_N}' c_{v_N} |N\rangle|v_N\rangle, \quad (13)$$

$$|G\rangle|0_G\rangle = |N\rangle|0_N\rangle + \sum_{v_I} \frac{\langle 0_N|v_I\rangle V}{\Delta E_{v_I}}|I\rangle|v_I\rangle, \quad (14)$$

state of the ionic manifold with character of the ground vibronic state proportional to the Hush coupling  $V$ , the Frank-Condon factor  $\langle 0_N | v_I \rangle$ , and inversely proportional to the energy difference between the states. The primed sum in equation IV.13 runs over the vibronic levels of the neutral state.

As detailed in Chapter II ( see equations II.17, II.22, II.23), the nuclear coupling terms which couple the Born-Oppenheimer electronic surfaces result from the nuclear kinetic energy operator. For the charge transfer complex TCNE-HMB the inclusion of the derivative of the electronic wavefunction with respect to the nuclear coordinate adds to the transmission element:

$$V_{NBO} = - \sum_i \frac{\hbar^2}{\mu_i} \langle \chi_G | \langle G | \frac{\partial}{\partial x_i} | E \rangle \frac{\partial}{\partial x_i} | \chi_E \rangle, \quad (15)$$

where the sum runs over all the vibrational modes of the molecule and  $\chi$  is a product vibrational wavefunction. Consider the mode  $i$  along coordinate  $x_i$  with vibrational wavefunction  $|n_E\rangle$  and  $n_E$  quanta in the mode. The nuclear coupling term for the mode  $i$  is:



$$V_{NBO}^i = \frac{-\frac{\hbar^2}{m_i} \langle n_G | \langle G | \frac{\partial}{\partial x_i} | E \rangle \frac{\partial}{\partial x_i} | n_E \rangle}{\langle n_G | n_E \rangle} \langle \chi_G | \chi_E \rangle . \quad (16)$$

An expression for the term  $V'_i = \langle G | \partial / \partial x_i | E \rangle$  is obtained using the Mulliken expression for the ground and excited states as coordinate dependent sums of the diabatic states  $| N \rangle$  and  $| I \rangle$  ( see equation IV.1). If the derivative of these diabatic states  $| N \rangle$  and  $| I \rangle$  is neglected, *i.e.* approximated as position independent quantities, the term  $V'_i$  is written as a function of  $\alpha(\vec{x})$ ,  $\beta(\vec{x})$ , and their derivatives. The secular equation which expresses the energies of  $| G \rangle$  and  $| I \rangle$  by coupling  $| N \rangle$  and  $| I \rangle$  with  $V$  is then used to obtain values for  $\alpha(\vec{x})$  and  $\beta(\vec{x})$  and :

$$V'_i(\vec{x}) = \frac{-\gamma_i / 2}{(x_i - x_{ic})^2 + \gamma_i^2} , \quad \gamma_i \equiv \sqrt{\frac{2V^2}{\lambda_i m_i \omega_i^2}} \frac{\Delta_i}{|\Delta_i|} , \quad (17)$$

where  $x_{ic}$  is the value of  $x_i$  where the diabatic potential curves cross and  $\Delta_i$  is the dimensionless shift of mode  $i$  (see equations II.29 - 31).  $V$  is the Hush coupling and  $\omega$  the frequency of the mode. Evaluating this expression with the experimental value of  $V = 4000 \text{ cm}^{-1}$  detailed above,  $V'_i$  varies slowly with respect to the vibrational wavefunctions and may be approximated by its value at the crossing point  $V'_i \approx -1 / 2\gamma$ . Equation IV.16 is now given:

Continuing with the expression of the electronic potentials as weakly perturbed

$$V_{NBO}^i = \frac{\hbar^2}{m_i} \sqrt{\frac{\lambda_i m_i \omega_i^2}{8V^2}} \frac{\Delta_i}{|\Delta_i|} \frac{\langle n_G | \frac{\partial}{\partial x_i} | n_E \rangle}{\langle n_G | n_E \rangle} \langle \chi_G | \chi_E \rangle . \quad (18)$$

quadratic functions of nuclear coordinates (see equation IV.12), the nuclear wavefunctions and its derivative is given by:

$$\langle n_G | \frac{\partial}{\partial x_i} | n_E \rangle = \sqrt{\frac{m_i \omega_i}{2\hbar}} \langle n_G | \hat{a} - \hat{a}^\dagger | n_E \rangle \quad (19)$$

where  $\hat{a}^\dagger$  is the creation and  $\hat{a}$  is the annihilation operator in the harmonic oscillator manifold. Using this result with the approximation  $n_E \approx 0$ :

$$V_{NBO}^i = \sqrt{\frac{\lambda_i (\hbar \omega_i)^3}{16V^2}} \cdot c_{n_G} \cdot \langle \chi_G | \chi_E \rangle , \quad c_{n_G} \equiv \frac{|\Delta_i|}{\sqrt{2}} - n_G \frac{\sqrt{2}}{|\Delta_i|} . \quad (20)$$

For the values of  $\Delta_i$  and  $n_G$  pertinent to the current EDA complex, it is estimated that the correction factor  $c_n$  has a value of approximately unity. The expression  $V'_i$  in equation IV.20 is evaluated by summing over the active interior modes of TCNE-HMB using the known frequencies and dimensionless shifts resulting in a non-Born- Oppenheimer coupling of  $500 \text{ cm}^{-1} \cdot \langle \chi_G | \chi_E \rangle$ .

#### Evaluation of Rate Expressions:

The Marcus electron transfer rate expression given in Chapter II and discussed above in equations IV.6 and IV.7 is evaluated using  $H_{RP} = 500 \text{ cm}^{-1}$  (the nuclear coupling value), the value of the solvent reorganization energy,  $\lambda_s$ , obtained from the absorption spectra fit as described above, and summed over the vibronic channels using the scaled equilibrium shifts of the interior modes observed in the resonance Raman profiles. The results of this calculation are given as  $\tau_1$  in Table IV.3 and plotted versus the solvation times measured in time dependent Stokes shift experiments in Figure IV.17 for the polar solvents examined in this study. The rates calculated in this manner exceed the experimental electron transfer values by a factor of  $\sim 3$  to 10.

The experimental electron transfer rates (and the theoretical rates calculated as  $\tau_1$ ) exceed or are approximately equivalent to the solvent relaxation times as determined by dynamic Stokes shift experiments and plotted in Figure IV.17. A number of workers including Walker *et al.* [16,19,29,30] and Sumi and Marcus [20] have derived theoretical rate expressions describing systems reacting over nonequilibrated reaction modes such as nonequilibrium polarization conditions. These treatments describe the reacting system's motion along a classical coordinate by a diffusion equation; a reaction rate is calculated for each position along the classical path.

The electron transfer in the molecular complex TCNE-HMB is an internal conversion process as the system makes a transition from a low lying vibrational state of the electronic reactant state to a high lying vibrational state of the electronic product

state. The set of high lying vibrational states which comprise the product states are the accepting modes of the reaction. For reactions of large driving force anharmonicity serves to couple the initial product state to a number of dark modes which serve as the dephasing bath for the electron transfer reaction [31]. Second order perturbation theory can be used to write the reaction rate as a function of the driving force:

$$k^{(2)}(G) = \frac{|H_{RP}|^2}{\hbar^2} \int_{-\infty}^{\infty} \prod_i \langle 0_i | 0_i(t) \rangle \exp\{-i G t / \hbar - g(t)\} dt, \quad (21)$$

where  $g(t)$  is the dephasing function which serves to damp the vibronic correlation function. Recalling the discussion in Chapter II of the frictionally damped oscillator model [II.27, II.28] where  $D$  represents the coupling strength between the solvation coordinate and the transition and the solvent time scale is  $\hbar / \Lambda$  :

$$g_R(t) = \left(\frac{D^2}{\Lambda^2}\right) \left[ e^{-\frac{\Lambda t}{\hbar}} - 1 + \frac{\Lambda t}{\hbar} \right] \quad (22)$$

the Kubo dephasing function smoothly interpolates between Lorentzian and Gaussian line shapes.

The vibrational component of a vibronic channel of the electronic transfer transition consists of a transition from a low-lying vibrational state to an anharmonically coupled high lying state; the analogous process is observed in vibrational overtone spectra. The  $5\nu_{CH}$  transition in gaseous benzene, which occurs at

approximately the energy of the driving force for the TCNE-HMB electron transfer reaction, has a FWHM of  $111\text{cm}^{-1}$  [32]. Similar line widths at this transition energy are observed for aromatic overtone transitions in HMB [33] and durene [33]. Therefore  $100\text{ cm}^{-1}$  will be used in the dephasing kernel  $g(t)$  for the evaluation of equation IV.21.

The motion of the TCNE-HMB reacting system is simulated by a Smoluchowski diffusion equation [34, 35] in the underdamped limit with diffusion constant  $k_B T / \tau_L$  [20]. The solvent coordinate  $X$  is defined such that  $X=0$  marks the reactant origin and  $X=1$  the origin of the product. The driving force for the reaction, i.e. the free energy gap between at the classical surfaces is a function of  $X$  given by  $G(X) = \Delta G^0 + \lambda_s - 2 \lambda_s X$ .

The initial, thermal distribution centered at  $X=1$  is projected on to the reactant surface and numerically propagated as described by Agmon and Hopfield [34]. The continuous solvent variable  $X$  is divided into a grid; after each propagation, the rate of electron transfer at that solvent position is calculated using equation IV.21. Integration of the distribution function over  $X$  results in the survival probability and represents the unreacted species. Time integration of the reactant state survival probability gives the theoretical electron transfer time  $\tau_2$  listed in Table IV.3 and plotted in Figure IV.17. The agreement with the experimental results is much improved over the theoretical rates calculated assuming infinitely fast solvent relaxation ( $\tau_1$ ). Also, the pattern of the experimental rates with respect to the driving force is well produced.

A few caveats may be appropriate here. The longitudinal relaxation time  $\tau_L$  is a tenet of dielectric continuum theory, which models the solvent as an isotropic, polarizable medium without molecular structure. Although the longitudinal relaxation times used to analyze the present data are single exponential results of transient Stokes shifts, the response of a real solvent to an instantaneously created charge distribution undoubtedly contains motion along a number of translational, rotational, as well as electronic degrees of freedom. Recent molecular dynamics computer simulations [36, 37] and femtosecond Stokes shift measurements [38] seem to indicate multicomponent solvation, including fast inertial responses that comprise as much as 80% of the relaxation. Improved time resolution in dynamic spectroscopic measurements and continued molecular dynamics calculations will be required to elucidate further these solvation components.

### Discussion and Conclusion

The electron transfer rates of TCNE-HMB in a variety of solvents were experimentally measured using femtosecond transient spectroscopy. Good theoretical predictions for these rates were calculated using an internal conversion model incorporating all available knowledge regarding interior modes coupled to the electron transfer, solvent reorganization energies, driving forces for the reaction, and non-Born-Oppenheimer coupling between the product and reactant surfaces. Below, a few

shortcomings of the analysis will be discussed.

The resonance Raman scattering applied to direct electron transfer systems yields information only about the ground state vibrations and only in the Frank-Condon region. The electron transfer internal conversion, however, involves a vibronic transition from a vibrational state in the excited potential to a high lying vibrational state in the ground state potential. As the new charge distribution of the ionic state is accessed, it seems reasonable that frequency shifts in nuclear modes may accompany this transition. The relevant Frank-Condon transmission factor in this instance must include this frequency change. Also, for reactions of large driving force, the normal mode picture employed in the TCNE-HMB analysis may be inapplicable as a result of large anharmonicities in the product state. Studies of electron transfer reactions proceeding by driving forces on the order of a couple thousand wavenumbers at most would be valuable, since these transitions should occur in the harmonic potential region. Product state distribution of the accepting modes could be examined by vibrational pump-probe spectroscopy. Such examinations could also probe the role of "dark" modes in electron transfer reactions as the free energy of the reaction is distributed amongst the nuclear modes in the ground electronic state. Vibrational relaxation in these non-Frank-Condon active modes is not probed by transient optical spectroscopy.

Another issue ignored in this discussion of electron transfer dynamics is the role of the coupling between bath vibrational modes and low frequency interior modes. In

the present example of TCNE-HMB, examples of low frequency interior modes which may be strongly coupled to the bath include the modes comprised of relative motion of the TCNE and HMB such as the tilt or rocking motions. Motion along these coordinates may be quite important with regard to the charge recombination process, as the relative orientation of the donor and acceptor alters. The frequency of these modes may be low enough to hinder their detection in the frequency domain. Most current modelling of the solvent-interior mode interactions assume weak interactions which give rise to exponential decays of coherence and populations. However strong coupling between the bath and the torsional intramolecular coordinate has been shown to be important in excited state isomerization.

Finally, in the analysis above, the electronic coupling matrix element responsible for the electron transfer arises from the non-Born-Oppenheimer nuclear term which serves to couple the vibronic states. The state that is excited by the light pulse, an adiabatic vibronic state which is initially a coherent superposition of diabatic vibronic states ( see equations IV.13 and IV.14), is a Born-Oppenheimer state that can only decay when the nuclear motion provides the perturbation which serves to couple the reactant and product surfaces. However, the coordinate position dependence of the  $|N\rangle$  and  $|I\rangle$  states was ignored. The electronic coupling term calculated using the Mulliken expressions above must be considered a substantial approximation; neither was the position dependence of the diabatic coupling analyzed. A much more elaborate electronic structure calculation would be required to estimate these relevant matrix



elements without such considerable approximations. However, the reasonable agreement between the experimental and predicted rates may indicate the validity of the approximation.

## CHAPTER IV

### References

- 1 R.A.Marcus and N.Sutin, *Biochim. Biophys. Acta*, **811**, (1986), 265
- 2 J.Jortner, *J. Chem. Phys.*, **64**, (1976), 4860
- 3 a) G.Briegleb, *Elektronen-Donator-Acceptor-Komplexe*,  
(Springer, Berlin, 1961)  
b) R.S.Mulliken, W.B.Person, *Molecular Complexes*,  
(Wiley, New York, 1969)  
c) N.Mataga, T.Kubota, *Molecular Interactions and Electronic Spectra*,  
(Dekker, NewYork, 1970)
- 4 J.Michl, *Molec. Photochem.*, **4**, (1972), 253
- 5 W.Liptay, T.Rehm, L.Schanne, W.Baumann, W.Lang,  
*Z. Naturforsch.*, **A37**, (1982), 1427
- 6 M.Saheki, H.Yamada, H.Yoshioka, K.Nakatsu, *Acta Cryst.*, **B32**, (1976), 662
- 7 E.Maverick, K.N.Trueblood, D.A.Bekoe, *Acta Cryst.*, **B34**, (1978), 2777
- 8 F.Markel, N.S.Ferris, I.R.Gould, A.B.Myers,  
*J. Am. Chem. Soc.*, **114**, (1992), 6208
- 9 M.Rossi, U.Buser, E.Haselbach, *Helv. Chim. Acta* **59**, (1976), 1039

- 10 E.F.Caldin, J.E.Crooks, D.O'Donnell, D.Smith, S.Toner,  
*Chem. Soc. J., Faraday Trans., Pt. 1*, **68**, (1972), 849
- 11 S.Ruhman, L.Williams, A.G.Joly, B.Kohler, K.A.Nelson,  
*J. Phys. Chem.*, **91**, (1987), 2237
- 12 S.Ruhman, B.Kohler, A.G.Joly, K.A.Nelson,  
*Chem. Phys. Lett.*, **141**, (1987), 16
- 13 D.L.Jeanmaire, M.R.Suchanski, R.P.van Duyne,  
*J. Am. Chem. Soc.*, **97**, (1975), 1699
- 14 P.F.Barbara, W.Jarzeba, *Adv. Photochem.*, **15**, (1990), 1
- 15 G.C.Walker, E.Åkeson, A.E.Johnson, N.E.Levinger, P.F.Barbara,  
*J. Phys. Chem.*, **96**, (1992), 3728
- 16 R.J.Sension, A.Z.Szarka, R.M.Hochstrasser, *J. Chem. Phys.*, **97**, (1992), 5239
- 17 D.Ben-Amotz, C.B.Harris, *J. Chem. Phys.*, **86**, (1987), 4856
- 18 K.Tominaga, D.A.V.Kliner, A.E.Johnson, N.E.Levinger, P.F.Barbara,  
*J. Chem. Phys.*, **98**, (1993), 1228
- 19 H.Sumii and R.A.Marcus, *J. Chem. Phys.*, **84**, (1986), 4894
- 20 J.Jortner and M.Bixon, *J. Chem. Phys.*, **88**, (1988), 167
- 21 T.Asahi and N.Mataga, *J. Phys. Chem.*, **95**, (1991), 1956
- 22 T.Asahi and N.Mataga, *J. Phys. Chem.*, **93**, (1989), 6575
- 23 N.S. Hush, *Electrochim. Acta*, **13**, (1968), 1005
- 24 S.Efrima and M.Bixon, *J. Chem. Phys.*, **64**, (1976), 3639

- 25 S.Efrima and M.Bixon, *Chem. Phys.*, **13**, (1976), 447
- 26 T.Kobayashi, Y.Takagi, H.Kandori, K.Kemnitz, K.Yoshihara,  
*Chem. Phys. Lett.*, **180**, (1991), 416
- 27 Y.J.Yan and S.Mukamel, *J. Chem. Phys.*, **85**, (1986), 5908
- 28 A.B.Myers, R.A.Mathies, *Biological Applications of Raman Spectroscopy*,  
T.G. Spiro editor, (Wiley, New York, 1987)
- 29 P.F.Barbara, G.C.Walker, T.P.Smith, *Science* , **256**, (1992), 975
- 30 E.Åkeson, G.C.Walker, P.F.Barbara, *J. Chem. Phys.*, **95**, (1991), 4188
- 31 K.F.Freed, in *Radiationless Processes in Molecules and Condensed Phases*,  
editor: F.K. Fong, (Springer, Berlin, 1976)
- 32 K.V.Reddy, D.F.Heller, M.J.Berry, *J. Chem. Phys.*, **76**, (1982), 2814
- 33 J.W.Perry, A.H.Zewail, *J. Phys. Chem.*, **85**, (1981), 933
- 34 N. Agmon and J.J. Hopfield, *J. Chem. Phys.*, **78**, (1983), 6947
- 35 B. Bagchi, and G.R. Fleming, *J. Phys. Chem.*, **94**, (1990), 9
- 36 M.Maroncelli, *J. Chem. Phys.*, **94**, (1991), 2084
- 37 E.A.Carter, J.T.Hynes, *J. Chem. Phys.*, **94**, (1991), 5961
- 38 S.J.Rosenthal, X.Xie, M.Du , G.R.Fleming, *J. Chem. Phys.*, **95**, (1991), 4715

**Figure IV.1** Experimental absorption spectrum of the charge transfer band in TCNE-HMB. Vertical arrow indicates excitation wavelength for the transient data presented in this thesis.

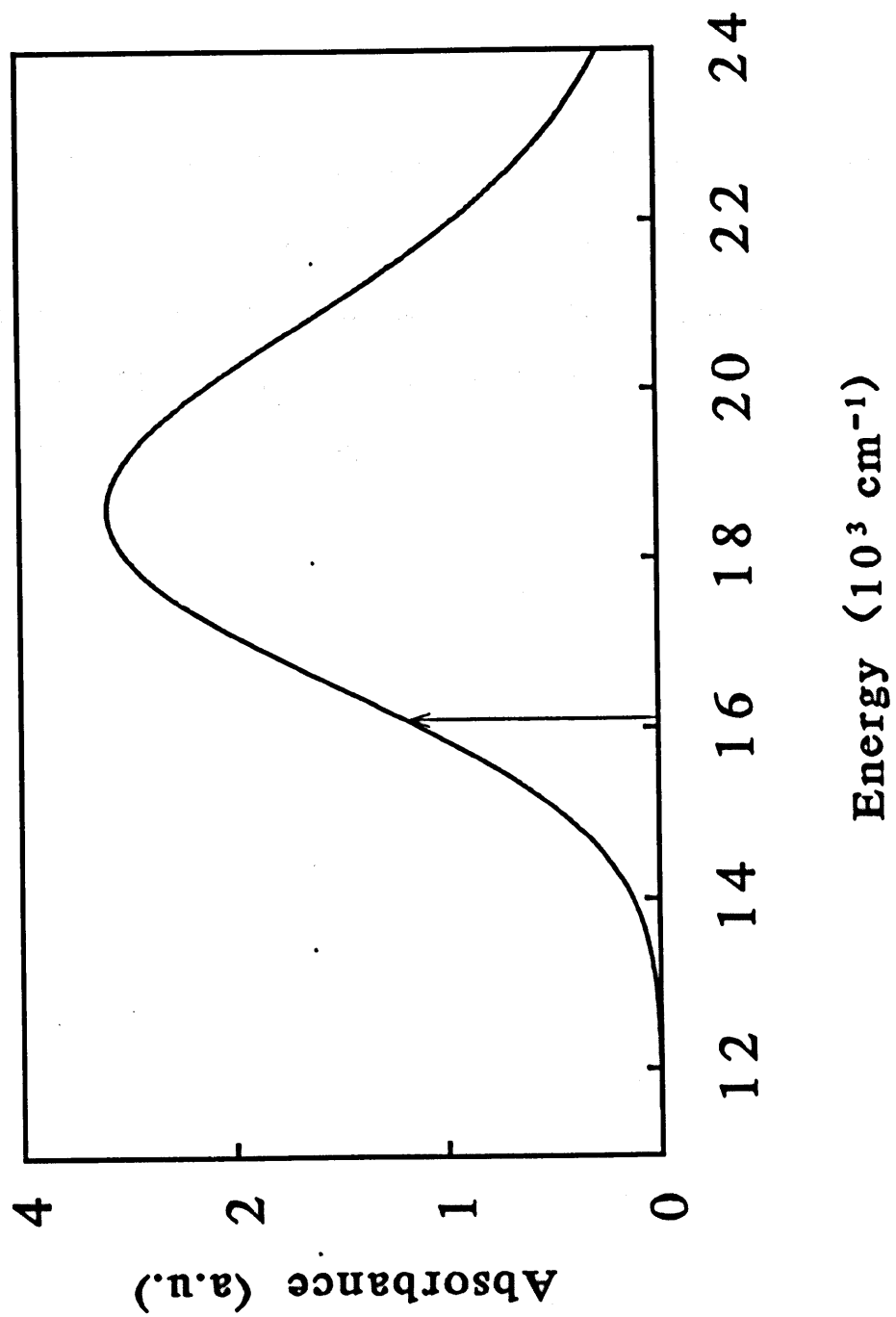
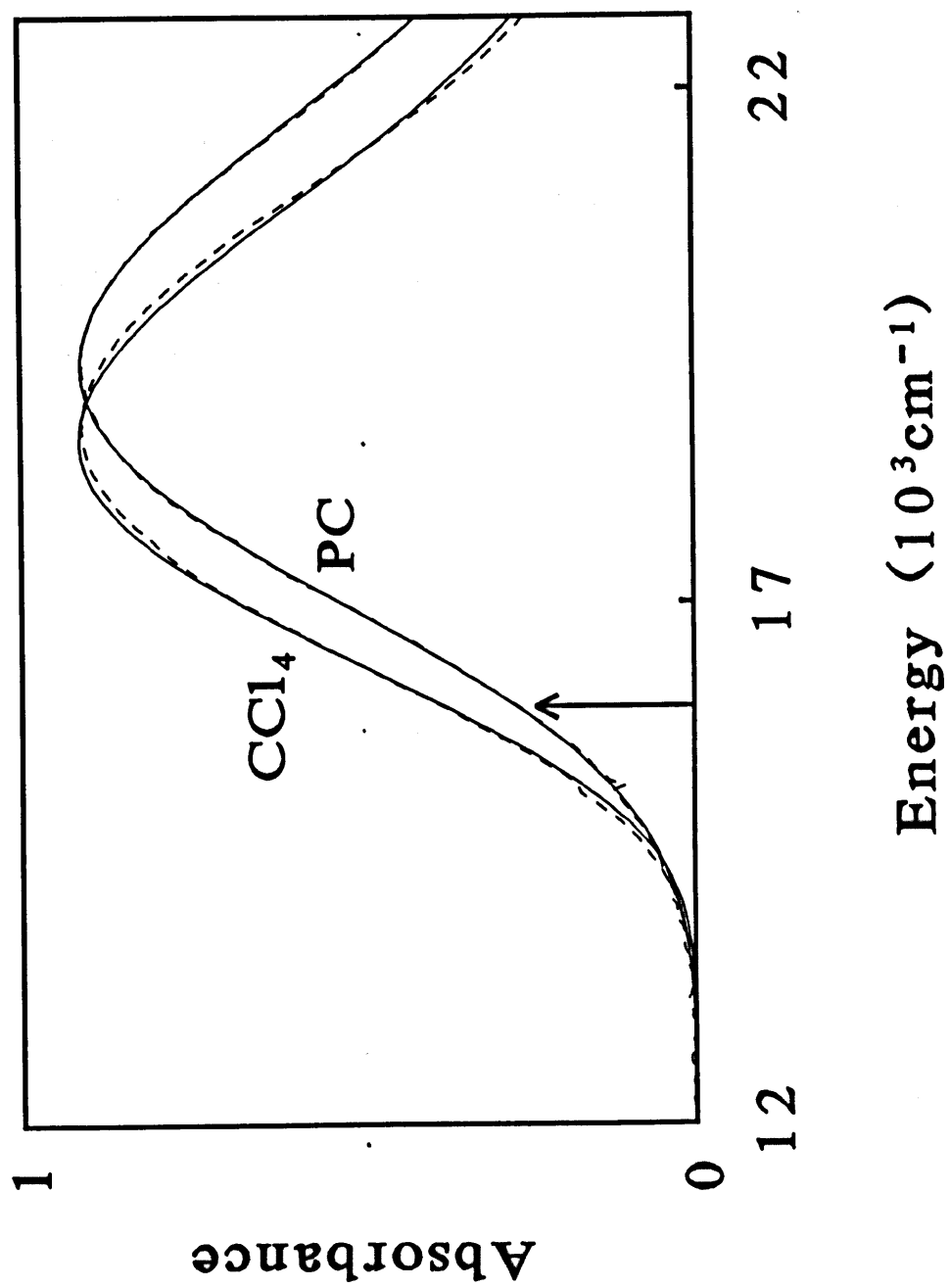


Figure IV.2 Experimental absorption spectrum (dashed lines) of the charge transfer band in TCNE-HMB with fits (solid lines) as detailed in text. These fits were performed to obtain solvent reorganization energies and driving forces. The solvents in the figure are:  $\text{CCl}_4$ , carbon tetrachloride and PC, propylene carbonate. Note the small peak shift relative to line width.





**Figure IV.3** Morse potentials of the ground and first excited electronic states for the molecular complex TCNE-HMB calculated along the donor - acceptor stretch. Thin lines are crude adiabatic surfaces calculate with constant coupling of  $V = 4000 \text{ cm}^{-1}$ . See text for details.

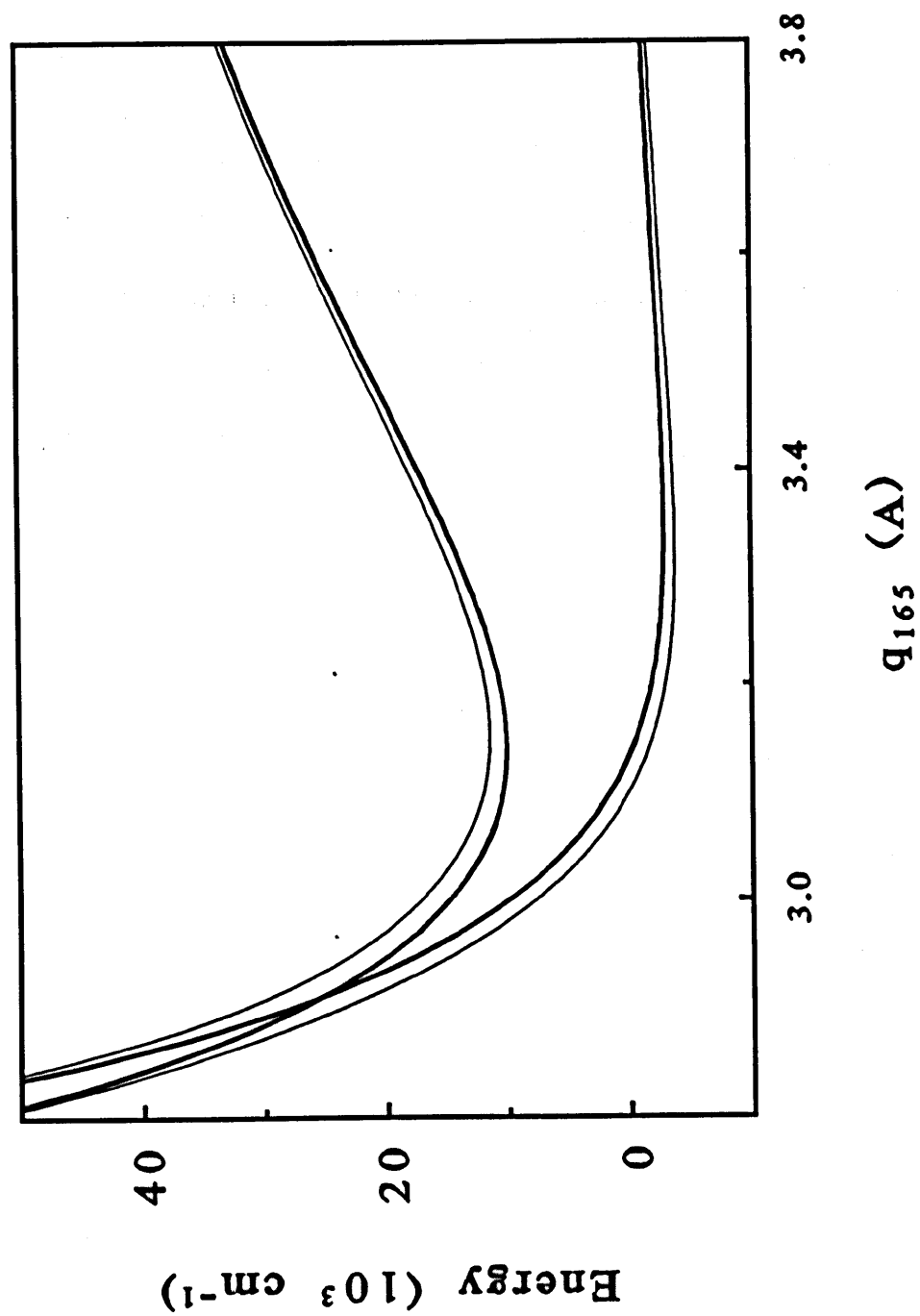


Figure IV.4 Transient bleach recovery measured for the molecular complex TCNE-HMB in cyclohexane. Excitation wavelength: 620 nm.; probe wavelength: 620 nm. Open circles are the data points, solid line is the fit with exponential decay 11.2 ps., damped oscillation of  $161.7\text{ cm}^{-1}$ , damping time 1.4 ps. Inset shows data and fit with exponential decay subtracted.

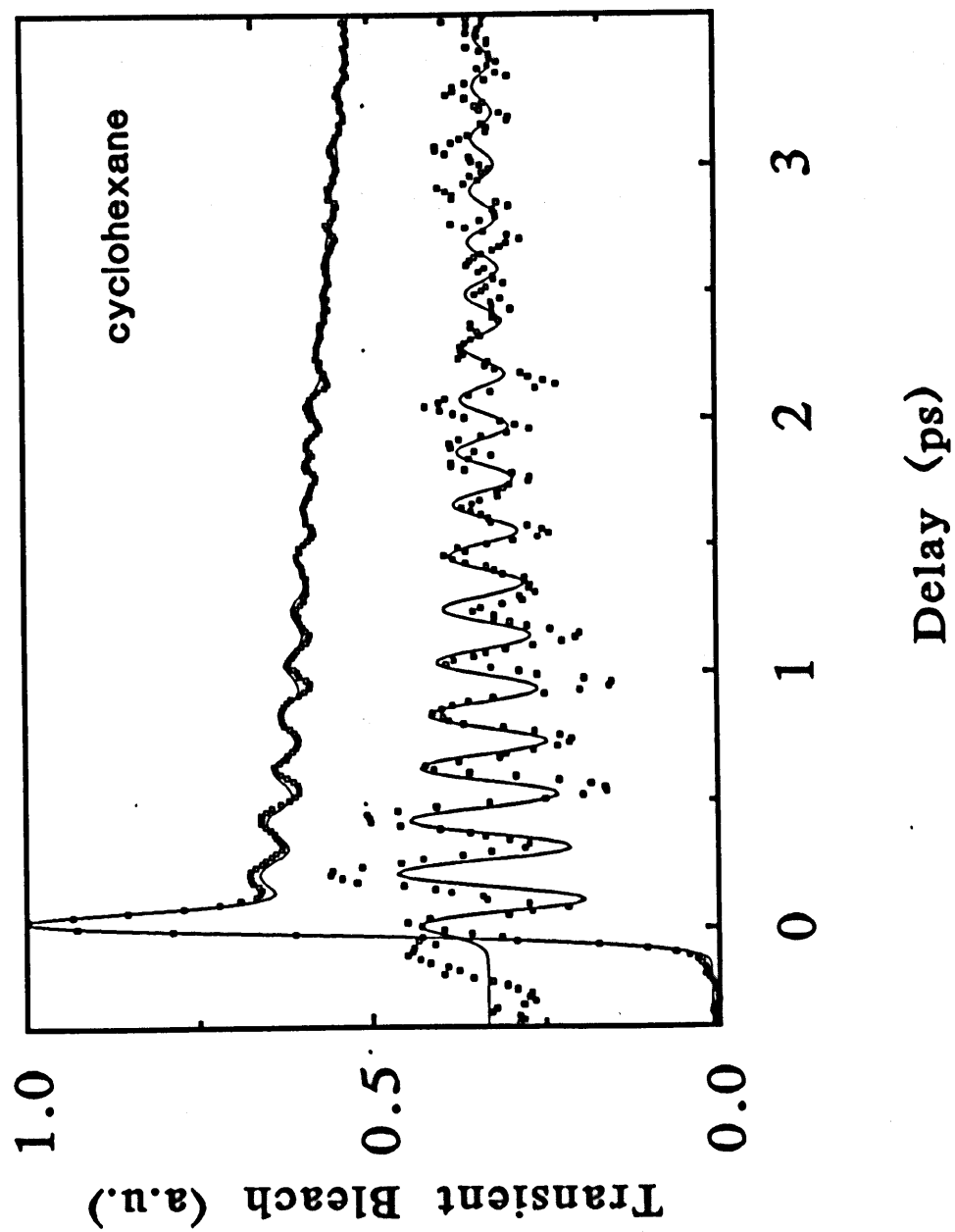
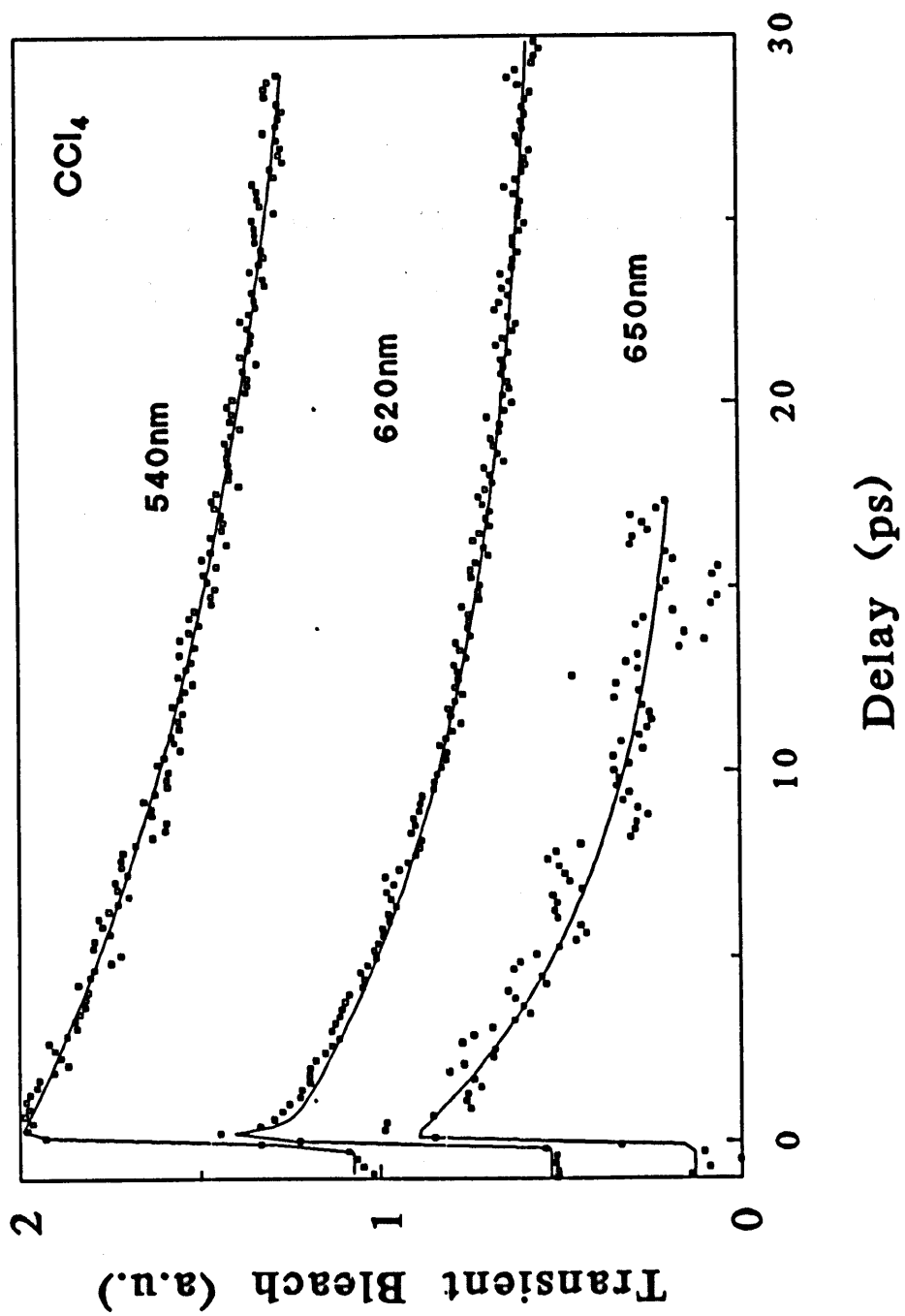


Figure IV.5 Transient bleach of TCNE-HMB in the nonpolar solvent carbon tetrachloride. Excitation wavelength: 620 nm.; probe wavelength as indicated in figure. Open circles are data points, solid line through data is fit detailed in text.



**Figure IV.6** Transient data for TCNE-HMB in glycerol triacetate. Excitation wavelength: 620 nm.; probe wavelength: 620 nm. Open circles are data points, solid line through data is fit detailed in text. Fit parameters are listed in Table IV.3.

Transient Bleach

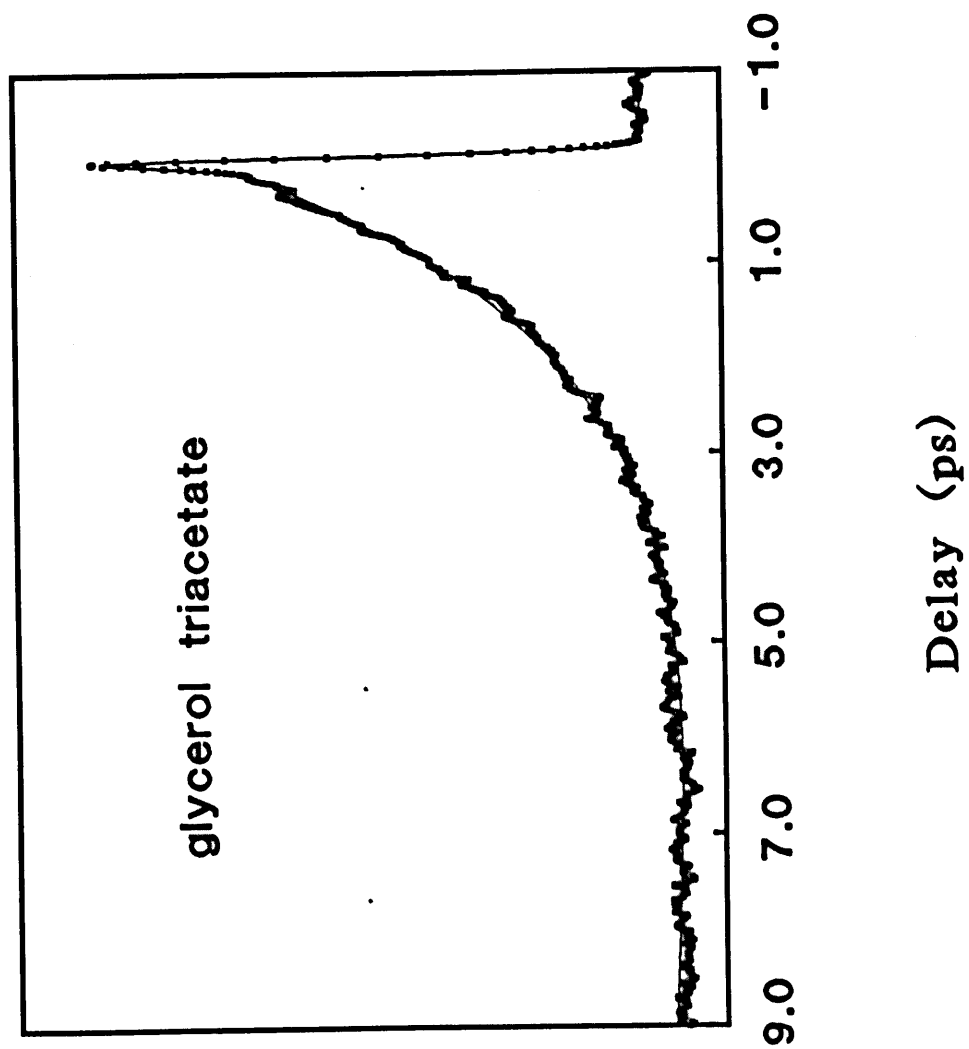
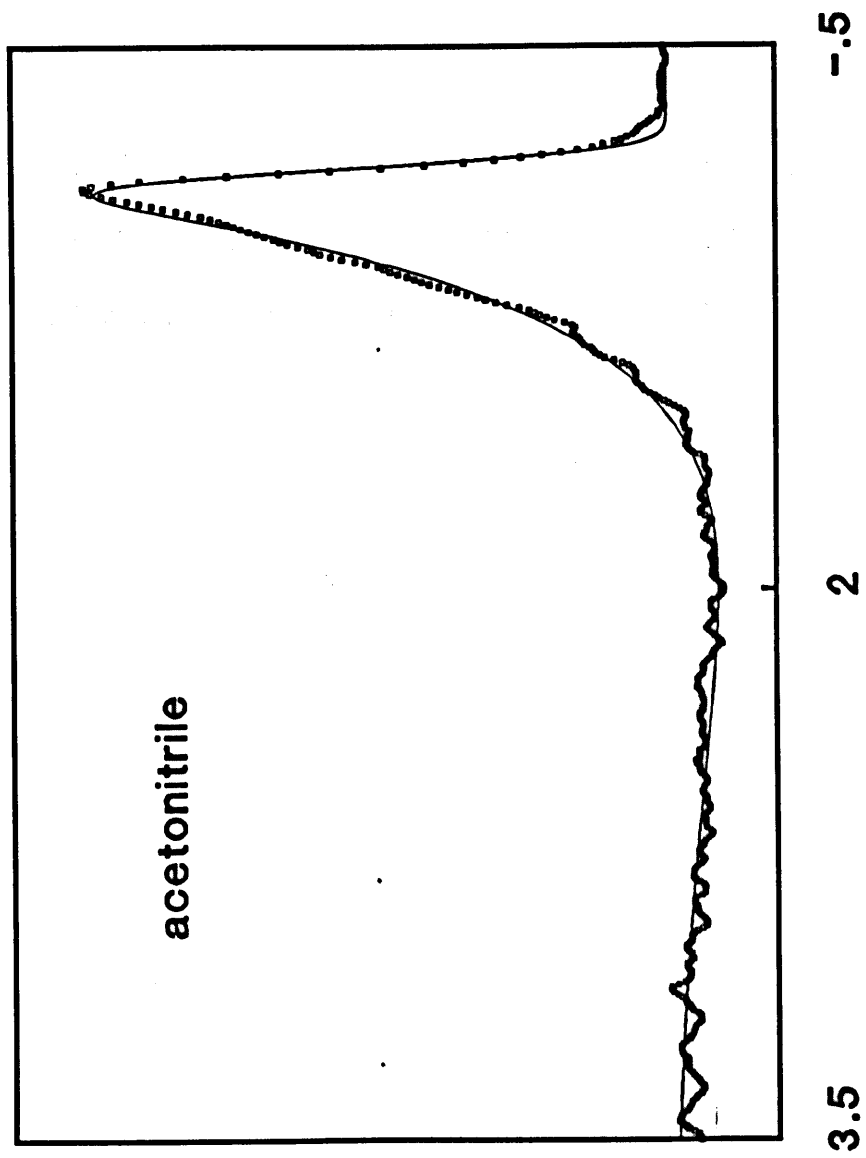




Figure IV.7 Transient data for TCNE-HMB in the polar solvent acetonitrile. Excitation wavelength: 620 nm.; probe wavelength: 620 nm. Open circles are data points, solid line through data is fit detailed in text. Fit parameters are listed in Table IV.3.

Transient Bleach

acetonitrile



**Figure IV.8** Transient data for TCNE-HMB in the polar solvent acetone. Excitation wavelength: 620 nm.; probe wavelength: 620 nm. Open circles are data points, solid line through data is fit detailed in text. Fit parameters are listed in Table IV.3.

Transient Bleach

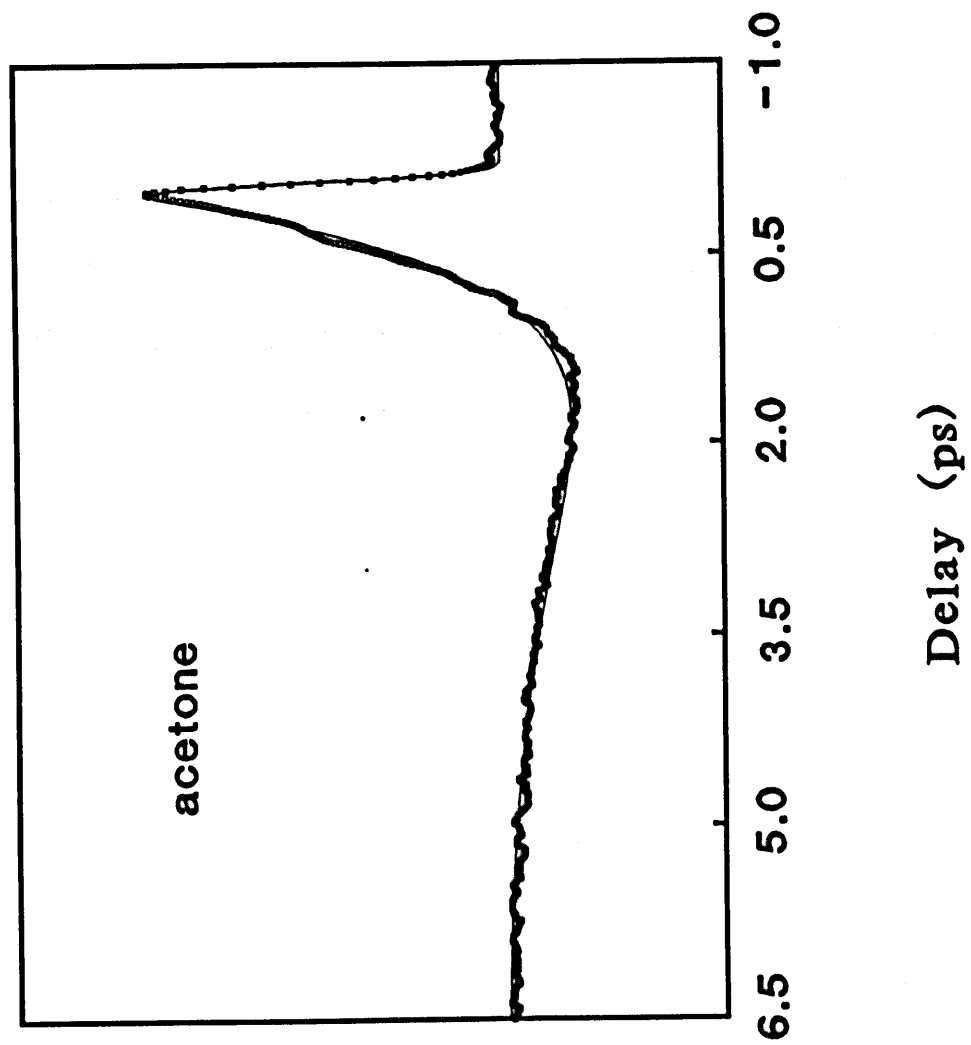


**Figure IV.9** Transient data for TCNE-HMB in the polar solvent ethylene acetate. Excitation wavelength: 620 nm.; probe wavelength: 620 nm. Open circles are data points, solid line is fit detailed in text. Note decay of transient bleach into transient absorption. Oscillations on falling edge of signal indicate nuclear coherence of ensemble.

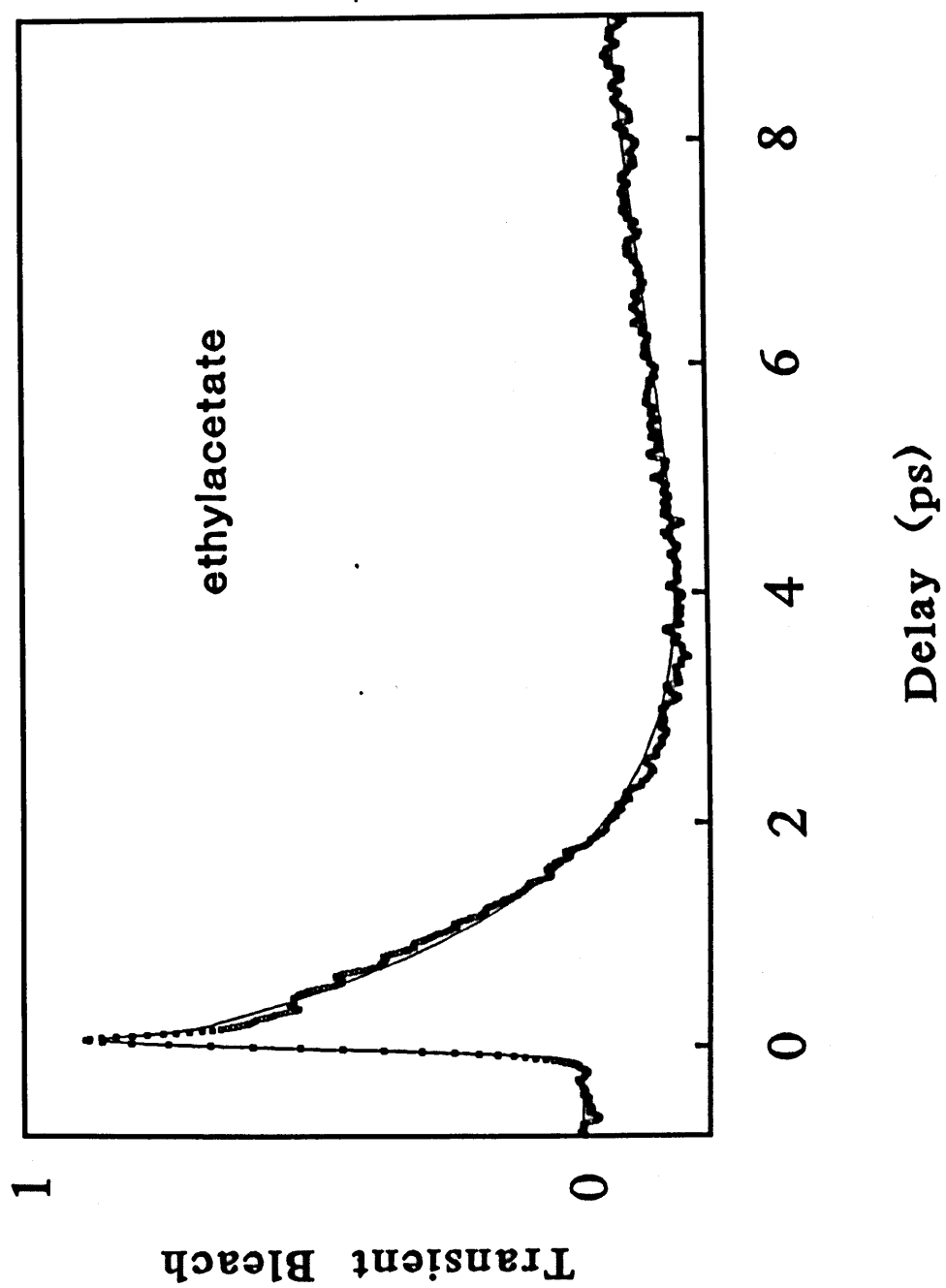


**Figure IV.10** Transient data for TCNE-HMB in the polar solvent tetrahydrofuran. Excitation wavelength: 620 nm.; probe wavelength: 620 nm. Open circles are data points, solid line through data is fit detailed in text. Fit parameters are listed in Table IV.3.

Transient Bleach

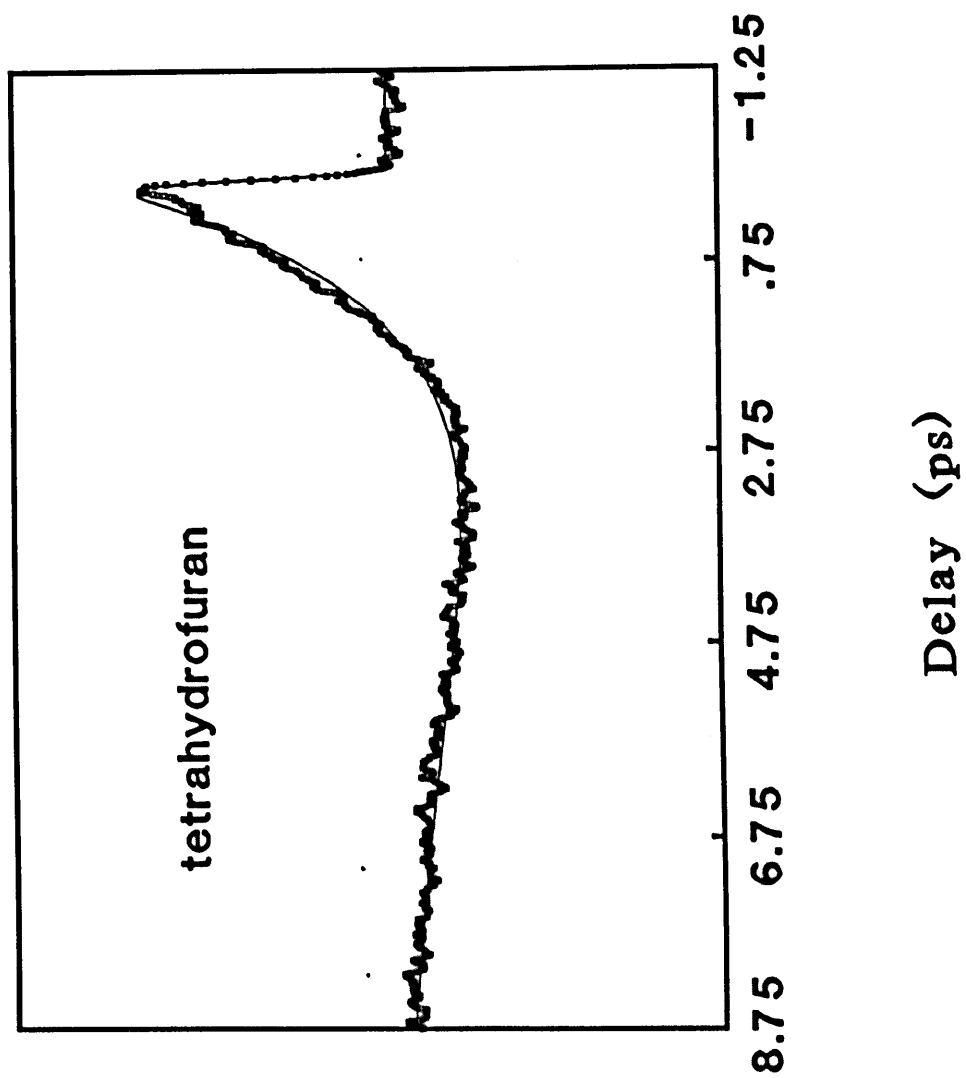




Figure IV.11 Transient data for TCNE-HMB in the polar solvent nitrobenzene. Excitation wavelength: 620 nm.; probe wavelength: 620 nm. Open circles are data points, solid line through data is fit detailed in text. Fit parameters are listed in Table IV.3.

Transient Bleach

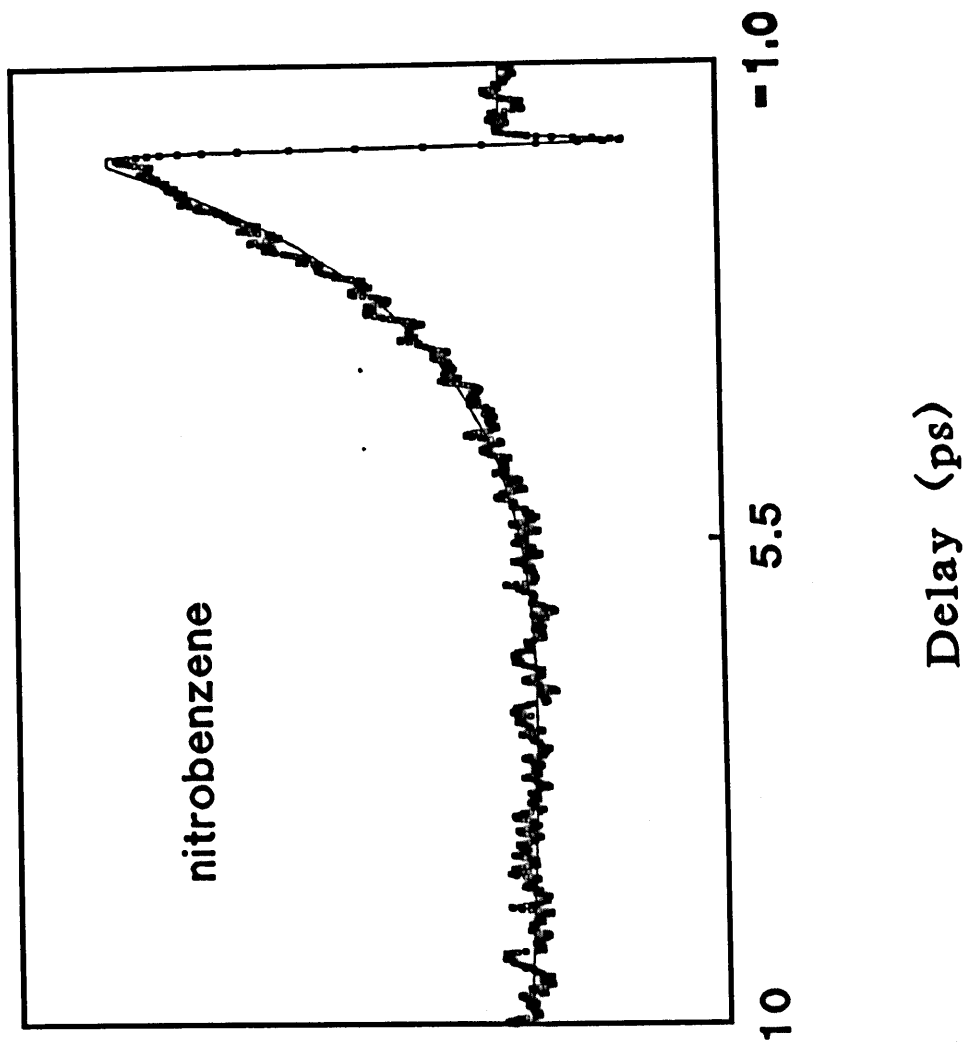


Figure IV.12 Transient data for TCNE-HMB in the polar solvent trichloroethene. Excitation wavelength: 620 nm.; probe wavelength: 620 nm. Open circles are data points, solid line through data is fit detailed in text. Fit parameters are listed in Table IV.3.

# Transient Bleach

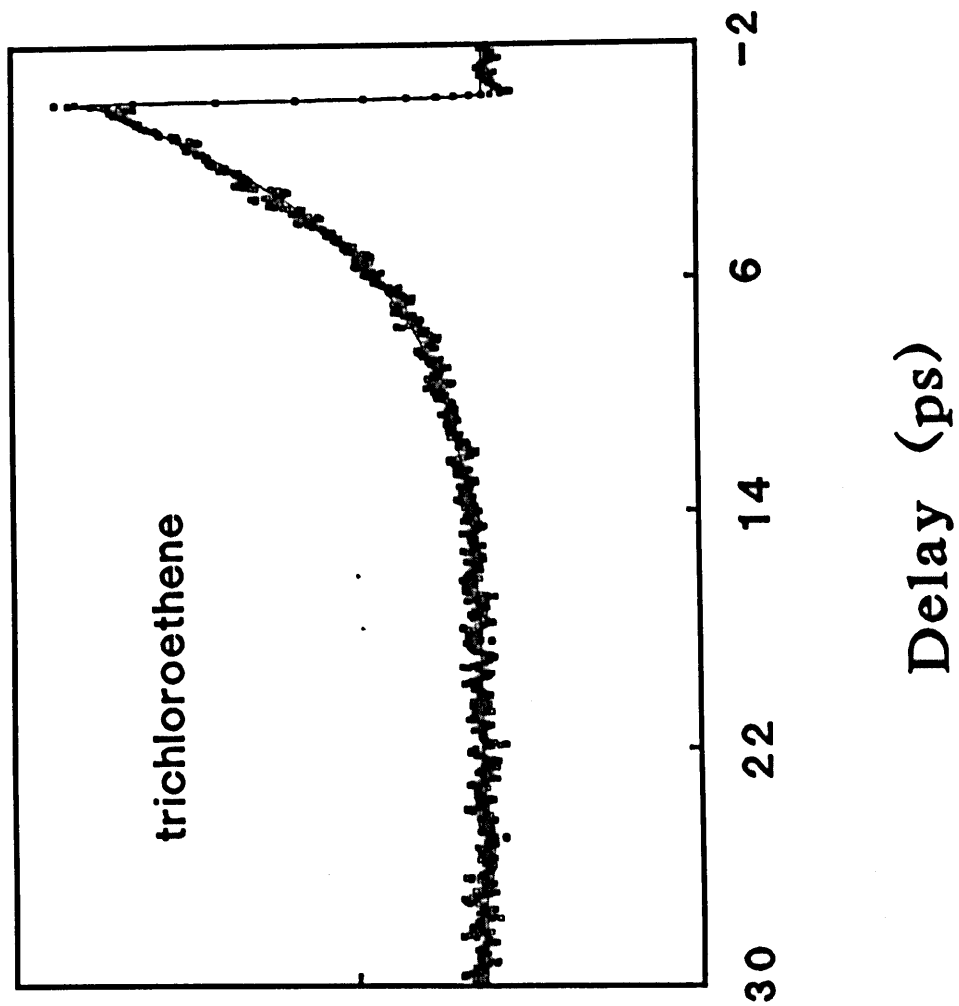


Figure IV.13 Transient data for TCNE-HMB in the polar solvent butyronitrle. Excitation wavelength: 620 nm.; probe wavelength: 620 nm. Open circles are data points, solid line through data is fit detailed in text. Fit parameters are listed in Table IV.3.

Transient Bleach

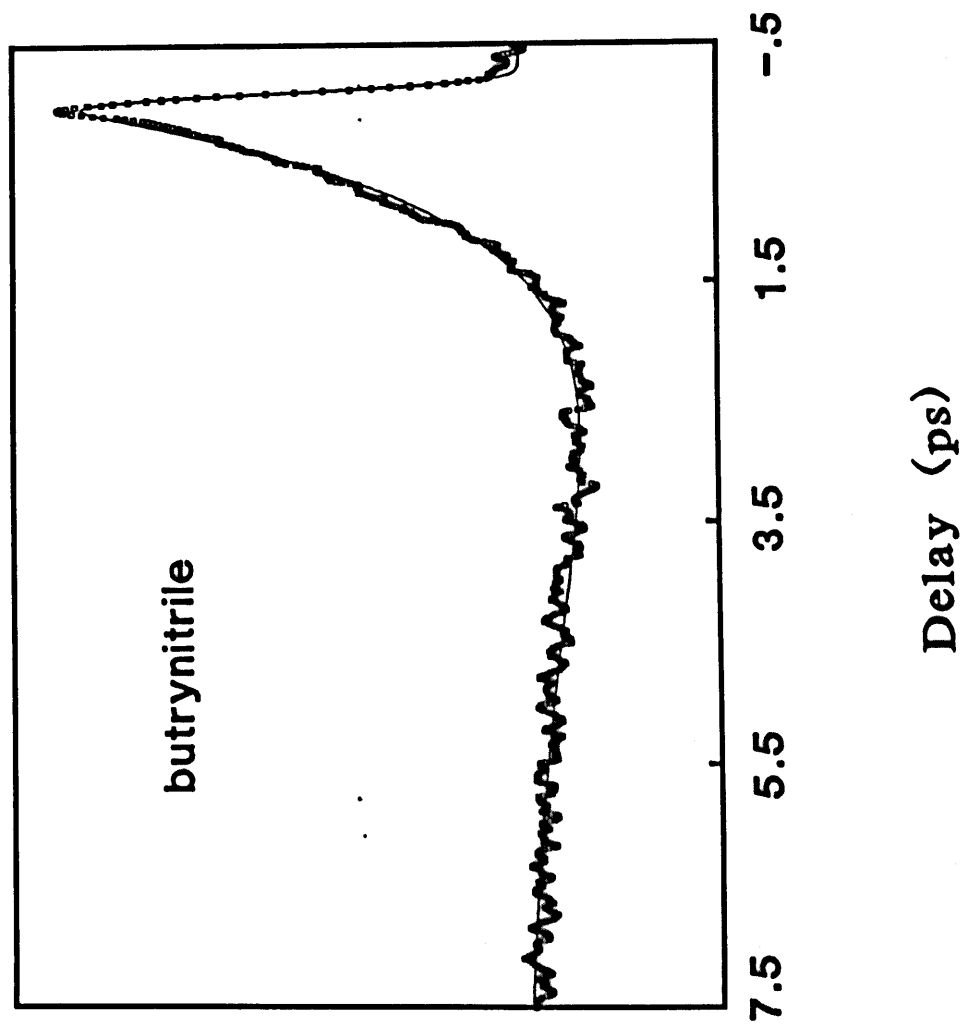


Figure IV.14 Transient data for TCNE-HMB in the polar solvent acetonitrile. Excitation wavelength: 620 nm.; probe wavelength as indicated in figure. Open circles are data points, solid line through data is fit detailed in text. Solid horizontal lines indicate zero for each probe wavelength.

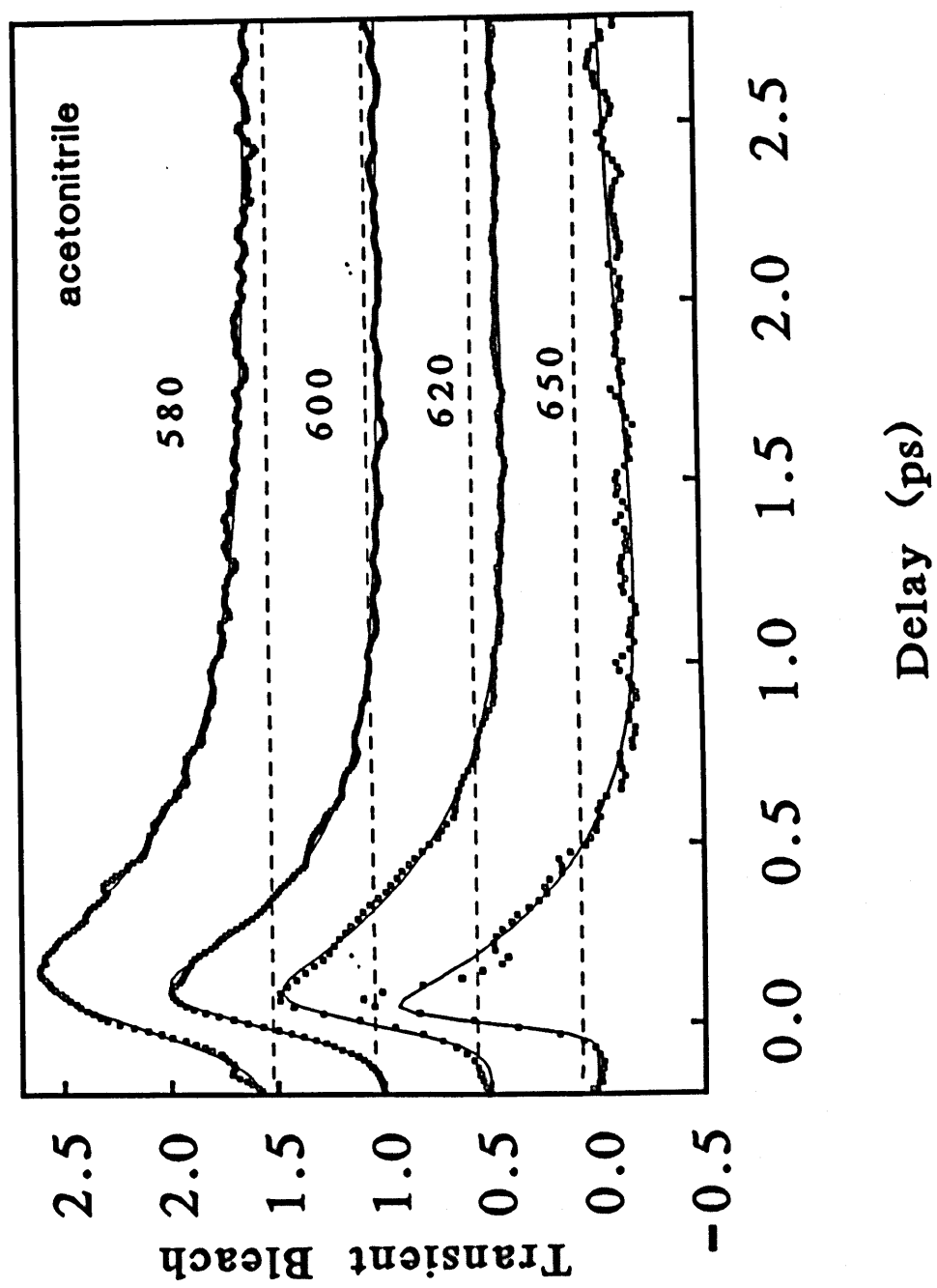




Figure IV.15 Transient data for TCNE-HMB in carbon tetrachloride. Excitation wavelength: 620 nm.; probe wavelength: 450 nm. Open circles are data points, solid line through data is fit detailed in text. This is a transient absorption of the TCNE<sup>-</sup> anion.

Transient Absorption

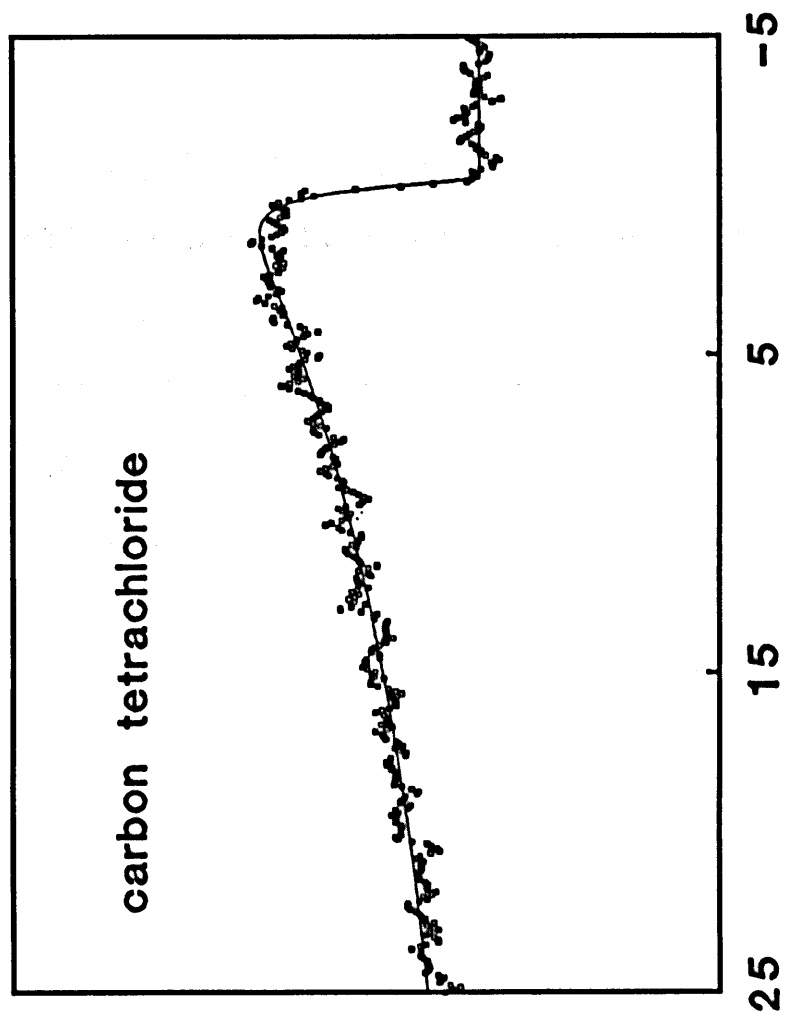


Figure IV.16 Experimentally determined solvent dependent charge recombination times for TCNE-HMB plotted versus solvent relaxation time. The solid line indicates an electron transfer time equal to the solvent relaxation time. Note scale break in abscissa. In fast solvents, ( $\tau_L < 2$  ps), the charge recombination time  $\sim \tau_L$ . In slower solvents, ( $\tau_L > 2$  ps), the charge recombination time may be governed by the dynamics of the interior modes.

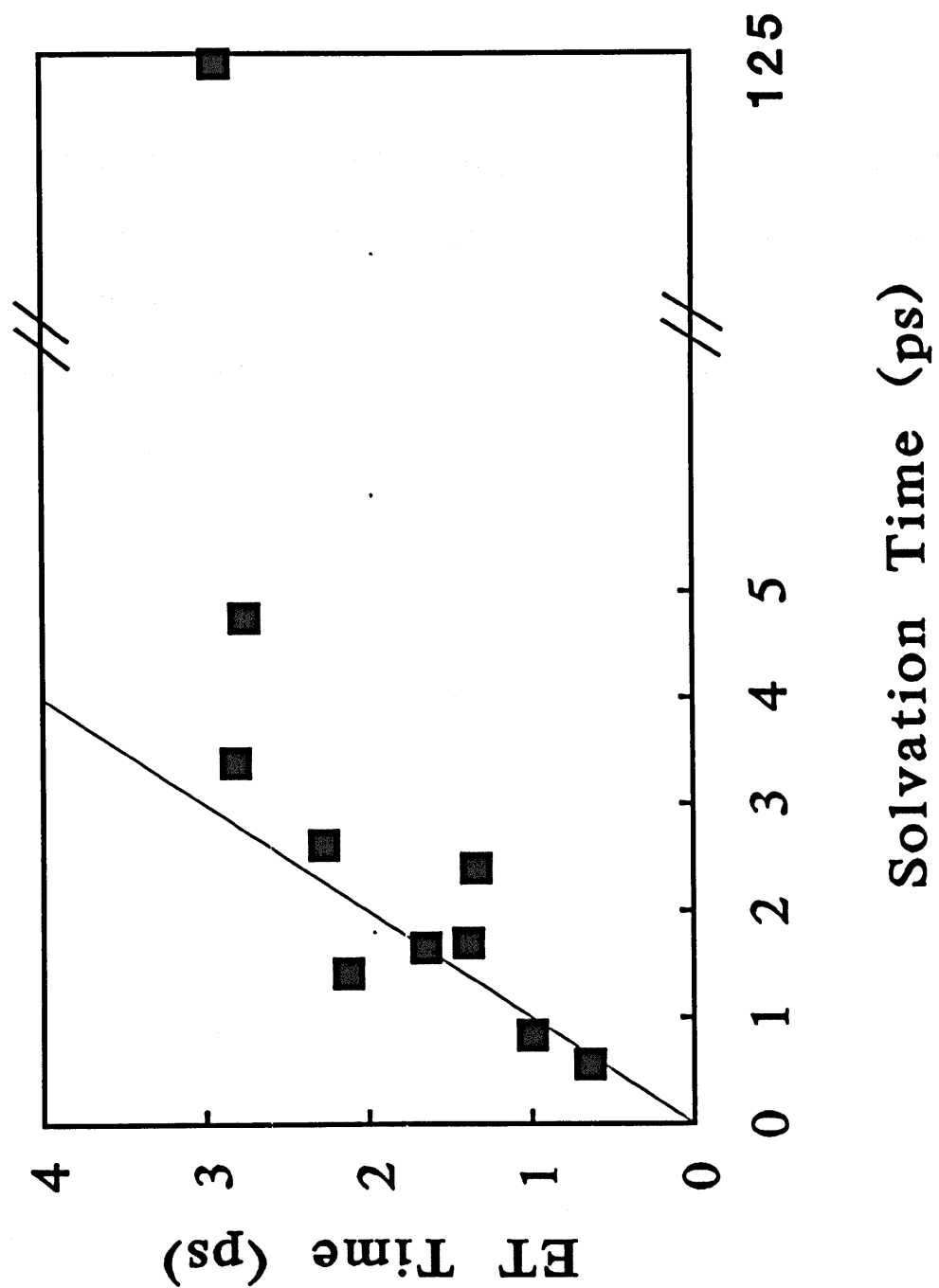


Figure IV.17 Measured and calculated charge recombination times in TCNE-HMB in polar solvents versus solvent relaxation time. The solid squares correspond to the experimentally observed ET times whereas the open circles and open squares correspond to the  $\tau_1$  and  $\tau_2$  times respectively listed in Table IV.3 and discussed in the text. Note that the fluctuations in the rates are mainly due to the static effect of the polarity of the different solvents used.

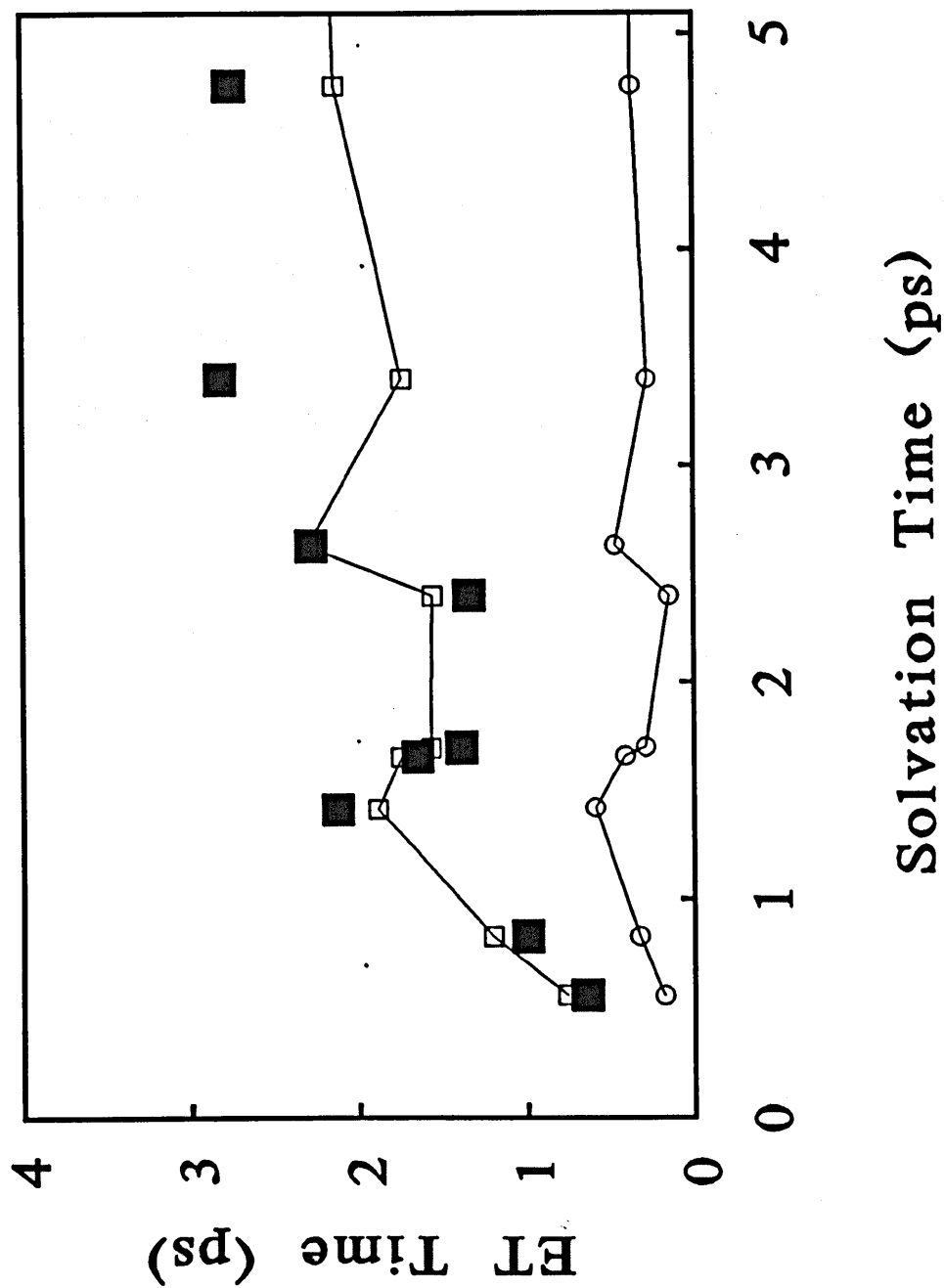


Figure IV.18 Population distribution versus vibrational quantum number of the 165  $\text{cm}^{-1}$  accepting mode of TCNE-HMB using classical reorganization energy  $\lambda_s = 1000 \text{ cm}^{-1}$ ,  $V = 4000 \text{ cm}^{-1}$  and  $T = 298 \text{ K}$ . For narrow distribution centered at  $n \sim 5$ ,  $\Delta G^0 = -.300 \text{ eV}$ . For broadest distribution centered at  $n \sim 12$ ,  $\Delta G^0 = 1.7 \text{ eV}$ . At large driving forces, the high frequency modes become the important accepting modes.

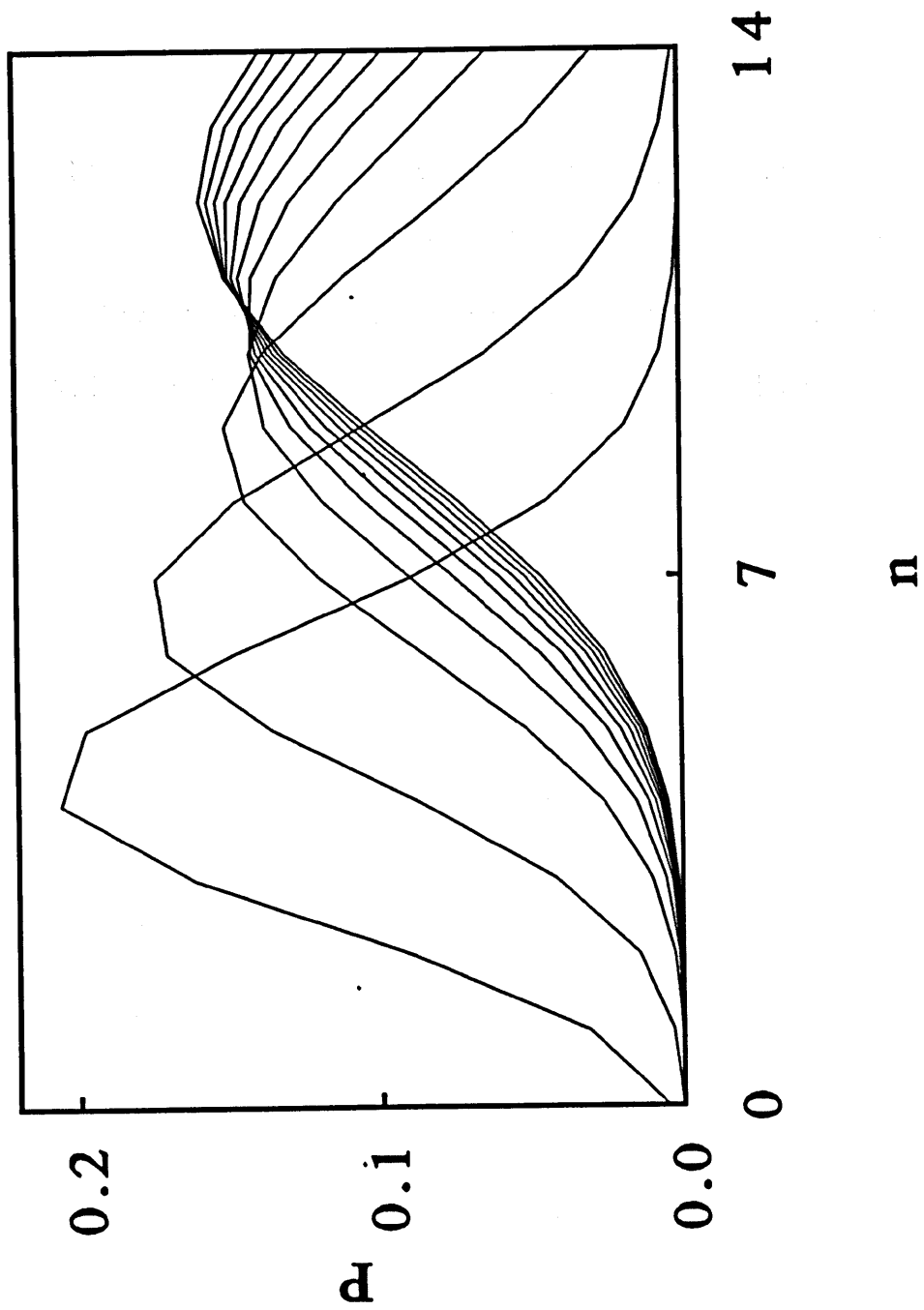




Figure IV.19 Population distribution versus vibrational quantum number of the 1551  $\text{cm}^{-1}$  accepting mode of TCNE-HMB using classical reorganization energy  $\lambda_s = 1000 \text{ cm}^{-1}$ ,  $V = 4000 \text{ cm}^{-1}$  and  $T = 298 \text{ K}$ . For narrow distribution centered at  $n \sim 1$ ,  $\Delta G^0 = -.300 \text{ eV}$ . For broadest distribution centered at  $n \sim 3$ ,  $\Delta G^0 = 1.7 \text{ eV}$ .

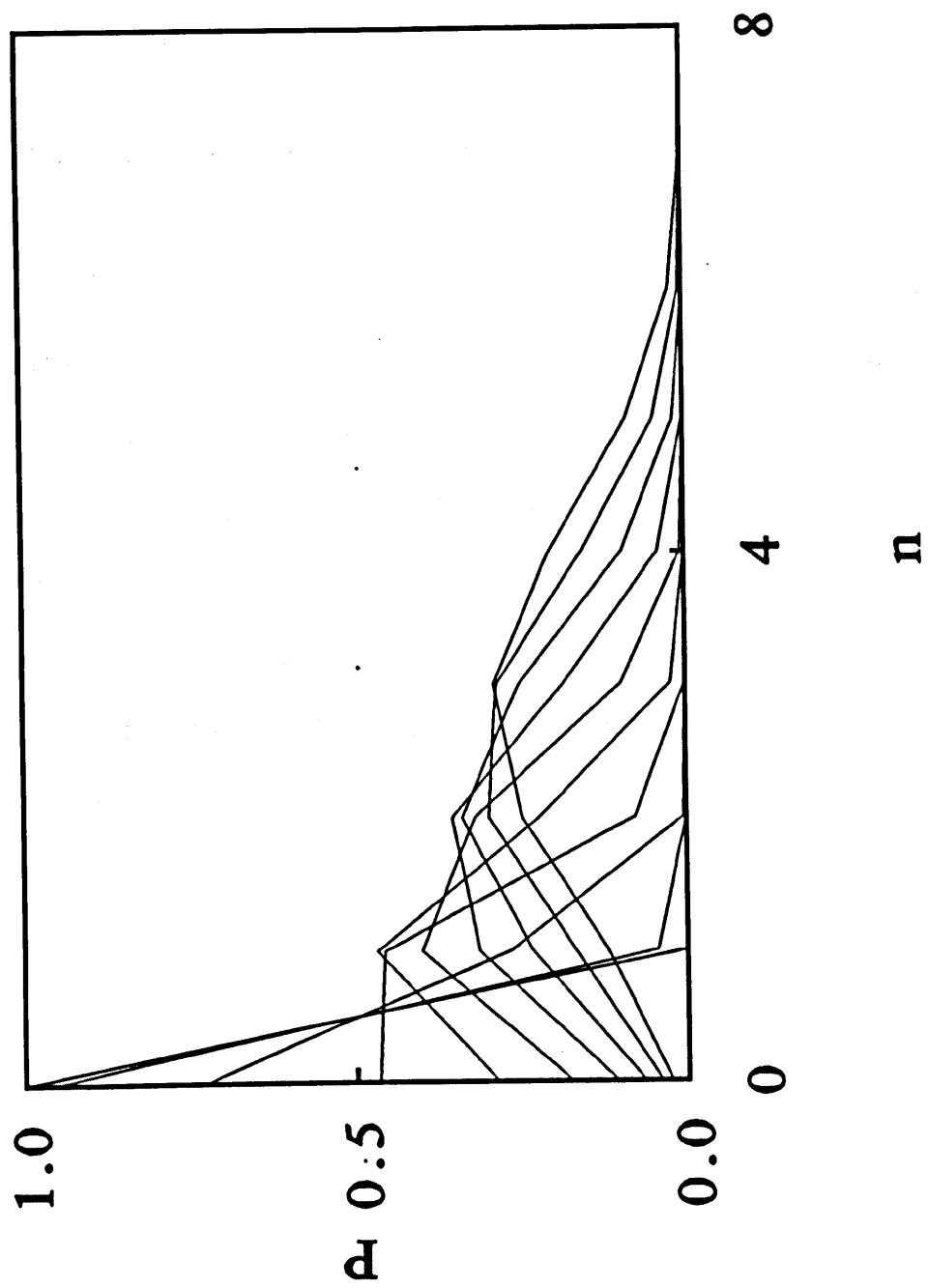


Figure IV.20 Average energy accepted by interior modes directly coupled to charge transfer in the TCNE-HMB complex plotted versus driving force. Calculation parameters: classical reorganization energy  $\lambda_s = 1000 \text{ cm}^{-1}$ ,  $V = 4000 \text{ cm}^{-1}$  and  $T = 298 \text{ K}$ . The most strongly coupled modes are indicated in figure. Note saturation of  $165 \text{ cm}^{-1}$  donor acceptor stretch at  $\Delta G^0 \sim 3000 \text{ cm}^{-1}$ . The strong decay of the Frank-Condon terms with increasing vibrational quantum number makes low frequency modes inefficient energy acceptors at large driving forces. Thus no photodissociation is observed even in this strongly coupled mode at driving forces of  $\sim 80$  quanta ( $\Delta G^0 / 165 \text{ cm}^{-1}$ ). At large driving forces, the high frequencies become the more efficient energy acceptors.

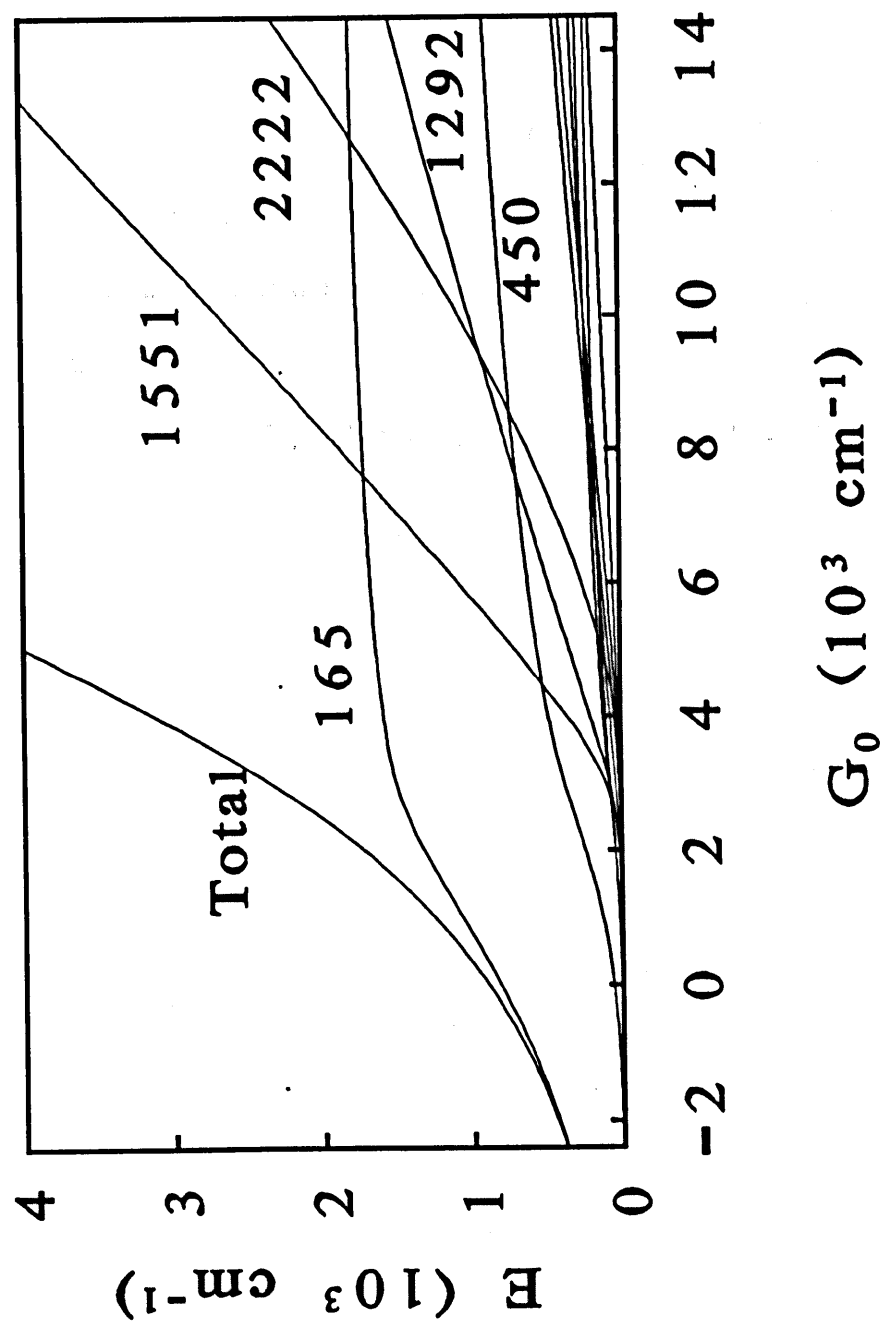


Table IV.1    Frequencies, shifts in dimensionless normal coordinates and reorganization energies of the vibrational modes active in the charge transfer band of TCNE-HMB in  $\text{CCl}_4$  as measured using resonance Raman excitation profiles and absorption spectra.

(F. Markel, N.S. Ferris, I.R. Gould, A.B. Myers, J. Am. Chem. Soc. **114**, 6208 (1992))

Freq. (cm <sup>-1</sup> ):	$\Delta$ :	$\lambda_1$ (cm <sup>-1</sup> ):
165	-3.80	1191
450	1.34	402
542	0.59	94
600	0.61	112
968	0.44	94
1292	0.73	344
1389	0.36	90
1437	0.23	38
1551	1.03	823
1570	0.30	71
2222	0.48	256

**Table IV.2** Experimental and theoretical results for the free energies and driving forces associated with the electron transfer in the molecular complex TCNE-HMB.

Solvent abbreviations: AcCN: acetonitrile, Acet: acetone, THF: tetrahydrofuran, MeOAc: methyl acetate, BuCN: butyronitrile, PC: propylene carbonate, EtOAc: ethyl acetate, NB: nitrobenzene, benzoCN: benzonitrile, GTA: glycerol triacetate, TCE: trichloroethene, CCl<sub>4</sub>: carbon tetrachloride

Solvent:	$\lambda_s$ (cm <sup>-1</sup> ): (Exp.)	$\lambda_s$ (cm <sup>-1</sup> ): (Theor.)	$\Delta G^0$ (10 <sup>3</sup> cm <sup>-1</sup> ): (Exp.)	$\Delta\Delta G^0$ (10 <sup>3</sup> cm <sup>-1</sup> ): (Exp.)	$\Delta\Delta G^0$ (10 <sup>3</sup> cm <sup>-1</sup> ): (Theor.)
AcCN	2000	1470	-12.50	1.36	1.09
Acet	1720	1380	-13.06	0.80	1.06
THF	1360	1040	-13.43	0.43	0.93
MeOAc	1540	1090	-13.15	0.71	0.90
BuCN	1730	1350	-12.87	0.99	1.06
PC	2190	1340	-12.39	1.47	1.11
EtOAc	1470	1020	-13.30	0.56	0.89
BenzoCN	1320	1090	-12.75	1.11	1.07
GTA	1420	980	-13.11	0.75	0.92
NB	1460	1070	-12.53	1.33	1.09
TCE	650	460	-13.21	0.65	0.70
CCl <sub>4</sub>	100	100	-13.86	0	0.51



Table IV.3 Experimental and theoretical charge recombination times in TCNE-HMB.  $\tau_{ET}$  is the experimental result,  $\tau_L$  is the longitudinal dielectric relaxation time,  $\tau_1$  is the ET time calculated assuming infinitely fast solvent relaxation,  $\tau_2$  is the ET time calculated with the solvent simulation (see text for details). Solvent abbreviations: AcCN: acetonitrile, Acet: acetone, THF: tetrahydrofuran, MeOAc: methyl acetate, BuCN: butyronitrile, PC: propylene carbonate, EtOAc: ethyl acetate, NB: nitrobenzene, benzoCN: benzonitrile, GTA: glycerol triacetate, TCE: trichloroethene,  $CCl_4$ : carbon tetrachloride

Solvent:	$\tau_{ET}$ (ps):	$\tau_L$ (ps):	$\tau_1$ (ps):	$\tau_2$ (ps):
AcCN	0.643(8)	0.56	0.18	0.76
Acet	0.995(6)	0.83	0.33	1.20
THF	2.13(2)	1.42	0.59	1.89
MeOAc	1.65(1)	1.66	0.41	1.75
BuCN	1.39(1)	1.7	0.29	1.57
PC	1.34(2)	2.4	0.15	1.56
EtOAc	2.28(1)	2.63	0.47	2.30
NB	2.82(3)	3.4	0.28	1.74
BenzoCN	2.76(2)	4.76	0.37	2.14
GTA	2.93(2)	125	0.44	6.68
TCE	3.20(7)	$\infty$	0.96	3.78
CCl <sub>4</sub>	11.2(1)	$\infty$	2.95	3.64

## CHAPTER V

### Photoinduced Electron Transfer in Porphyrin-Quinones

#### Introduction:

The efficient transduction of light energy to chemical potential energy as observed in many photosynthetic systems is achieved by the rapid execution of two fundamental molecular processes following the initial optical excitation: the transfer of this energy through the antenna complex to the primary electron donor, and the initial electron transfer which stores the excitation energy in dipolar form. The high yield of these processes as observed, for example, in natural systems, depends upon the rapidity of the reaction with respect to competitive relaxation mechanisms. As fluorescence from reactant electronic states often comprises the principal loss channel for electronic energy transfer or electron transfer reactions, it is necessary to complete these reactions quickly with respect to the fluorescent rate. Molecular properties and subsequent reaction dynamics which serve to accelerate the evolution of the system through productive reaction channels are thus of great interest. One such dynamic property of optically induced electronic energy transfer and charge separation reactions which has been the recent subject of numerous experimental [1-6] and theoretical [7-11] investigations is the role of nuclear and electronic coherences in these reactions.

The energy transfer through photosynthetic antenna complexes such as those found in phycobilisomes [12] and the initial charge separation in bacterial reaction centers [13] both occur on time scales over which both nuclear and electronic coherences have been demonstrated to persist in condensed phase systems. Vos and coworkers have reported oscillations of  $\sim 500$  fs and  $\sim 2$  ps in the transient stimulated emission signal accompanying the electron transfer in *Rhodobacter capsulatus* algae at 10 K [4]. This demonstrated coherence and the efficiency of the native processes naturally suggests a role of this coherence in transfer dynamics.

#### Coherences and Their Role in Reactions:

The phenomenological Bloch model has been successfully employed by many investigators to express the dynamics of an optically driven system coupled to a bath. It is convenient to employ this formalism to illustrate the role of coherence in a reaction such as electronic energy transfer. The energy transfer between coupled chromophores is expressed as a population difference equation  $\Delta n(t)$  which expresses the equilibration of the electronic excitation between the coupled moieties using the parameters  $T_1$ , the excitation lifetime,  $T_2'$ , the coherence time which describes the electronic coherence between the coupled chromophores, and  $\beta$ , the matrix element responsible for the energy transfer [2]. The equation of motion is analytically expressed

in three regimes:

(1) underdamped:  $2 \beta T_2' > 1$

$$\Delta n(t) = e^{-t(\frac{1}{T_1} + \frac{1}{T_2'})} \cos(\omega_{osc}t - b) \quad (1)$$

where

$$\omega_{osc} = \sqrt{4\beta^2 - \frac{1}{T_2'^2}} \quad (2)$$

(2) critically damped:  $2 \beta T_2' = 1$

$$\Delta n(t) = e^{-t(\frac{1}{T_1} + \frac{1}{T_2'})} (1 + t(\frac{1}{T_1} + \frac{1}{T_2'})) \quad (3)$$

and

(3) overdamped:  $2 \beta T_2' < 1$

$$\Delta n(t) = e^{(-\frac{t}{T_1})} \left[ (1+\kappa) e^{\frac{-t(1-\kappa)}{T_2'}} - (1-\kappa) e^{\frac{-t(1+\kappa)}{T_2'}} \right] \quad (4)$$

where

$$\kappa = \sqrt{1 - (2\beta T_2')^2} \quad (5)$$

The population transfer expression  $\Delta n(t)$  for the dynamics in the overdamped regime where  $(2 \beta T_2')^2 \ll 1$  further simplifies to:

$$\Delta n(t) = e^{-t(\frac{1}{T_1} + 2\beta^2 T_2')} \quad (6)$$

The effect of this electronic coherence is apparent in equation V. 6 as this expression shows the population equilibration rate between coupled chromophores is exponentially dependant upon the coherence time  $T_2'$ .

The effect of a coherence on a reaction such as electron transfer in the underdamped regime is conveniently examined in the context of the Landau-Zener transition probability formalism. As discussed in Chapter II of this thesis, the Landau-Zener transition probability describes an incoherent electronic transition between weakly coupled states in terms of, among other properties, the electronic coupling matrix element and the velocity of the reactive system through the transition configuration. This transition probability amplitude is enhanced via constructive interference under certain conditions.

The motion of a Langevinian system along a reaction coordinate is described by a stochastic process in which the reactive complex is subject to a frequency dependent but linear friction force and a Gaussian distributed random force. Here the energy loss rate is the power dissipated against the frictional force. This power is given by:

$$P = \zeta v^2 \quad (7)$$

where  $\zeta$  is the frequency dependent friction parameter and  $v$  is the system velocity which may be averaged over harmonic motion. The time required for the system to lose a given amount of energy is inversely proportional to the friction parameter,  $\zeta$ .

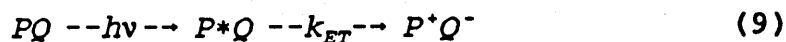
For a reacting system in which both the Landau-Zener transition probability  $P_{LZ}$  is  $\ll 1$  due to the nonadiabaticity of the transition and the energy loss rate of the system is low due to the weak coupling between the optical transition and the bath, there may be many crossings through the transition region. In the underdamped regime, when the coherence time  $T_2$  is long compared to the period of oscillation to the transition geometry, some of these crossings will occur coherently. For a self-exchange electron transfer reaction in which the above conditions are met, the resulting constructive interference enhances the Landau-Zener probability  $P_{LZ}$  such that [8]:

$$P_{COH} \approx 2P_{LZ} N_{COH}^2 \quad (8)$$

where  $N_{COH}$  is the number of coherent crossings through the transition region.

Detailed spectroscopic measurements on chemical systems which model the picosecond electron transfer dynamics observed in native systems are required both to elucidate these mechanisms in natural systems and to provide avenues for device development. In order to perform a systematic study on the role of coherences in a reaction such as an optically induced electron transfer, a molecular system is required

which undergoes electron transfer on the same time scale that coherences have been experimentally observed. The porphyrin based photosynthetic systems of both bacterial reaction centers and green plants naturally suggest the employment of a porphyrin-quinone electron transfer model system. This is an example of the indirect photoinduced electron transfer mechanism detailed in Chapter I of this thesis in which the electron transfer proceeds from a local excitation of the donor or acceptor. Here, the optical excitation photon serves to locally excite the porphyrin electron donor. Following this excitation, the electron is transferred to the quinone:



In reversible systems such as porphyrin-quinones the polar state  $P^+Q^-$  undergoes subsequent relaxation via charge recombination to return to the initial, neutral electronic state.

The transient absorption spectrum for both zinc and freebase covalently bound phenylporphyrin-quinone have recently been resolved at time delays of 1 ps [14]. The formation of the polar state  $P^+Q^-$  following the optical preparation of the locally excited state  $P^*Q$  was reported to occur within the 350 fs excitation. It is quite possible that coherences created by a sub 100 fs optical pulse in modes coupled to the electron transfer may persist during this reaction. In order to investigate the solution phase dynamics of the optical transition  $PQ \rightarrow P^*Q$ , time resolved spectroscopic experiments were performed on the non-charge transferring magnesium tetraphenylporphyrin in



tetrahydrofuran (MgTPP in THF) at ambient temperature.

#### Observed Coherences in Porphyrins and Porphyrin-Quinones:

One very basic coherence loss process involves the transition of an optically driven system from the Raman to the fluorescence regime [15]. It is well known that the spontaneous scattering collected in a resonant Raman experiment is emission from an electronically phased ensemble. As the electronic coherence of this system is damped, the superposition state decays to a fluorescent population which persists for the lifetime of the excited state. Therefore an experiment which observes the accompanying changes in the emission of the sample will measure the loss of electronic coherence. While the resonance Raman state is still imprinted on the system, the anisotropies associated with emission from the driven state are different than in the case of dephased fluorescence. This emission anisotropy therefore presents a novel way to access the coherence dynamics. A relationship between molecular state coherence and anisotropy in optical experiments was recently predicted [16].

The anisotropy of a signal field generated by a prepared state in a pump-probe experiment may be determined by probing the excitation with polarization both parallel and perpendicular to the pump pulse. In the experiments, the difference in the detector signals for the two polarizations,  $S_{\parallel}(t) - S_{\perp}(t)$ , normalized by the spatially integrated signal  $S_{\parallel}(t) + 2S_{\perp}(t)$ , is collected as a function of time delay between the state

preparation and the probing event. If a degeneracy or near degeneracy is accessed by the initial excitation, this excitation pulse places the ensemble in a superposition state. When a probe pulse couples the components of this superposition to a common final state, the probe signal contains interference terms described by constructive Feynman paths (see Figure V.1). It is the experimental observation of the decay of this interference that was reported by Galli, Wynne, LeCours, Therien and Hochstrasser in *Chemical Physics Letters*, 206, (1993), 493. This article presented a novel use of a pump-probe anisotropy measurement to observe, in a room temperature liquid, the electronic dephasing of degenerate states.

Figure V.2 presents the decay of the anisotropy of magnesium tetraphenylporphyrin in tetrahydrofuran when excited and probed at 620 nm (see Appendix I, this thesis and *Chemical Physics Letters*, 206, (1993), 493, for details). The biphasic decay of the anisotropy signal indicates the evolution of the initial fully coherent ensemble with anisotropy 0.7 to a partially coherent ensemble with anisotropy 0.4 to a dephased, populationally equilibrated ensemble of anisotropy 0.1. These anisotropy values and decays indicate the electronic dephasing and population equilibration of the  $Q_x$  and  $Q_y$  components of the  $E_u$  excited state. The anisotropy decays with time constants 210 fs and 1.6 ps. This experiment demonstrates the persistence of an electronic coherence in magnesium tetraphenylporphyrin in tetrahydrofuran over the time scale of the predicted electron transfer time for porphyrin-quinone.

Oscillatory components in transient absorption signals indicating a persistent coherence during the electron transfer event have also been observed in freebase and metallated porphyrin-quinones in solution. Figure V.3 shows the transient absorption of freebase triphenylporphyrin-quinone in toluene excited at 620 nm and probed at 500 nm (upper curve) and 510 nm (lower curve). Following the initial overshoot small recurrences observed at  $\sim 200$  fs (500 nm) and  $\sim 300$  fs (510 nm) suggest that coherence plays some role in the electron transfer. Longer lasting oscillations are observed when the freebase triphenylporphyrin-quinone in the slow solvent, glycerol triacetate, is excited at 620 nm and probed at 520 nm. Figure V.4 displays the transient absorption with large amplitude oscillation of  $\sim 95 \text{ cm}^{-1}$  persisting for  $\sim$  the first picosecond following the initial excitation.

Due to the small extinction coefficient of freebase triphenylporphyrin-quinone at available excitation wavelengths (  $\epsilon$  (620 nm)  $\sim 400 \text{ L / mol cm}$  ) and resulting low level of excitation, the time required to attain an acceptable signal-to-noise value in spectroscopic examinations of this molecular system was prohibitive. In order to continue the investigation of the role of coherence in electron transfer reactions, numerous metallations, substituent groups, and solvents were examined in order to attain both an adequate extinction coefficient at 620 nm and red edge excitation. Both characteristics were obtained with magnesium triphenylporphyrin-quinone (5, 10, 15 - triphenyl-20-(2', 5'-quinonyl) porphinato (Mg) ) in toluene, tetrahydrofuran, and pyridine.

### Description of System and Expectations:

The optical and near ultraviolet spectrum of a regular metalloporphyrin is adequately described by the excitation of a  $\pi$  electron from one of two HOMOs of  $a_{1u}$  or  $a_{2u}$  symmetry to the doubly degenerate  $e_g$  LUMO ( $D_{4h}$  notation) [17]. Two electron coupling matrix elements describe the transition mixing which gives rise to the intense absorption observed around 420 nm known as the Soret (B) band and the weaker features observed in the 500 to 600 nm region referred to as the Q bands. For a porphyrin with a fourfold symmetry axis such as MgTPP, two bands comprise the Q transition - the lower energy  $Q_0$ , and approximately  $1250\text{ cm}^{-1}$  to the blue, the vibronic band  $Q_v$ . When the fourfold symmetry is broken as in the freebase porphyrin, the  $Q_0$  state splits into the  $Q_x$  and  $Q_y$  components.

The ground state absorption spectra of magnesium triphenylporphyrin-quinone in solution is dominated by the excitation of the local porphyrin states as detailed above; the presence of the quinone serves as a small perturbation save for the addition of the broad charge transfer feature observable beneath and to the red of the porphyrin  $Q_0$  and  $Q_v$  vibronic bands. The position, width and magnitude of this band is solvent dependent.

Magnesium triphenylporphyrin-quinone in these solvents thus provides a molecular system for the examination of the role of coherence in photoinduced electron transfer. The relaxations which may be expected to contribute to the reaction dynamics

are the electronic dephasing and population equilibration of the  $Q_x$  and  $Q_y$  components of the  $E_u$  excited state of the porphyrin moiety as observed in MgTPP in tetrahydrofuran. As these components of the porphyrin excited state are expected to have different electronic coupling strengths with the ionic state  $P^+Q^-$ , it may also be possible to experimentally resolve the different electron transfer rates from the  $Q_x$  and  $Q_y$  levels.

### Results and Discussion:

The diffuse nature of the  $P^*$  absorption spectrum in the range 600-850 nm is well known to be present on a picosecond timescale for a variety of metallated and freebase porphyrins in various solvents [18]. The transient absorption in this spectral region at a delay of 20 ps is essentially flat save for two stimulated emission features. These stimulated emission peaks correspond to the vibronic bands observable in the steady state fluorescence spectrum; in zinc tetraphenylporphyrin, for example, the bands occur at 575 and 625 nm; in freebase tetraphenylporphyrin these emissions occur at 675 and 700 nm.

As mentioned above, the 620 nm pulse excites the porphyrin-quinone in pyridine and tetrahydrofuran to both the  $P^*$  state and the charge transfer (CT)  $P^+Q^-$  state. Following the photoexcitation of the porphyrin-quinone the  $P^*$  state rapidly evolves to the ionic  $P^+Q^-$  surface as the electron transfers to the quinone moiety on a

subpicosecond timescale. The porphyrin cation  $P^+$  absorption in the visible region is dominated by a  $\sim 50$  nm wide feature centered at  $\sim 650$  nm for the metallated species [14, 19]. Probing the system at 650 nm with sufficient time resolution will thus reveal the kinetics of the ion pair formation. Oscillatory components in the probe signal may indicate coherences maintained during this electron transfer reaction.

Figures V.5 and V.6 show the first  $\sim 1.5$  ps of electron transfer dynamics of magnesium triphenylporphyrin-quinone in pyridine at a temporal resolution of  $\sim 60$  fs. Both parallel and perpendicular probe components were collected (see Chapter III, this thesis) then combined to form the magic angle data presented. All data presented in this Chapter V are constructed magic angle data. The signal is fitted with an instantaneously rising component due to direct excitation to the ionic state which subsequently decays with a charge recombination time constant of  $735 \pm 65$  fs as the system returns to the ground electronic state. As expected, the signal also contains a component which grows in at the electron transfer rate of  $390 \pm 54$  fs, then decays with the charge recombination time. There is no evidence of any oscillatory signal component. Neither is there any evidence of multiple electron transfer rates indicating population transfer between the  $Q_x$  and  $Q_y$  components of  $P^+$  as observed in MgTPP in tetrahydrofuran and detailed above nor electron transfer occurring directly from these components with different rates due to differential coupling. Vibrational relaxation in the ground electronic state following the charge recombination is observable in the long time dynamics data. Figure V.7 shows the magic angle data

resulting from the 620 nm excitation, 620 nm probe examination. Following the initial transient absorption event a transient bleach is observed which decays on a  $> 10$  ps time scale as the porphyrin-quinone cools to the initial state.

Similar observations are made in the examination of the electron transfer dynamics of magnesium porphyrin-quinone in tetrahydrofuran. Again, no oscillatory signal component is observed. The long time dynamic data presented in Figure V.10 was also fit using two functions: one with an instantaneous rise, charge recombination decay, and cooling decay, the other with an electron transfer rise, charge recombination decay, and cooling decay. Both the excitation and probe pulses were centered at 620 nm. Figures V.8 and V. 9 display the short time magic angle kinetic data obtained using a 650 nm probe pulse following the 620 nm excitation. The electron transfer rate resulting from this model is  $350 \pm 10$  fs, the charge recombination  $1340 \pm 20$  fs; these components are again accompanied by a  $> 10$  ps cooling component.

In toluene the broad, ground state charge transfer feature is centered  $\sim 680$  nm, while the relatively narrow  $Q_0$  transition to  $P^*$  is centered  $\sim 600$  nm. As a result the excitation of the magnesium porphyrin-quinone at 620 nm is dominated by:



prohibiting the observation of the  $P^* \rightarrow P^+Q^-$  electron transfer. Figures V.11 and V.12 show the transient absorption of magnesium porphyrin-quinone in toluene. The fitting function rises instantaneously as a result of direct excitation to the ionic state, then decays with a charge recombination time of  $570 \pm 80$  fs and cooling component of 6

$\pm 0.08$  ps.

This investigation of electron transfer dynamics in magnesium porphyrin-quinone was successful with respect to the acquisition of high signal to noise data with sufficient temporal resolution to observe electron transfer events on the order of several hundreds of femtoseconds. Although high quality data on this photoinitiated system was obtained as planned, no oscillatory signal components indicating coherences maintained during the electron transfer were observed. Nor was it necessary to include population transfer kinetics between the  $Q_x$  and  $Q_y$  components of the  $E_u$  state as observed in MgTPP in tetrahydrofuran and discussed above. Excellent fits to the experimental data were obtained with the simplest model: instantaneous photoexcitation of the porphyrin to the local state  $P^*$  followed by the sub picosecond electron transfer as the system moves to the ionic surface  $P^+Q^-$  followed by charge recombination to the ground electronic state and picosecond cooling.

The anisotropy as a function of delay between pump and probe for magnesium porphyrin-quinone in pyridine, tetrahydrofuran and toluene displays no evidence of the electronic coherence observed for MgTPP in tetrahydrofuran. This may indicate that the destruction of the  $D_{4h}$  symmetry of MgTPP resulting from the replacement of the phenyl moiety by a quinone in the magnesium porphyrin-quinone may be sufficient to prohibit the superposition excitation of the  $Q_x$  and  $Q_y$  components. The  $Q_0$  vibronic band of the porphyrin  $P \rightarrow P^*$  transition displays a  $\sim 90$   $\text{cm}^{-1}$  shift in toluene when a phenyl is replaced by a quinone indicating a perturbation of the local states of the



porphyrin.

The kinetic data obtained for the electron transfer processes showed no evidence of the population transfer observed for MgTPP in tetrahydrofuran. In addition to the previously discussed possibility of  $Q_x$  and  $Q_y$  splitting, it may be that the perturbation of the quinone moiety on the local states of the porphyrin serves to differentiate the oscillator strengths of the  $Q_x$  and  $Q_y$  components. If the photoexcitation of the  $P \rightarrow P^*$  is dominated by a single component, the population transfer observed in MgTPP may be quenched by electron transfer in the magnesium porphyrin-quinone.

## Chapter V

### References:

- 1 K.Wynne, C.Galli, P.J.F.DeRege, M.J.Therien, and R.M.Hochstrasser,  
*Ultrafast Phenomena VIII*, eds. J.L.Martin, A.Migus, G.A.Mourou,  
A.H.Zewail, (Springer-Verlag Berlin Heidelberg), (1993), 71
- 2 F. Zhu, C. Galli and R.M. Hochstrasser, *J. Chem. Phys.*, **98**, (1993), 1042.
- 3 C.Galli, K.Wynne, S.M. LeCours, M.J.Therien, and R.M.Hochstrasser,  
*Chem. Phys. Lett.*, **206**, (1993), 493
- 4 M.H.Vos, J.C.Lambry, S.J.Robles, D.C.Youvan, J.Breton, and J.L.Martin,  
*Proc. Natl. Acad. Sci. USA*, **88**, (1991), 8885
- 5 U.Banin, A.Waldman, and S.Ruhman, in  
*Ultrafast Phenomena VIII*, eds. J.L.Martin, A.Migus, G.A.Mourou,  
A.H.Zewail, (Springer-Verlag Berlin Heidelberg), (1993), 68
- 6 U. Banin, A. Waldman and S. Ruhman, *J. Chem. Phys.*, **96**, (1992), 2416
- 7 J.Jean, G.R.Fleming, and R.A.Friesner,  
*Ber. Bunsenges. Phys. Chem.*, **95**, (1991), 253
- 8 J.N.Onuchic and P.G.Wolynes, *J. Chem. Phys.*, **92**, (1988), 6495
- 9 R.A.Marcus and R.Almeida, *J. Phys. Chem.*, **94**, (1990), 2973
- 10 R.Almeida and R.A.Marcus, *J. Phys. Chem.*, **94**, (1990), 2978

- 11 R.S. Knox and D. Gülen, *Photochem. Photobiol.* , **57**, (1993), 40.
- 12 L.O.Palsson, T.Gillbro, A.Sharkov, R.Fischer, and H.Scheer,  
*Ultrafast Phenomena VIII*, eds. J.L.Martin, A.Migus, G.A.Mourou,  
A.H.Zewail, (Springer-Verlag Berlin Heidelberg), (1993), 557
- 13 W.Zinth, C.Lauterwasser, U.Finkele, P.Hamm, S.Schmidt, and W.Kaiser  
*Ultrafast Phenomena VIII*, eds. J.L.Martin, A.Migus, G.A.Mourou,  
A.H.Zewail, (Springer-Verlag Berlin Heidelberg) , (1993), 535
- 14 J.Rodriguez, C.Kirmaier, M.R.Johnson, R.A.Friesner, D.Holten, and  
J.L.Sessler, *J. Am. Chem. Soc.*, **113**, (1991), 1652
- 15 J. Friedman, F. Novak and R.M. Hochstrasser, in  
*Laser and Coherence Spectroscopy*, ed. J.I. Steinfeld  
(Plenum Press, New York 1978)  
R. M. Hochstrasser and F. A. Novak, *Chem. Phys. Lett.*, **53** (1978), 3;  
S. Mukamel, D. Grimbirt and Y. Rabin, *Phys. Rev. A*, **26**, (1982), 341;  
B. Dick and R.M. Hochstrasser, *J. Chem. Phys.*, **81**, (1984), 2897.
- 16 K.Wynne and R.M.Hochstrasser, *Chem. Phys.*, **171**, (1993), 179
- 17 M. Gouterman, in: *The Porphyrins*, vol. III, ed. D. Dolphin  
(Academic Press, New York, 1978), p.1
- 18 J. Rodriguez, C. Kirmaier and D. Holten,  
*J. Am. Chem. Soc.*, **111**, (1989), 6500.

- 19 Z.Gasyna, W.R.Browett, and M.J.Stillman,  
*Inorganic Chemistry*, **24**, (1985), 2441

**Figure V.1** Three-level diagram of the relevant states in the experiment in MgTPP in THF. The pump prepares a coherent superposition comprised by the components of the degenerate E state. The probe stimulates emission back to the ground electronic state. These processes are indicated by the solid arrows.

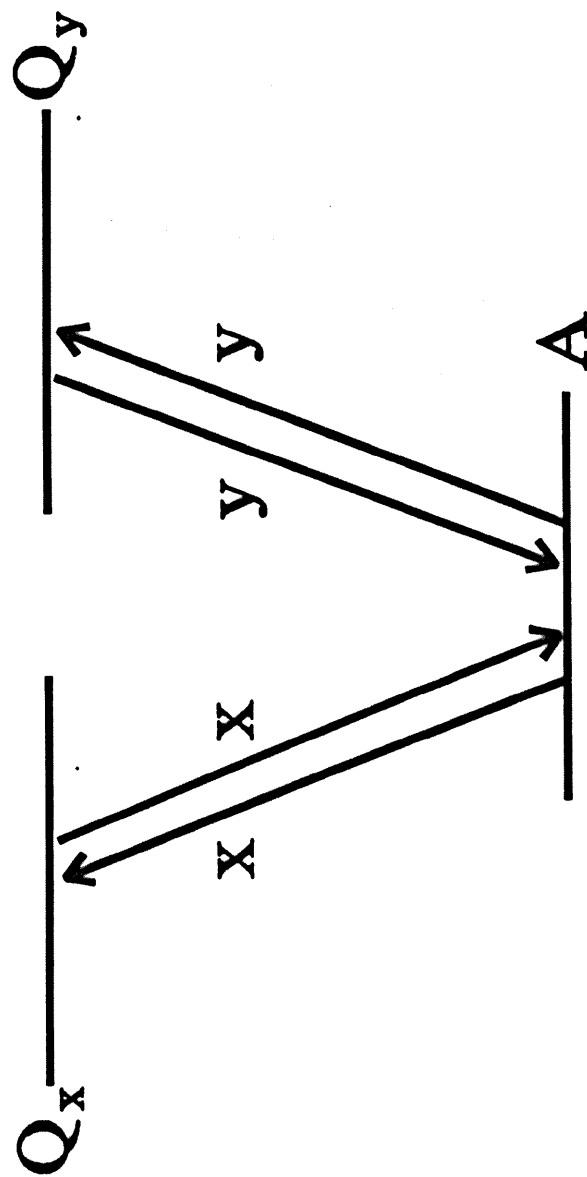


**Figure V.2** Pump-probe transient gain signal in MgTPP in THF pumped and probed at 620 nm with concurrent detection of the  $S_{||}(t)$  and  $S_{\perp}(t)$  gain signals. The open circles display the anisotropy calculated directly from the data while the solid line displays the anisotropy calculated from the fit (solid line). The inset shows the anisotropy calculated directly from experimental data taken with a smaller delay step size.

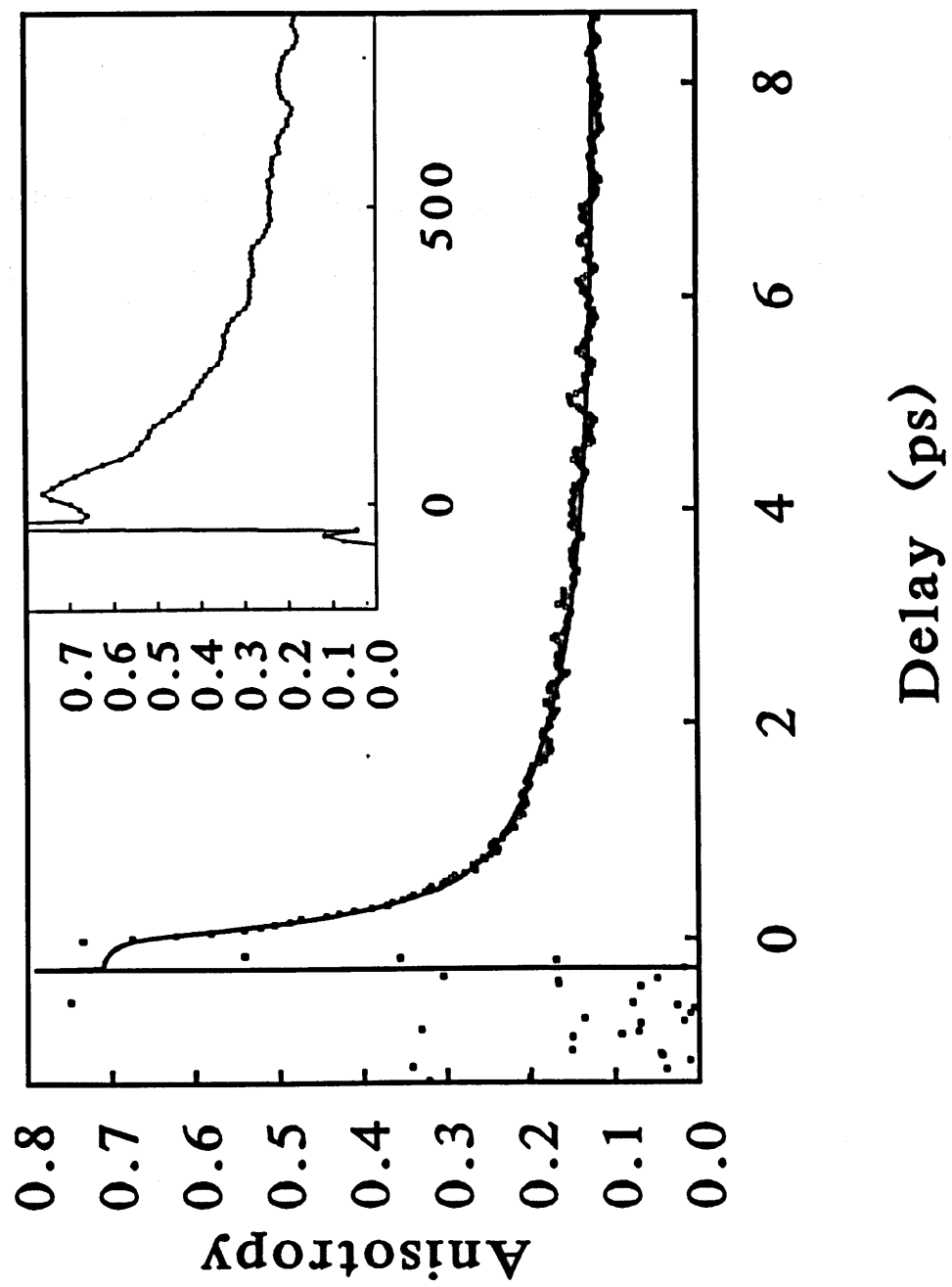




**Figure V.3** Transient absorption of freebase porphyrin-quinone in glycerol triacetate. The excitation wavelength is 620 nm, the probe wavelengths are 500 nm (upper curve) and 510 nm (lower curve). Solid arrows indicate features discussed in text.

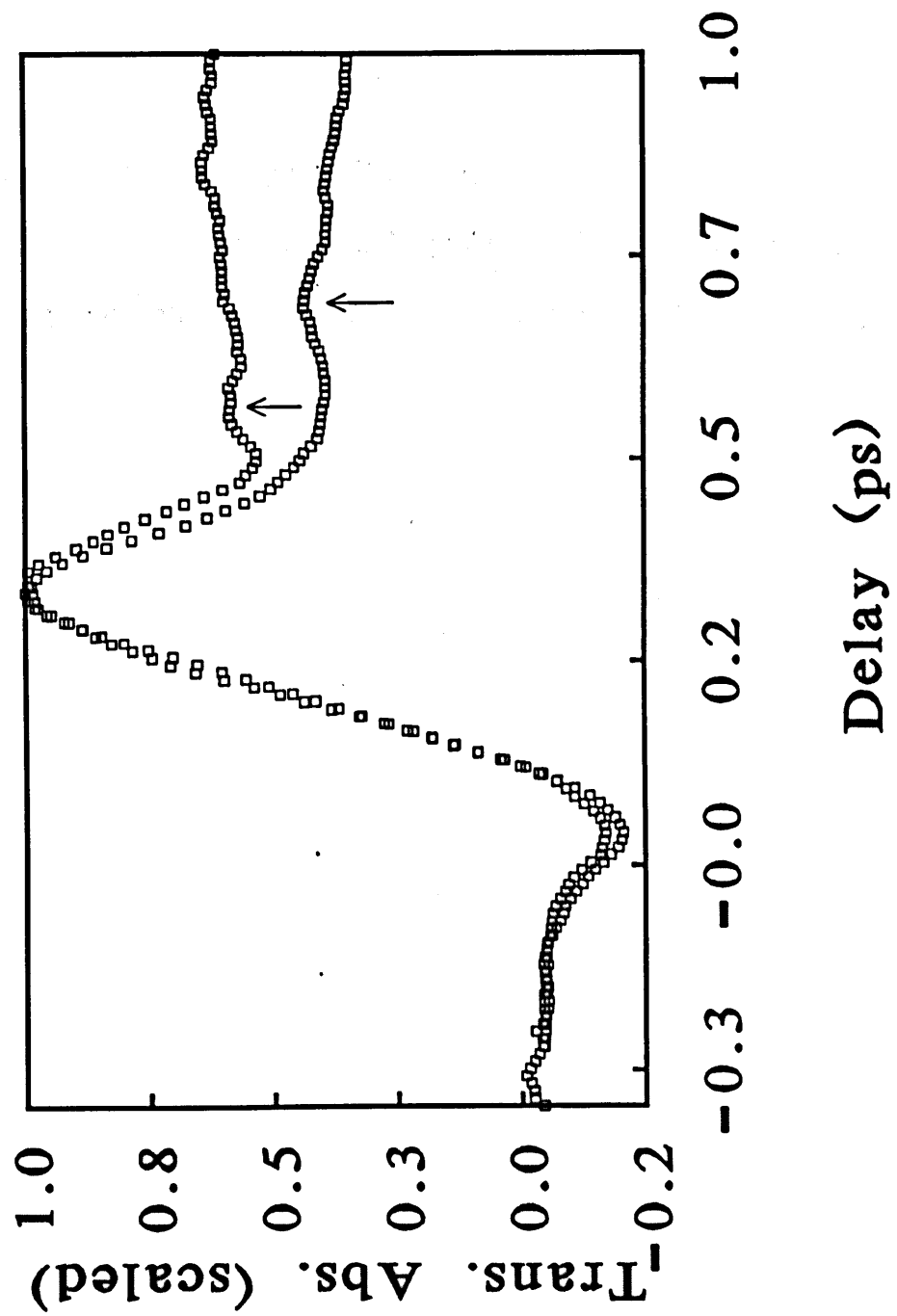


**Figure V.4** Transient absorption of freebase porphyrin-quinone in glycerol triacetate. The excitation wavelength is 620 nm, the probe wavelength is 520 nm. Open circles are the data points, solid line is the fit described in the text. The oscillation period is  $95 \text{ cm}^{-1}$ .

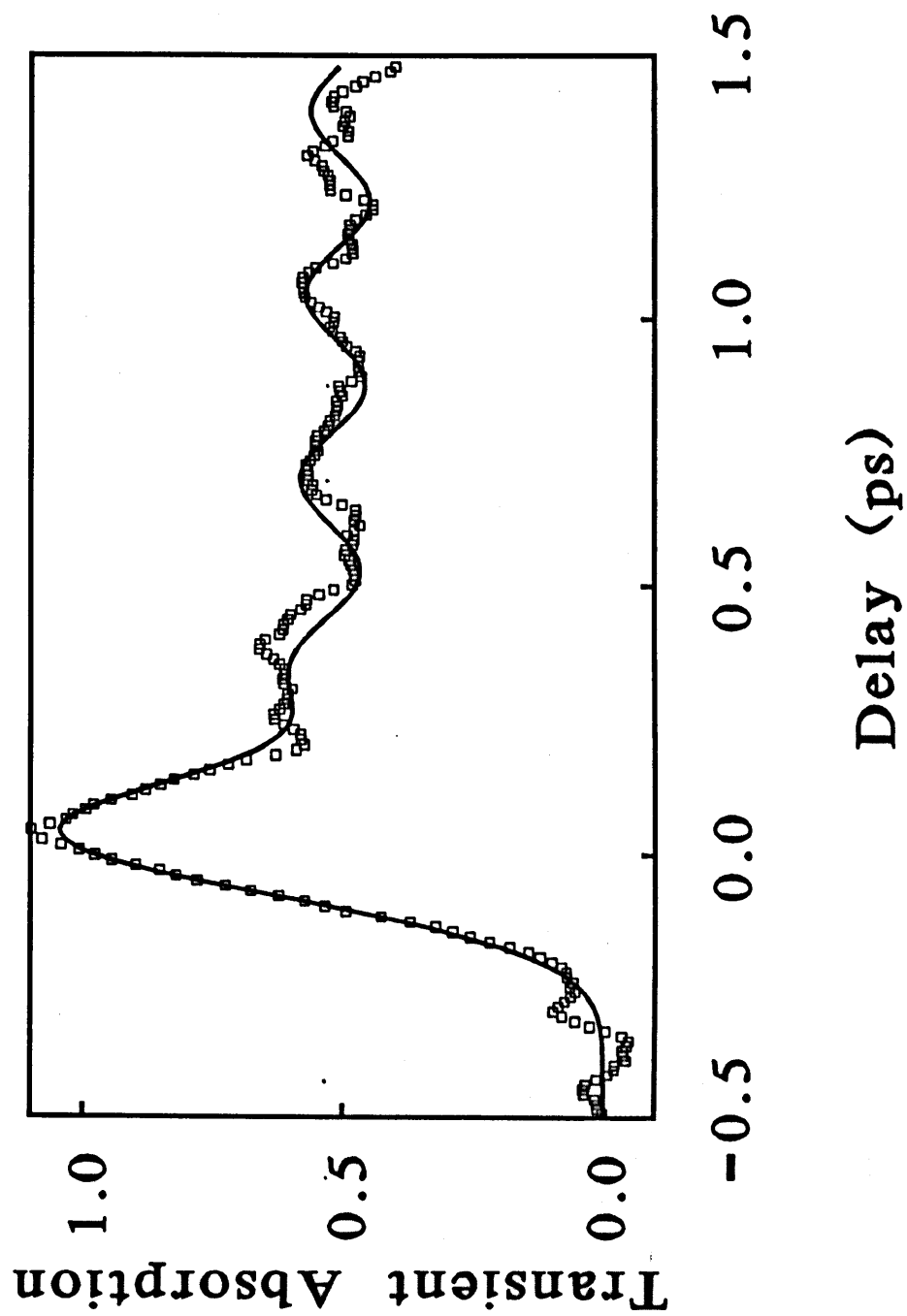


**Figure V.5** Transient absorption of magnesium triphenylporphyrin-quinone in pyridine. The excitation wavelength is 620 nm, the probe wavelength is 650 nm. Open circles are the data points, solid line is the fit described in the text.

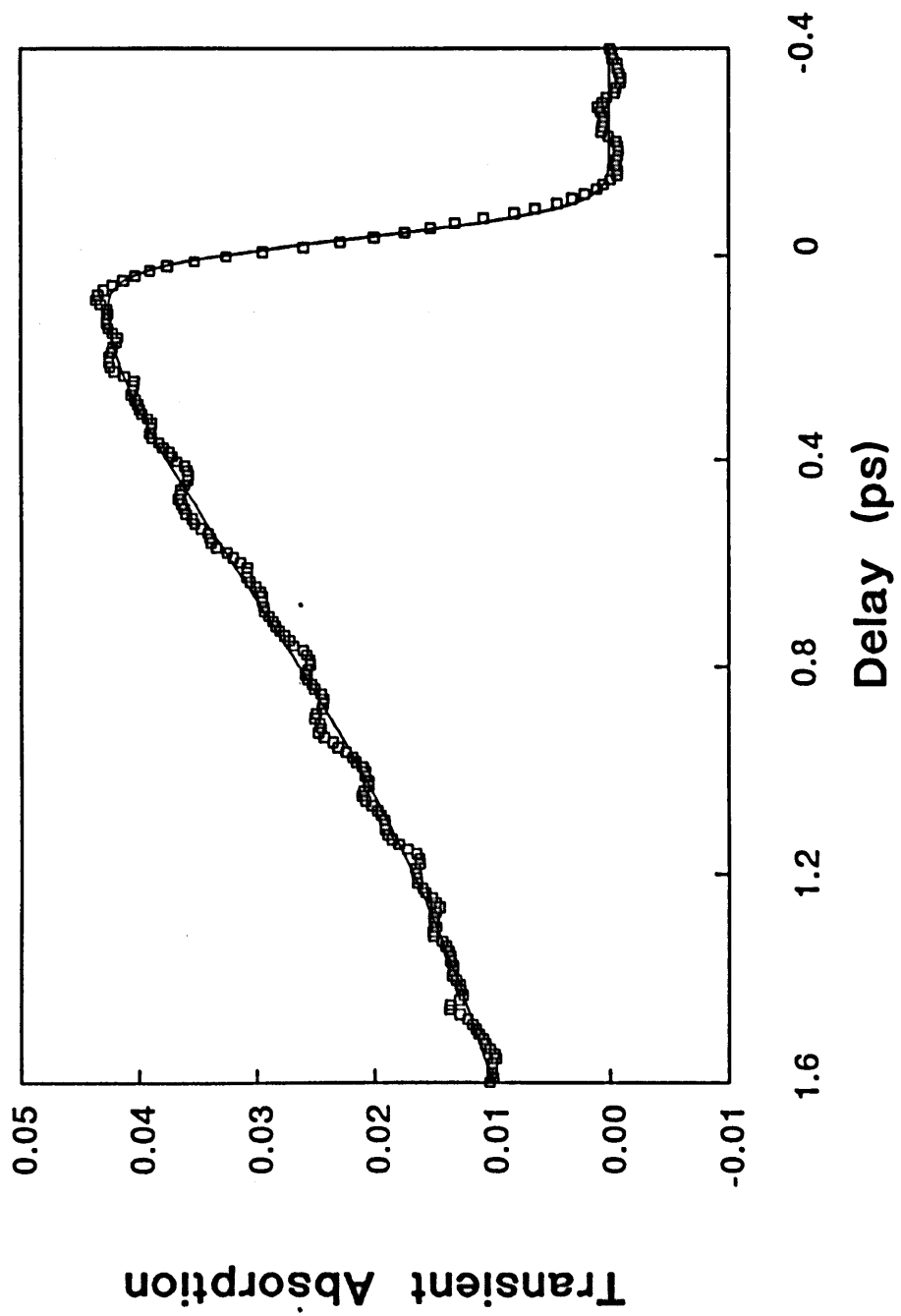


**Figure V.6** Transient absorption of magnesium triphenylporphyrin-quinone in pyridine. The excitation wavelength is 620 nm, the probe wavelength is 650 nm. Open circles are the data points, solid line is the fit described in the text.

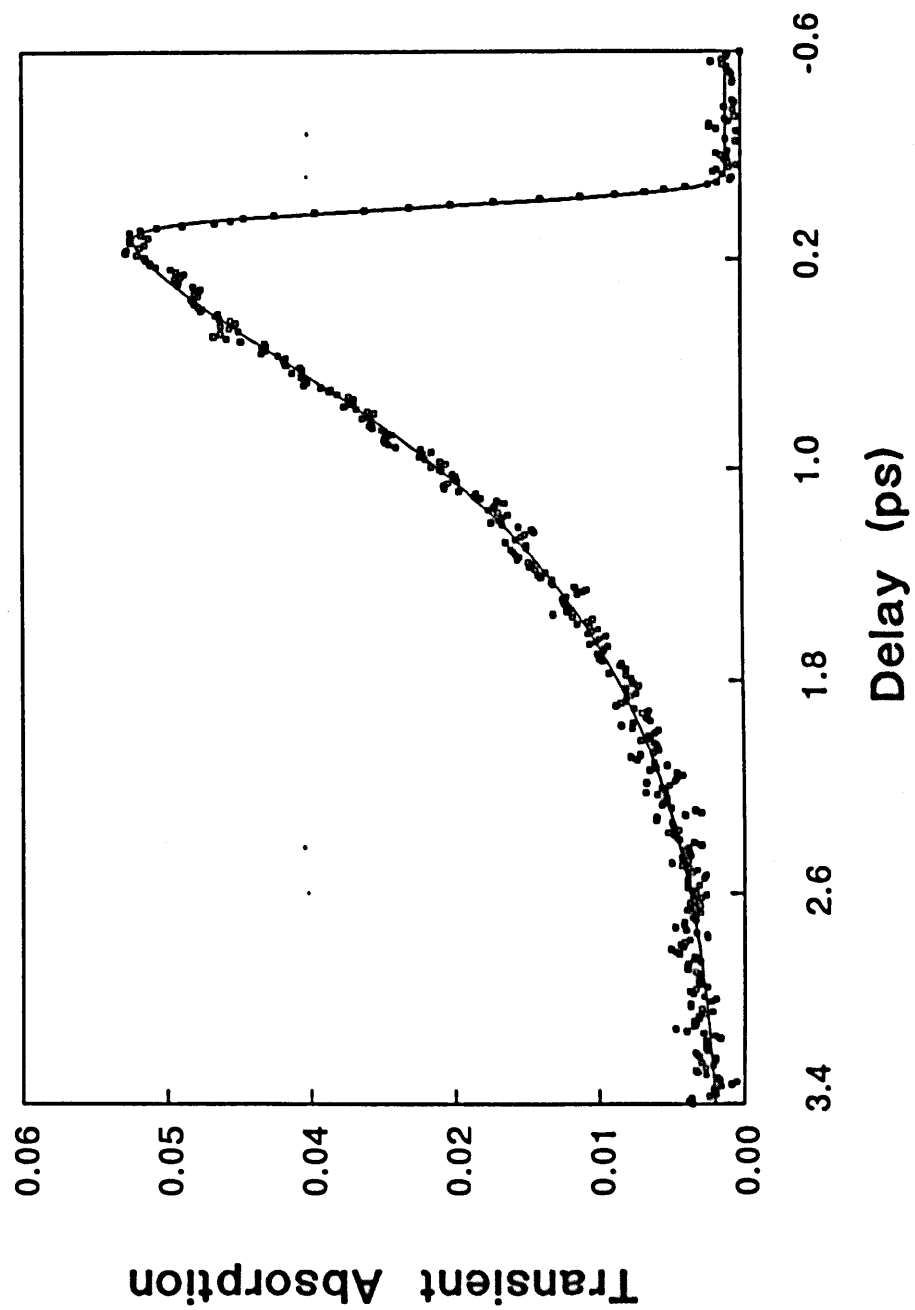




Figure V.7 Transient absorption of magnesium triphenylporphyrin-quinone in pyridine displaying the long time relaxation dynamics. Note the transient bleach following the decay of the ion absorption. The excitation wavelength is 620 nm, the probe wavelength is 620 nm. Open circles are the data points, solid line is the fit described in the text.

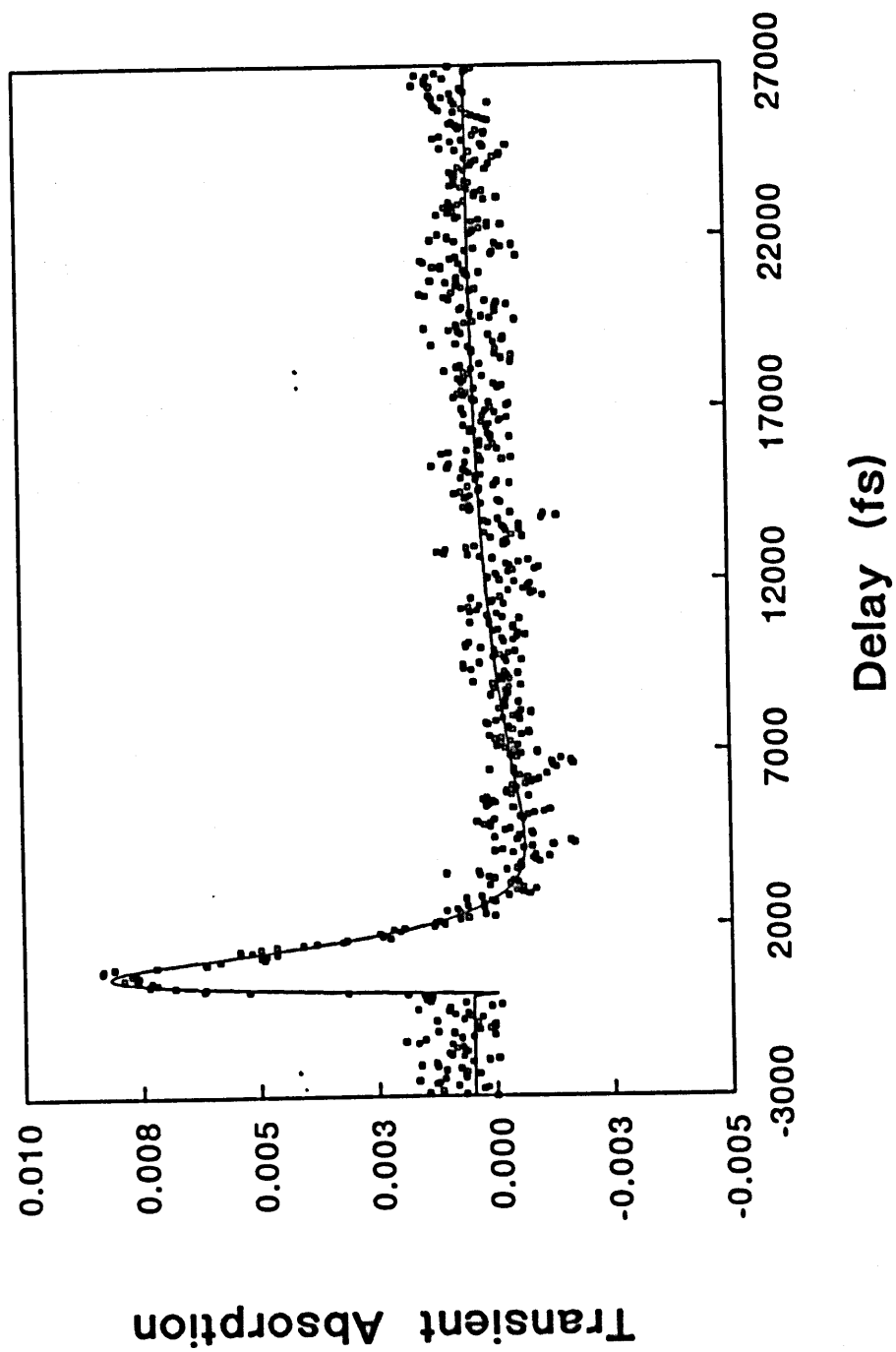
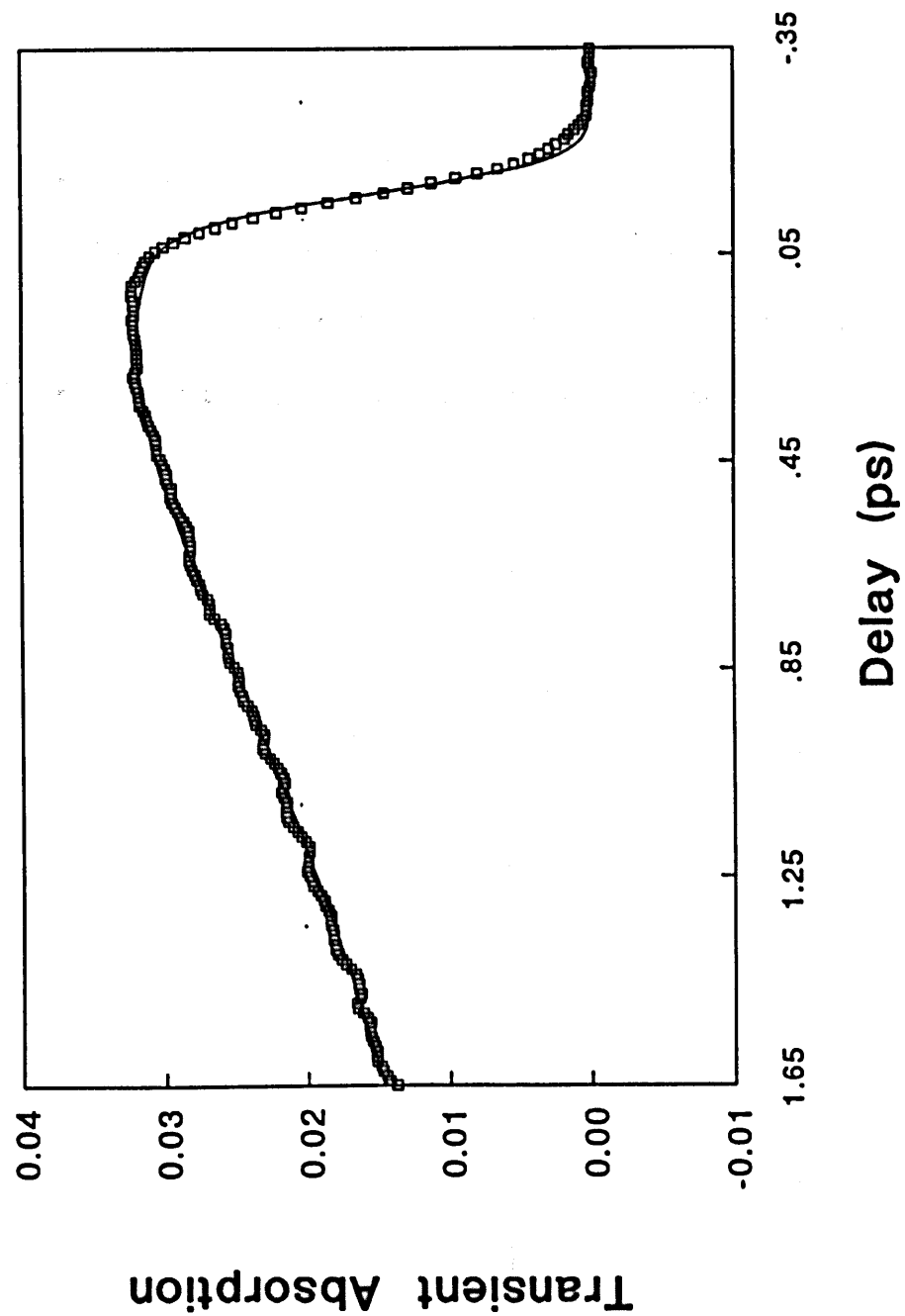
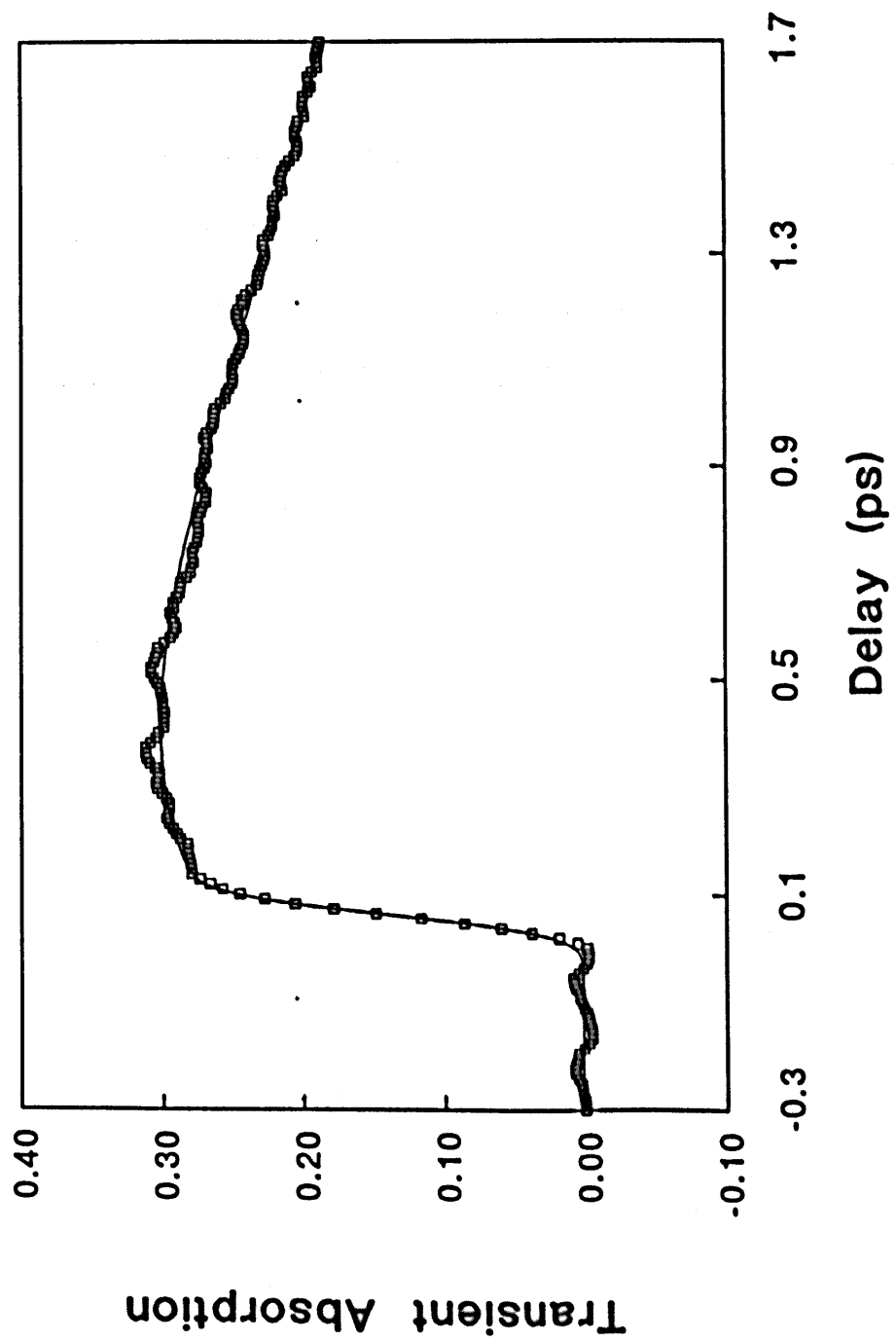


Figure V.8 Transient absorption of magnesium triphenylporphyrin-quinone in tetrahydrofuran displaying the rapid evolution of the system to the ionic state  $P^+Q^-$  and the charge recombination to the ground electronic state PQ. The excitation wavelength is 620 nm, the probe wavelength is 650 nm. Open circles are the data points, solid line is the fit described in the text.



**Figure V.9** Transient absorption of magnesium triphenylporphyrin-quinone in tetrahydrofuran. The excitation wavelength is 620 nm, the probe wavelength is 650 nm. The absorption grows in at the electron transfer rate and decays at the charge recombination rate. Open circles are the data points, solid line is the fit described in the text.



**Figure V.10** Transient absorption of magnesium triphenylporphyrin-quinone in tetrahydrofuran displaying the long time dynamics of charge recombination and ground state cooling. The excitation wavelength is 620 nm, the probe wavelength is 620 nm. Open circles are the data points, solid line is the fit described in the text.

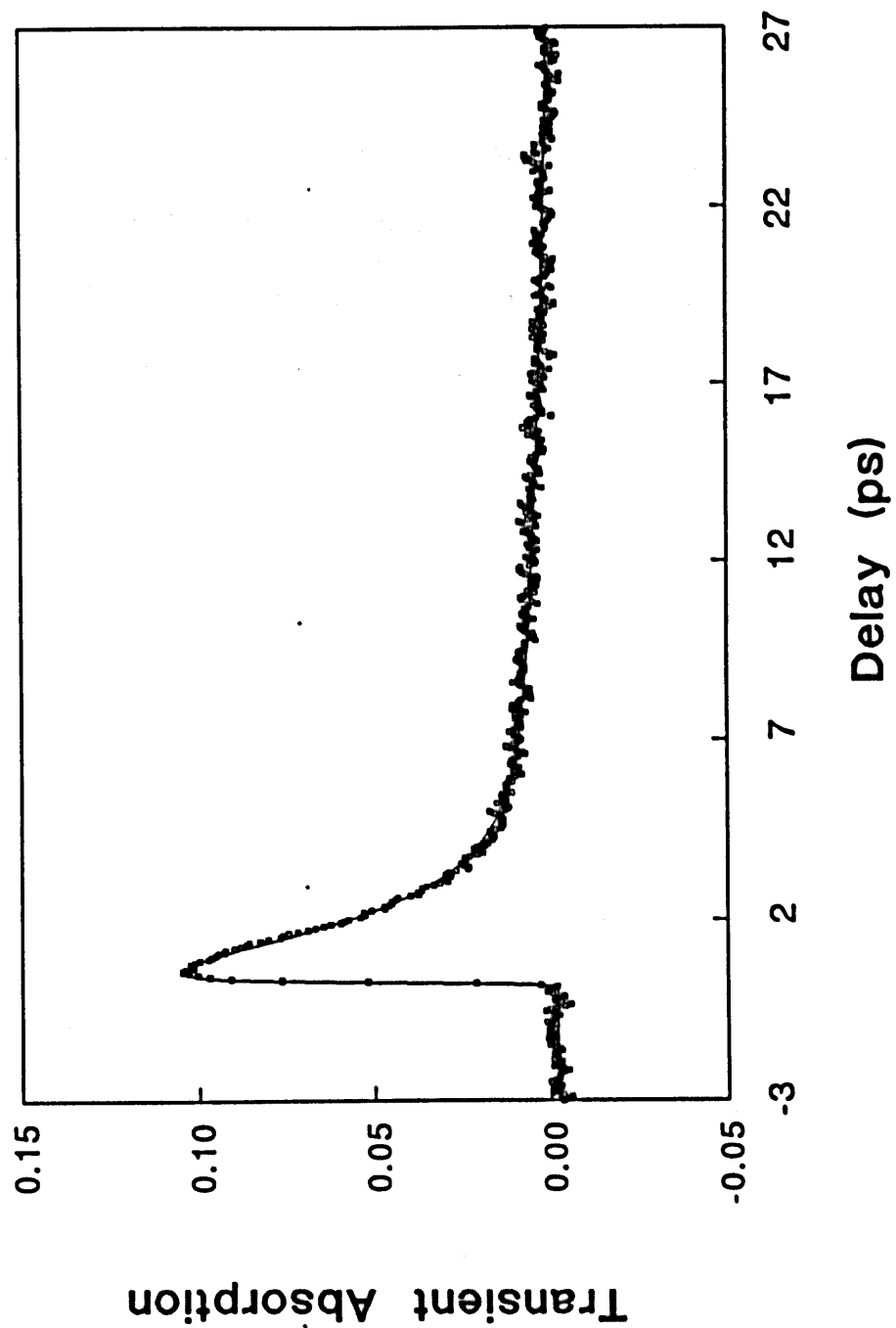




Figure V.11 Transient absorption of magnesium triphenylporphyrin-quinone in toluene displaying the long time dynamics of charge recombination and ground state cooling. The excitation wavelength is 620 nm, the probe wavelength is 620 nm. Open circles are the data points, solid line is the fit described in the text.

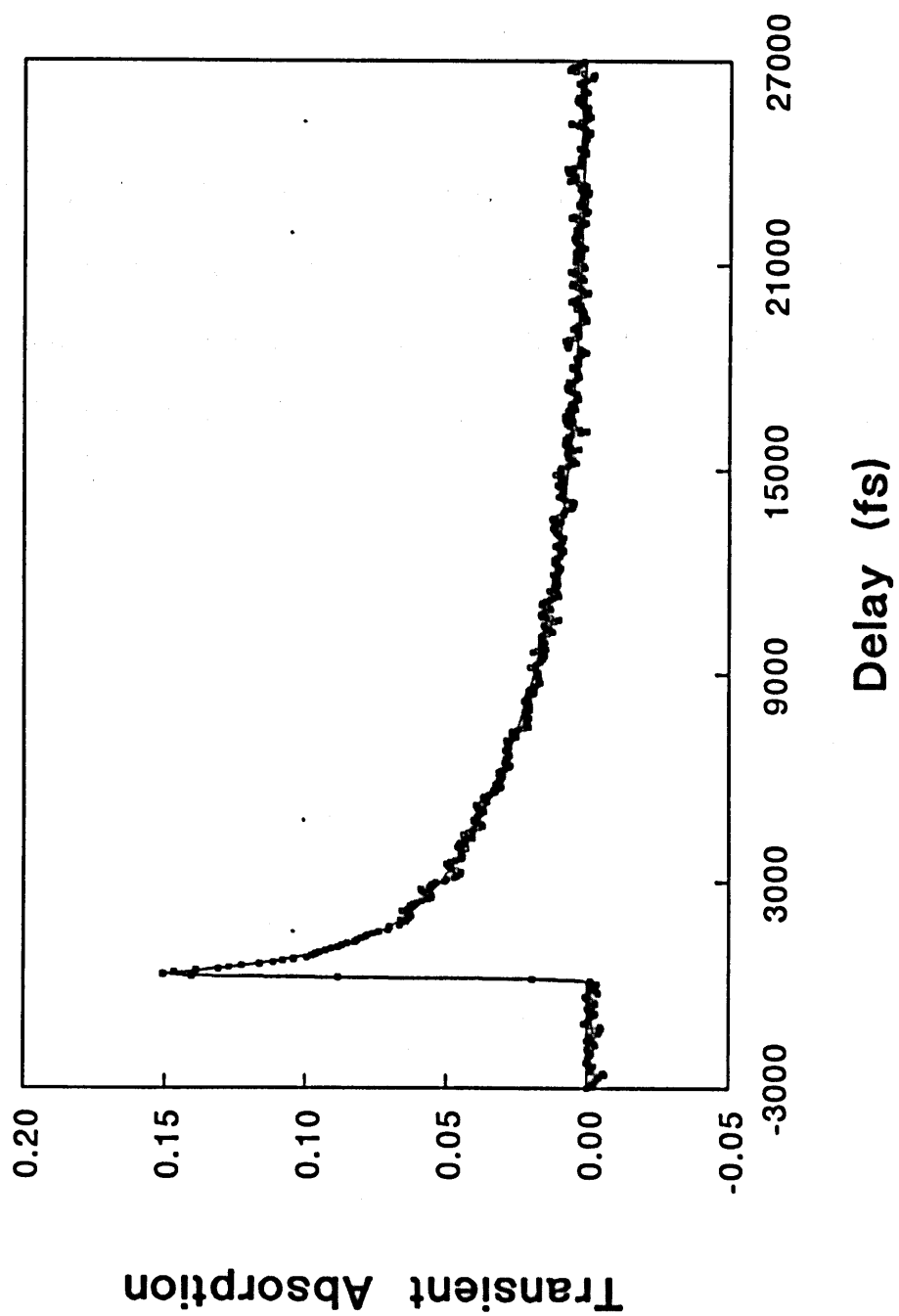
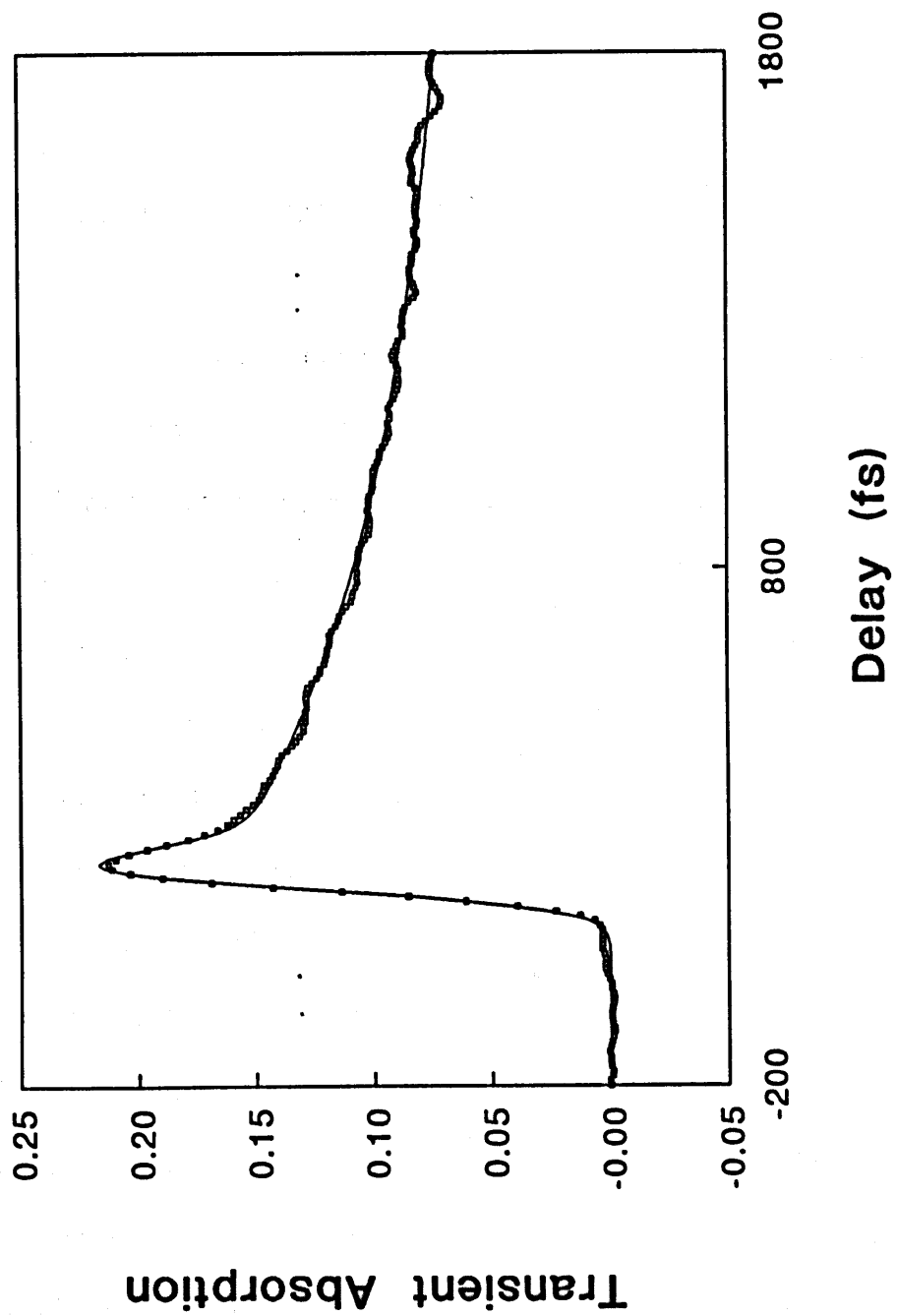


Figure V.12 Transient absorption of magnesium triphenylporphyrin-quinone in toluene displaying the short time dynamics of charge recombination. The excitation wavelength is 620 nm, the probe wavelength is 620 nm. Open circles are the data points, solid line is the fit described in the text.



## APPENDIX I

### Nondissertation Research

University of Pennsylvania (1988-1993)

#### Summary

##### I ) Coherence and electronic energy transfer

The dynamical behavior of intramolecular energy transfer in 9,9'-bifluorene and 2,2'-binaphthyl was investigated as a function of solvent environment in an examination of the solvent dependent system-bath coupling and the effect of this coupling on the electronic excitation transfer dynamics. Following an impulsive electronic excitation, the real time evolution of the system from a coherent, ordered system to an incoherent, disordered system was observed using transient polarization spectroscopy. This use of anisotropy measurements allows examination of orientational dynamics following the optical state preparation.

The excitation transfer between the fluorenyl moieties of 9,9'-bifluorene occurs in  $\sim 300$  fs in hexane and shows negligible variation in the alkane solvent series hexane - decane - hexadecane. In  $\text{CCL}_4$ , however, the excitation transfer slows appreciably to  $\sim 970$  fs. The excitation transfer between the naphthyl moieties of 2,2'-binaphthyl in  $\text{CCL}_4$  displays an underdamped oscillation of period  $1.2 \pm 0.1$  ps with damping constant  $180 \pm 20$  fs. This underdamped oscillatory motion results from the coherent

transport of the exciton. To my knowledge, this was the first observation of such coherence.

The observed dynamics were analyzed in the context of correlated energy fluctuations of the aryl moieties (global perturbations) which maintain the phase relationship between the excited ring states while destroying the ground to excited ring state coherence. This analysis made possible the experimental determination of both the excitation transfer rates and the solvent dependent pure dephasing rates responsible for loss of phase coherence of the initially prepared coherent state of the exciton. This analysis is continuing in the molecular dynamics (MD) simulations of 9,9'-bifluorene in hexane which thus far has examined the effect of excitation exchange coupling fluctuations on exciton dynamics.

F. Zhu, C. Galli, and R.M. Hochstrasser,  
*The Real Time Electronic Excitation Transfer Dynamics  
of 9,9-Bifluorene and 2',2-Binaphthyl in Solution,*  
**Journal of Chemical Physics**, 98, (1993), 1042

K. Wynne, S.Gnanakaran, C. Galli, F.Zhu and R. M. Hochstrasser,  
*Luminescence Studies of Ultrafast Energy Transfer Oscillations in Dimers*  
**Journal of Luminescence**, in press, (1993)

## II ) Ultrafast electron transfer (ET) in Nile Blue-Dimethylaniline and related complexes

A 2.5 ps component of the fluorescence decay was resolved and a  $\sim 100$  fs component observed for the electron donor / acceptor system Nile blue in dimethylaniline by Yoshihara (*Chem. Phys. Lett.*, 180, (1991), 416). In order to examine the ultrafast dynamics associated with electron transfer reactions which are competitive with solvation and vibrational relaxation times, a study of this and related systems was undertaken.

The subpicosecond electron transfer reactions from Nile blue to dimethylaniline, Nile blue to aniline, Cresyl violet to dimethylaniline and Cresyl violet to aniline following the 620 nm photoexcitation to an eigenstate of the electron donor were resolved with optical time resolved pump-probe spectroscopy. At that time, the  $\sim 85$  fs electron transfer measured for Nile Blue in dimethylaniline was one of the fastest ET reactions measured.

There are a number of undesirable properties of these electron donor / acceptor systems, however, which render them unsuitable for a systematic study of reaction dynamics. There is no evidence for any complex formation between the donor and acceptor. The electron transfer must then occur over a distribution of distances and orientations which greatly complicates the analysis of the reaction kinetics. Also the decay of the stimulated emission signal indicating the electron transfer ( $D^*A \rightarrow D^+A^-$ ) is obscured by the transient bleach which recovers with the charge recombination reaction ( $D^+A^- \rightarrow DA$ ) when probed at 650 nm. The research performed on these systems resulted in informed choices for molecular systems suitable for systematic studies of electron transfer reactions: the strongly bound molecular complex tetracyanoethylene-hexamethylbenzene and the covalently bound porphyrin-quinone species. Both of these ET systems have clearly resolvable transient ion spectra.

### III ) Low frequency coherence in electron transfer reactions

Evidence of low frequency coherence during the photoinitiated electron transfer in covalently bound porphyrin-quinones was observed with optical time resolved pump-probe spectroscopy. This species is a common model compound for the subpicosecond dynamics of photosynthetic electron transfer. The porphyrin-quinones, both metallated and free-base, are locally excited by a 620 nm photon ( $\pi \rightarrow \pi^*$ ); the electron transfer reaction proceeds as the system evolves from this excited state ( $P^*Q$ ) to the polar state ( $P^+Q^-$ ). The formation of this ionic state is followed by the charge recombination reaction ( $P^+Q^- \rightarrow PQ$ ).

Following the photoexcitation of the free-base porphyrin-quinone in toluene transient absorptions at 500 nm and 510 nm are observed. Subsequent to the initial overshoot feature in the transient absorption signal, a small recurrence at 200 fs (at 500 nm) and 300 fs (at 510 nm) is resolved. For the free-base porphyrin-quinone in the more viscous solvent glycerol triacetate, an oscillatory component in the transient absorption signal observed at 500 nm persists for  $\sim 1.5$  ps; the oscillatory signal component is  $95\text{ cm}^{-1}$ . There is a strong indication that coherence of nuclear and / or electronic origin plays a role in the electron transfer reaction in porphyrin-quinone complexes. However the small cross section of the free-base porphyrin-quinone at the excitation wavelengths available make the continued study of these species unfeasible. Suitable species with meso- substitution and metallation were synthesized for further study.

K. Wynne, C. Galli, and R.M. Hochstrasser,  
*Vibrational Coherence in Electron Transfer*,  
Ultrafast VIII ( Springer, Berlin, 1992).



#### IV) Intermolecular vibrational coherence in liquid pyrrole

The molecular dynamics of optically transparent liquids were examined using femtosecond optical Kerr effect measurements. Numerous liquids were investigated in this examination of low frequency solution dynamics, including alkanes, alcohols and other associated liquids.

Using heterodyned optical Kerr spectroscopy, a  $103\text{ cm}^{-1}$  oscillation was observed in neat pyrrole and an  $89\text{ cm}^{-1}$  oscillation in neat, deuterated pyrrole. As this frequency is well below the monomeric modes of pyrrole, and a very broad band which peaks at  $100\text{ cm}^{-1}$  has been observed in the far-infrared absorption spectrum of liquid pyrrole, this signal component is assigned to the impulsive stimulated Raman excitation of a dimeric mode of pyrrole. Semi-empirical quantum chemistry calculations have predicted a dimeric mode of  $98\text{ cm}^{-1}$ .

This liquid state dynamics examination also measures the anisotropy loss due to the decay of the rotational coherence of the ensemble: a value of 2.3 ps is observed for neat pyrrole, while the rotational decay time for the deuterated species is 1.4 ps. As these times are fairly short with respect to the calculated hydrodynamic slip time for pyrrole of 6.8 ps and the measured rotational decay time found for pyridine of  $4.0 \pm 0.3\text{ ps}$ , it is suggested that the rotational friction may be governed by dissociation and recombination dynamics rather than the more conventional forms of collisional friction.

K. Wynne, C. Galli, and R.M. Hochstrasser,  
*Femtosecond Intermolecular Vibrational Motion in Pyrrole*,  
**Chemical Physics Letters**, 193, (1992), 17

V) Electronic coherence in nearly degenerate states of magnesium tetraphenylporphyrin in solution

The role of coherences in reacting condensed phase systems is becoming a subject of intense inquiry as can be seen from recent reports of the experimental observation of nuclear coherences in photodissociation products<sup>1</sup>, charge transferring reaction centers<sup>2</sup>, underdamped behavior in electronic energy transfer<sup>3</sup>, as well as experimental<sup>4</sup> and theoretical<sup>5</sup> investigations of electronic coherences in condensed phase electron transfer events. Experimental observations of such processes must be made on time scales faster than the phase-loss mechanisms resulting from motion along the reaction coordinate; proper design may allow the measurement of the coherence decay of the initially prepared state entering the reactive regime. Such experiments thus directly reveal the phase evolution of the reaction. It is therefore of great interest to obtain knowledge of the electronic dephasing that contributes to coherence loss processes in the condensed phase.

One very basic coherence loss process involves the transition of an optically driven system from the Raman to the fluorescence regime.<sup>6</sup> It is well known that the spontaneous scattering collected in a resonant Raman experiment is emission from an electronically phased ensemble. As the electronic coherence of this system is damped, the superposition state decays to a fluorescent population which persists for the lifetime of the excited state. Therefore an experiment which observes the accompanying changes in the emission of the sample will measure the loss of electronic coherence. While the resonance Raman state is still imprinted on the system, the anisotropies associated with emission from the driven state are different than in the case of dephased fluorescence. This emission anisotropy therefore presents a novel way to access the coherence dynamics. A relationship between molecular state coherence and anisotropy in optical experiments was recently predicted.<sup>7</sup>

The anisotropy of a signal field generated by a prepared state in a pump-probe

experiment may be determined by probing the excitation with polarization both parallel and perpendicular to the pump pulse. In the experiments, the difference in the detector signals for the two polarizations,  $S_{\parallel}(t) - S_{\perp}(t)$ , normalized by the spatially integrated signal  $S_{\parallel}(t) + 2S_{\perp}(t)$ , is collected as a function of time delay between the state preparation and the probing event. If a degeneracy or near degeneracy is accessed by the initial excitation, this excitation pulse places the ensemble in a superposition state. When a probe pulse couples the components of this superposition to a common final state, the probe signal contains interference terms described by constructive Feynman paths. It is the experimental observation of the decay of this interference that is the subject which presents a novel use of a pump-probe anisotropy measurement to observe, in a room temperature liquid, the electronic dephasing of degenerate states.

Electronic coherence decay has been measured previously. The stochastic interactions between a solute and its environment which lead to the dephasing of optical transitions between nondegenerate states was studied in the time domain by two<sup>8</sup> and three<sup>9</sup> photon echo techniques. These experiments showed that the decay of electronic coherence of the transitions of polyatomic molecules in solution occurs in the time frame of 40 - 70 fs.

Porphyrins and closely related compounds serve a variety of roles in biological structures and processes. The metallotetraphenylporphyrins have approximate four-fold symmetry and hence degenerate states suitable for this investigation. The excitation and relaxation dynamics of these species have been the subject of considerable study, and a significant amount of information on their Raman and fluorescence spectra is available.<sup>10</sup> This Letter presents femtosecond optical experiments on magnesium tetraphenylporphyrin in tetrahydrofuran (MgTPP in THF) at ambient temperature.

The biphasic decay of the anisotropy signal indicates the evolution of the initial fully coherent ensemble with anisotropy 0.7 to a partially coherent ensemble with anisotropy 0.4 to a dephased, populationally equilibrated ensemble of anisotropy 0.1. The anisotropy decays with time constants 210 fs and 1.6 ps

C. Galli, K. Wynne, S. M LeCours, M. J. Therien and R. M. Hochstrasser,  
*Direct Measurement of Electronic Dephasing in Anisotropy*  
**Chemical Physics Letters**, 206, (1993), 493

R.M.Hochstrasser, B.R.Cowen, P.L.Dutton, C.Galli, S.LeCours, S.Maiti, C.C.Moser,  
D.Raftery, M.Therien, G.C.Walker and K.Wynne  
*Vibrational Dynamics in Condensed Phases and Proteins*  
**Proceedings of the International Conference on Time-Resolved Vibrational Spectroscopy**, (Springer-Verlag, Berlin, 1993)

#### References

- 1 U. Banin, A. Waldman and S. Ruhman, *J. Chem. Phys.*, **96** , (1992), 2416.
- 2 M.H. Vos, J.-C. Lambry, S.J. Robles, D.C. Youvan, J. Breton and J.-L. Martin,  
*Proc. Natl. Acad. Sci. USA*, **88** , (1991) ,8885.
- 3 F. Zhu, C. Galli and R.M. Hochstrasser, *J. Chem. Phys.*, **98** , (1993), 1042.
- 4 K. Wynne, C. Galli, P.J.F. De Rege, M.J. Therien and R.M. Hochstrasser,  
in: *Ultrafast Phenomena VIII*, Eds. J.-L. Martin e.a. (Springer, Berlin, 1993).
- 5 J.M. Jean, R.A. Friesner and G.R. Fleming, *J. Chem. Phys.*, **96** , (1992), 5827.

- 6 J. Friedman, F. Novak and R.M. Hochstrasser, in: *Laser and Coherence Spectroscopy*, ed. J.I. Steinfeld ( Plenum Press, New York 1978)  
R. M. Hochstrasser and F. A. Novak, *Chem. Phys. Lett.*, **53**, (1978), 3  
S. Mukamel, D. Grimberty and Y. Rabin, *Phys. Rev.A*, **26**, (1982) 341  
B. Dick and R.M. Hochstrasser, *J. Chem. Phys.*, **81**, (1984), 2897
- 7 K. Wynne and R.M. Hochstrasser, in press *Chem. Phys.*
- 8 P.C. Becker, H.L.Fragmito, J.Y. Bigot, C.H. Brito Cruz, R.L. Fork and C.V. Shank, *Phys. Rev. Lett.*, **63**, (1989), 505  
E.T.J. Nibbering, D.A. Wiersma and K. Duppen, *Phys. Rev. Lett.*, **66**, (1991) 2464.
- 9 J.Y. Bigot, M.T. Portella, R.W. Schoenlein, C.J. Bardeen, A. Migus and C.V. Shank, *Phys. Rev. Lett.*, **66**, (1991), 1138.
- 10 M. Gouterman, in: *The Porphyrins*, vol. III, ed. D. Dolphin (Academic Press, New York, 1978), p.1